

DOCTOR OF PHILOSOPHY

Impact of Dynamic Traffic on Vehicle-to-Vehicle Visible Light Communication

Al-sallami, Farah

Award date:
2021

Awarding institution:
Coventry University

[Link to publication](#)

General rights

Copyright and moral rights for the publications made accessible in the public portal are retained by the authors and/or other copyright owners and it is a condition of accessing publications that users recognise and abide by the legal requirements associated with these rights.

- Users may download and print one copy of this thesis for personal non-commercial research or study
- This thesis cannot be reproduced or quoted extensively from without first obtaining permission from the copyright holder(s)
- You may not further distribute the material or use it for any profit-making activity or commercial gain
- You may freely distribute the URL identifying the publication in the public portal

Take down policy

If you believe that this document breaches copyright please contact us providing details, and we will remove access to the work immediately and investigate your claim.

Impact of Dynamic Traffic on Vehicle-to-Vehicle Visible Light Communication



By

Farah Mahdi Yaseen Al-Sallami

PhD

May 2021

Impact of Dynamic Traffic on Vehicle-to-Vehicle Visible Light Communication

Farah Mahdi Yaseen Al-Sallami

*A thesis submitted in partial fulfilment of the University's requirements
for the degree of Doctor of Philosophy*

May 2021



Declaration

All sentences or passages quoted in this document from other people's work have been specifically acknowledged by clear cross-referencing to author, work and page(s). Any illustrations that are not the work of the author of this report have been used with the explicit permission of the originator and are specifically acknowledged. I understand that failure to do this amounts to plagiarism and will be considered grounds for failure.

Name: Farah Mahdi Yaseen Al-Sallami

Signature:

Date: 12/5/2021



Certificate of Ethical Approval

Applicant: Farah Al Sallami
Project Title: Movement effect on visible light communication systems

This is to certify that the above named applicant has completed the Coventry University Ethical Approval process and their project has been confirmed and approved as Low Risk

Date of approval: 21 Apr 2021
Project Reference Number: P121679

Acknowledgement

I would like to thank Highways England and Mott MacDonald for providing traffic measurements.

I would like to express my sincere gratitude to the director of studies, Dr. Olivier Haas, who has offered substantial support, advice and guidance throughout this work.

I would also like to offer my sincere gratitude and appreciation to my supervisor Dr. Sujan Rajbhandari, who has gone above and beyond with his exceptional support at the expense of his own time since the very early stages of this work.

I would like to extend my sincere thanks to my supervisor Dr. Zahir Ahmad, for his valuable support and advice throughout this work.

Sincere thanks go to Dr. Paul Anthony Haigh of the University of Newcastle for his outstanding support. I would also like to thank Prof. Cheng-Xiang Wang, Prof. Stanislav Zvanovec and Dr. Ahmed Al-Kinani for offering outstanding support.

Thanks and appreciations go to my managers, the head of higher education school, Dr. Kelly Rogers and the dean of higher education, Ms. Dale Wooly of South and City College Birmingham for their exceptional support and understanding throughout my study.

I would also like to offer special thanks to my colleagues of Coventry University, Zihao Liu, Shalika Atlis, Abdulrahman A. Mahmoud, Nurudeen Aigoro and Othman Younus of Northumbria University.

To my parents, no words can express my appreciation for your love, support and encouragement. Finally, I would like to extend my appreciation to my brothers Hussain and Hassan for their constant support and encouragement.

Abstract

Due to the directional nature of the visible light signals propagation, the performance of visible light communications (VLC) systems depends on the geometry of the link. In dynamic vehicle-to-vehicle VLC (V2V-VLC) systems, the geometry of the VLC link changes continuously due to the unpredictable movement patterns of the transmitter, receiver and surrounding vehicles. This thesis investigates the impact of dynamic traffic conditions during different times of the day to establish a statistical channel model for the V2V-VLC systems. The study considers the geometrical variation due to the variable inter-vehicle spacing and radiation pattern of vehicles' sources. The results showed that the statistical model of channel path loss is given by a convolution of the distributions of the inter-vehicle spacing and the radiation pattern of vehicles' sources. Based on the measured traffic, the line of sight (LOS) and non-LOS path loss are developed for the radiation pattern of vehicles' sources which depends on the manufactures. The study shows that the LOS path loss distribution depends on the radiation pattern, whereas it has a less significant effect on the non-LOS path loss distribution. Furthermore, the existence of multiple reflectors decreases path loss and enhances the communication link's performance. Different weather conditions add attenuation that increases the mean path loss value without changing the statistical distribution of the path loss. Studying the temporal properties of the V2V-VLC channel shows that the channel can be described as time-variant non-stationary with flat and slow fading behaviour. The bit-error-rate (BER) and signal-to-noise (SNR) ratio performance, when the on-off-keying (OOK) modulation scheme is used, depends on the dynamic traffic and the existence of other vehicles in the adjacent lanes. A difference of at least 2 dB between the required SNR values to achieve comparable BER performance in different lanes is observed.

Contents

Acronyms	xvii
1 Introduction	1
1.1 Background on VLC	2
1.1.1 Features	2
1.1.2 Applications	4
1.1.3 Challenges	5
1.2 Problem Statement	6
1.3 Motivations	6
1.4 Research aim	6
1.5 Research Objectives	7
1.6 Original contributions and publications	8
1.7 Organisation of the thesis	11
2 V2V-VLC Channel	13
2.1 Related Works	14
2.1.1 Vehicle-to-vehicle visible light channel modelling	14
2.1.1.1 Ray-tracing-based channel modelling	15
2.1.1.2 Measurement-based channel modelling	16
2.1.1.3 Analytical and simulation-based channel modelling	17
2.1.2 Impact of weather conditions	18
2.2 V2V-VLC Channel Model	22

2.2.1	Impact of weather conditions	23
2.2.2	Geometrical propagation effect	25
2.2.2.1	LOS component	27
2.2.2.2	NLOS component	28
2.2.2.3	Temporal properties	29
2.2.2.4	The performance of V2V-VLC system	33
2.3	Summary	35
3	Impact of Dynamic Traffic on V2V-VLC Channel	37
3.1	Related works	38
3.2	Impact of dynamic traffic on the inter-vehicle spacing	40
3.2.1	inter-vehicle spacing variation per lane	42
3.2.2	inter-vehicle spacing variation per motorway	49
3.3	Impact of dynamic traffic on the channel path loss	51
3.4	Summary	55
4	LOS V2V-VLC Channel	57
4.1	Related works	58
4.2	Impact of the radiation pattern on LOS V2V-VLC channel	64
4.2.1	The Lambertian model	64
4.2.2	Piecewise Lambertian model	67
4.2.3	Gaussian model	68
4.2.4	Empirical model of Toyota Altis Headlight	72
4.2.5	Comparison between different radiation pattern models	74
4.3	Impact of weather conditions on LOS V2V-VLC channel	75
4.4	Summary	77
5	Multipath V2V-VLC Channel	81
5.1	Related works	82
5.1.1	Impact of Reflection on VVLC Channel	82

5.1.2	Temporal properties of multipath VVLC channel	84
5.2	Reflection from different objects and surfaces	85
5.3	Path loss of NLOS V2V-VLC channel	87
5.3.1	Single reflector scenario	88
5.3.2	Multiple reflectors scenario	94
5.4	Temporal properties of V2V-VLC channel	96
5.4.1	Two-dimensional CIR	96
5.4.2	RMS delay spread	99
5.4.3	Two-dimensional autocorrelation function	99
5.5	Summary	103
6	Performance analysis of V2V-VLC Channel	104
6.1	Related works	105
6.1.1	Vehicle-to-vehicle visible light communication performance	105
6.1.2	Impact of interference	110
6.1.2.1	Interference from natural light sources	110
6.1.2.2	Interference from artificial light sources	112
6.2	Probability of co-existence of other vehicles in the adjacent lanes	114
6.3	BER performance of the V2V-VLC channel	125
6.4	Summary	131
7	Conclusions and Future work	134
7.1	Conclusions	134
7.2	Future work	137

List of Figures

1.1	Electromagnetic spectrum including the visible light frequency band	2
1.2	Examples of VLC applications proposed in the literature.	4
1.3	Areas of original contributions and novelty. Original contributions (blue): modelling and theoretical work carried out to simulate the system; novel (red): new models, mathematical relationships and results.	9
1.4	A brief description of the thesis substantive chapters and contents.	11
2.1	A communication system with examples of channel impairments that distort the transmitted signal.	14
2.2	A classification of channel modelling approaches and methods.	15
2.3	Possible VVLC channel impairment due to a) rain (Sakhastka/Getty, 2021), b) fog (Singh/National, 2015), c) haze (Lee/Reuters, 2017) and d) snow- fall (Hanacekl, 2018).	19
2.4	Scattering models according to particle size.	20
2.5	Illustration of multipath propagation of the optical signal between transmitter and receiver vehicles due to reflection and scattering from other vehicles, road surface and roadside objects.	25
2.6	Illustration of three-dimensional geometry of V2V-VLC link.	27
2.7	Illustration of a communication link between two vehicles A & B and NLOS component due to reflection from vehicle j	29
2.8	Effect of multipath propagation on the transmitted signal.	30

2.9	Block diagram of a communication system that uses OOK modulation scheme.	33
2.10	Conditional probability density function of OOK modulation signals.	34
3.1	Map showing M42 and M6 in the West Midlands, UK (Highways England, n.d.).	41
3.2	Traffic flow variation and inter-vehicle spacing variation during the day. . .	42
3.3	Inter-vehicular distribution provided by traffic measurements in three lanes on the M42, M6 and combined M42 & M6 at a) 00:00-03:00 and b)16:00-19:00.	43
3.4	The cumulative density function of inter-vehicle spacing in the left-hand lane at 00:00-03:00.	46
3.5	The cumulative density function of inter-vehicle spacing in the middle lane at 00:00-03:00.	46
3.6	The cumulative density function of inter-vehicle spacing in the right-hand lane at 00:00-03:00.	47
3.7	The cumulative density function of inter-vehicle spacing in the left-hand lane at 16:00-19:00.	47
3.8	The cumulative density function of inter-vehicle spacing in the middle lane at 16:00-19:00.	48
3.9	The cumulative density function of inter-vehicle spacing in the right-hand lane at 16:00-19:00.	48
3.10	The cumulative density function of reflection at late 00:00-03:00 and rush 12:00-15:00 hours.	50
3.11	The a) PDF and b) CDF curves of the Line-of-Sight (LOS) component of Vehicle-to-Vehicle Visible Light Communications (V2V-VLC) the simulated path loss in (3.4) and the equivalent statistical distribution (theoretical) in (3.6), when the inter-vehicle spacing D has a log-normal distribution with parameters given in Table 3.4, at 00:00-03:00 (late hours) and 12:00-15:00 (rush hours).	53

3.12	The a) PDF and b) CDF of the LOS component of V2V-VLC path loss when the inter-vehicle spacing D has an exponential distribution with $\lambda_s = 0.0039 \text{ veh.m}^{-1}$	55
4.1	Examples of vehicular light sources design from different manufacturers including a) 2010 Audi R8 headlight (Lee et al., 2012b), b) Yamaha Cygnus-X scooter taillight (Viriyasitavat et al., 2013), c) 2015 Toyota Corolla Altis taillight (Toyota, 2018), d) 2015 Toyota Corolla Altis headlight (Toyota, 2018), e) 2017 Ford Mondeo multibeam headlight (Ford, 2020) and f) Audi A5 S5 taillight (Audi, 2021).	62
4.2	The probability density function of channel path loss obtained by the Lambertian at 00:00-03:00 (late hours) and 12:00-15:00 (rush hours).	66
4.3	The statistical and simulated PDFs of the LOS component of the V2V-VLC path loss using the piecewise Lambertian model when the inter-vehicle spacing D has a log-normal distribution at 00:00-03:00 (late hours) and 12:00-15:00 (rush hours).	67
4.4	a) Polar plot of the radiation pattern of vehicle source which uses Philips LUXEON® Rebel in the horizontal 0° and vertical 90° planes b) The normalized intensity pattern of the theoretical Gaussian model, single Philips LUXEON® light emitting diode (LED) and vehicle source which uses Philips LUXEON®.	70
4.5	The numerical evaluation of the term $10 \log(I_C(\phi))$ when $\phi \sim U(0, 60^\circ)$ and the LED Philips LUXEON® Rebel is used.	71
4.6	The probability density function of channel path loss obtained by the Gaussian model of the LED Philips LUXEON® Rebel at 00:00-03:00 (late hours) and 12:00-15:00 (rush hours).	72
4.7	The CDFs of the path loss obtained by raytracing and the Monte Carlo (MC) simulation of the Gaussian model of a LED at 00:00-03:00 and 12:00-15:00.	73

4.8	The PDF of channel path loss obtained by the empirical radiation model at 00:00-03:00 (late hours) and 12:00-15:00 (rush hours).	75
4.9	The CDFs of path loss for the Lambertian model, Gaussian angular distribution model and empirical asymmetric radiation patterns at a) 00:00-03:00 and b) 12:00-15:00.	76
4.10	Weather impact on V2V-VLC path loss for a) Lambertian, b) Piecewise Lambertian c) Empirical, d) Gaussian models at 00:00-03:00 (right-side) and 12:00-15:00 (left-side).	78
5.1	Geometry of NLOS link when reflection from road surfaces and neighbouring vehicles is considered.	86
5.2	Reflection from different surfaces with different nature and physical state includes reflection from vehicles, wet road surface, Portland cement concrete and asphalt with a very smooth texture.	88
5.3	The a) PDFs and b) CDFs of NLOS component of V2V-VLC path loss for a Lambertian source when a single reflector is considered and the inter-vehicle spacing D has a log-normal distribution for various half-power angles $\Psi_{1/2}$ for the time intervals 00:00-03:00 and 12:00-15:00.	91
5.4	The a) PDF and b) CDF of NLOS component of the V2V-VLC path loss for Lambertian source when a single reflector is considered and the inter-vehicle spacing D has a log-normal distribution for three different values of f 2 m, 1.5 m and 1 m, respectively, for the time intervals 00:00-03:00 and 12:00-15:00.	93
5.5	The a) PDF and b) CDF of NLOS V2V-VLC path loss using the piecewise Lambertian model when the inter-vehicle spacing D has a log-normal distribution and $f=1$ m for the time intervals 00:00-03:00 and 12:00-15:00.	95
5.6	Multiple reflection path loss distribution of four reflectors vehicles, at a) 00:00-03:00 and b) 12:00-15:00.	97
5.7	The two-dimensional CIR of the V2V-VLC channel when the inter-vehicle spacing has a log-normal distribution at a) 00:00-03:00 and b) 12:00-15:00.	98

5.8	The RMS delay spread σ_{rms} of the V2V-VLC channel for a) high-density traffic and b) low-density traffic.	100
5.9	The autocorrelation functions and coherence time of V2V-VLC channel at 00:00-03:00 (a and b) and 12:00-15:00 (c and d), respectively.	101
6.1	A realistic scenario with the presence of surrounding vehicles that introduces multiple reflectors as well as the increased ambient noise due to the light sources (Syed, 2014).	106
6.2	System setup of Shen and Tsai (2017); Béchadergue et al. (2019) experiment.	108
6.3	A photograph of a realistic driving scenario in presence of the sunlight (Pxhere.com, 2017).	110
6.4	VVLC channel path loss as a function of distance and under different illumination conditions (Turan et al., 2018, Figure 5).	112
6.5	Reflection and the direct light from the surrounding vehicles increases the shot noise at the receiver.	115
6.6	The probability of co-existence of other vehicles in the right-hand (L_3), middle (L_2) and left-hand (L_1) lanes during the off-peak hours at a) 00:00-06:00 and b) 00:00-03:00.	117
6.7	The probability of co-existence of other vehicles versus time in the right-hand (L_3), middle (L_2) and left-hand (L_1) lanes during the high-density traffic hours a) 06:00-20:00 and b) 16:00-19:00.	118
6.8	The probability of co-existence of other vehicles versus time on the right-hand (L_3), middle (L_2) and left-hand (L_1) lanes during the night hours (20:00-24:00).	119
6.9	The cumulative density functions of the co-existence of other vehicles in the left-hand lane at 00:00-03:00	121
6.10	The cumulative density functions of the co-existence of other vehicles in the middle lane at 00:00-03:00	122

6.11	The cumulative density functions of the co-existence of other vehicles in the right-hand lane at 00:00-03:00	122
6.12	The cumulative density functions of the co-existence of other vehicles in the right-hand lane at 16:00-19:00.	123
6.13	The cumulative density functions of the co-existence of other vehicles in the middle lane at 16:00-19:00.	123
6.14	The cumulative density functions of the co-existence of other vehicles in the left-hand lane at 16:00-19:00.	124
6.15	The cumulative density function of the co-existence of other vehicles in the adjacent lanes during off-peak hours 00:00-03:00 and during peak hours 16:00-19:00 periods.	124
6.16	A typical communication link between two vehicles travelling on a three-lane motorway and co-existence of other vehicles in the adjacent lanes which act as a) interference sources and b) reflectors.	127
6.17	BER performance of the V2V-VLC link in three lanes at 00:00-03:00 when a) the empirical and b) the Lambertian models are considered.	129
6.18	BER performance of the V2V-VLC link in three lanes at 16:00-19:00 when a) the empirical and b) the Lambertian models are considered.	130

List of Tables

1.1	A comparison between RF and VLC-based communications.	3
2.1	Summary of research works that studied the weather conditions on VVLC systems.	22
2.2	Parameters of (2.3) and (2.4).	24
2.3	Matrix of channel classification depending on the time parameters of the channel and the transmitted signal properties.	31
3.1	Summary of the research that considered the impact of traffic conditions on VVLC systems.	40
3.2	Parameters of log-normal distribution that describes the inter-vehicle spacing per lane on the M42, M6 and combined M42 & M6.	44
3.3	Parameters of log-normal distribution that describes the inter-vehicle spacing per lane.	45
3.4	Parameters of different distributions that expected to describe the inter-vehicle spacing per motorway.	50
3.5	Summary of mean and variance values of the statistical path loss when the inter-vehicle spacing D has a log-normal distribution for time intervals 00:00-03:00 and 12:00-15:00.	52
4.1	Examples of vehicular light sources that were considered in the literature.	63
4.2	Parameters of the piecewise Lambertian model (Viriyasitavat et al., 2013).	68

4.3	Coefficients of Gaussian function which describes luminous intensity distribution of Philips LUXEON® Rebel LED (Moreno and Sun, 2008; Ding et al., 2016).	69
4.4	Parameters of log-normal distribution that describes the inter-vehicle spacing.	74
4.5	Summary of mean and variance values of the statistical path loss distributions.	77
4.6	Attenuation values and parameters for different weather conditions (Kim et al., 2015; Hu et al., 2007).	79
4.7	Summary of mean path loss values of the statistical path loss (in dB) for different weather conditions and radiation models.	79
5.1	Reflective indexes of different road object materials.	87
5.2	Results summary of the reflection component path loss when a single reflector is considered for various half-power angles $\Psi_{1/2}$	90
5.3	Results summary of the reflection component path loss when a single reflector is considered for three different values of f 2 m, 1.5 m.	92
5.4	Values of the RMS delay spread σ_{rms} of V2V-VLC channel at rush and late hours compared to previous works.	102
5.5	Values of the 50% coherence time for different inter-vehicle spacing distributions.	102
6.1	Summary of the performance of VVLC systems reported in the literature.	107
6.2	Parameters of different distributions that are expected to describes L_k	120
6.3	Simulation parameters.	125
6.4	A summary of the transmitted SNR values to achieve BER= 10^{-6} for different models, lanes, and configurations.	132

Acronyms

AGC automatic gain control

APD avalanche PD

AWGN additive white Gaussian noise

BER bit-error-rate

CDF cumulative density function

CIR channel impulse response

ECE R112 Economic Commotion for Europe Regulation No. 112

FOV field of view

GEV generalized extreme value distribution

I-MPPM inverted-MPPM

IM/DD Intensity Modulation/Direct Detection

IR infrared

ISI inter-symbol-interference

ITS intelligent transportation system

LED light emitting diode

LEO Low-Earth-Orbit

LOS Line-of-Sight

MC Monte Carlo

MIMO multiple-input-multiple-output

mmWave Millimetre Wave

MPAM M-ary pulse amplitude modulation

MPPM M-ary pulse position modulation

NLOS non-Line-of-Sight

OFDM orthogonal-frequency-division-multiplexing

OOK on-off-keying

OWC Optical Wireless Communications

PAM pulse amplitude modulation

PD photodiode

PDF probability density function

PDR packet delivery rate

PPP poisson point process

RF Radio Frequency

RMS root-mean-square

RMSE root-mean-square-error

SC-BPSK sub-carrier-BPSK

SINR signal-to-interference-noise ratio

SNR signal-to-noise ratio

SPAD single-photon avalanche diode

SRR symbol reception rate

SSL solid state light

SUMO simulation of urban mobility

US uncorrelated scattering

UV ultraviolet

V2I vehicle-to-infrastructure

V2V vehicle-to-vehicle

V2V-VLC Vehicle-to-Vehicle Visible Light Communications

VENETOS vehicular network open simulator

VLC Visible Light Communications

VLiDAR Visible Light Detection and Ranging

VVLC Vehicular visible light communications

WSS wide sense stationary

List of Symbols

$\alpha, \delta, \beta, \epsilon, \text{ and } \omega$	Numerical coefficients of the Toyota Altis headlight radiation pattern empirical model
$\alpha(t)$	Amplitude of the received signal
\otimes	Convolution
Δt	Time difference
$\delta()$	Dirac delta function
η	Visibility range dependent parameter due to weather conditions
γ	Photodetector responsivity
$\Gamma(\lambda)$	Weather conditions attenuation coefficient
Γ_k	FET channel noise factor
ι	Discrete-time instant
λ	Light wavelength
λ_s	Parameter of an exponential distribution that describes the inter-vehicle spacing per motorway at low-density traffic
$\mu_b \text{ and } \sigma_b$	Parameters of the channel path loss when Lambertian radiation pattern model is considered

μ_c and σ_c	Parameters of the channel path loss when the empirical radiation pattern model is considered
μ_d and δ_d	Parameters of log-normal distribution of the inter-vehicle spacing per lane
μ_g and σ_g	Parameters of the inter-vehicle spacing per motorway in logarithmic scale
μ_j and σ_j	Parameters of the channel path loss due to multiple reflection
μ_k and σ_k	Parameters of the channel path loss when piecewise Lambertian radiation pattern model is considered
μ_l and δ_l	Parameters of a log-normal distribution describes the probability of the co-existence of other vehicles in the adjacent lanes
μ_m and σ_m	Parameters of the channel path loss a log-normal distributed inter-vehicle spacing is considered
μ_n and σ_n	Parameters of generalized extreme value distribution of the the channel path loss when the inter-vehicle spacing has a exponential distribution
μ_o and σ_o	Parameters of a normal distribution describes the term $\log(D+1)$ when inter-vehicle spacing per motorway D has a log-normal distribution
μ_q and σ_q	Parameters of the channel path loss due to single reflection
μ_r and σ_r	Parameters of a log-normal distribution describes the variation in the length of the reflection paths
μ_s and σ_s	Parameters of a log-normal distribution of the inter-vehicle spacing per motorway

Φ	Elevation (vertical) irradiance angle of the vehicle's source radiation pattern
ϕ	Azimuth (horizontal) irradiance angle of the vehicle's source radiation pattern
ϕ_o	Numerical maximum value of irradiance angle
ϕ_s	Angle of irradiance with respect to the normal to the reflector
ϕ_T	Angle of irradiance with respect to the LOS line between the transmitter and receiver
$\Psi_{1/2}$	Half power angle of a source radiation pattern
ρ	Reflection index
σ_{rms}	RMS delay spread of the channel
σ_{shot}^2	Variance of the shot noise
σ_{th}^2	Variance of the thermal noise
σ_{total}^2	Total variance of the Additive white Gaussian noise
τ	Propagation delay
τ_{excess}	Mean excess delay
θ	Incident angle at the receiver
θ_R	Incidence angle at the receiver when reflection occurs
ζ	Path loss exponent in
$A_c(t; \tau)$	Two-dimensional autocorrelation function
A_r	Receiver area

B_c	Channel coherence bandwidth
B_D	Channel Doppler spread
B_s	Bandwidth of the signal
B_w	Noise bandwidth
c	Speed of light
C_{pd}	Capacitance of PD per unit area
D	Inter-vehicle spacing per motorway
d_1	Longitudinal inter-vehicular spacing from the transmitter to the reflector
d_2	Longitudinal inter-vehicular spacing from the reflector to the receiver
D_l	Inter-vehicle spacing per lane
e	Naperian number
E_b	Bit energy
f	Lateral inter-vehicle spacing
f_k	Logical indicator of the traffic flow in the adjacent lanes
$flow_k$	Traffic flow
G_v	Open-loop voltage gain
g_m	FET transconductance
$g_S()$	Receiver concentrator gain
g_t	Optical gain of the transmitter

$h(t)$	Channel impulse response accounts for geometrical propagation effects
$h_T(t)$	Total channel impulse response accounts for geometrical propagation and the weather conditions effects
$h_{LOS}(t)$	Line-of-sight component of the channel impulse response
$h_{NLOS}(t)$	Non-line-of-sight component of the channel impulse response
h_w	Weather conditions effects
I_2	Noise bandwidth factor
I_3	Noise bandwidth factor
I_{bg}	Background current
j	Single reflector
J_r	Total number of reflectors
k	Indicator of the left-hand, middle and right-hand lanes
K_p	Boltzmann's constant
l_v	Visibility range due to weather conditions
m	Order of Lambertian emission
$N_0/2$	Double-sided power spectral density of the Additive white Gaussian noise
$n_o(t)$	Additive white Gaussian noise process
O_k	Occupation percentages per lane
$P_d(t, \tau)$	Power delay profile of the channel

P_I	Interference power
P_R	Received power
$P_X(x)$	Probability distribution of a random variable X
P_{avg}	Average transmitted power
q	Electron charge
r_1	Distances from the transmitter to the reflector
r_2	Distances from the reflector to the receiver
R_ν	Event of having more than two vehicles in any adjacent two lanes at any time instant
r_j	Distances from the j^{th} reflector to the receiver
r_{th}	Optimum decision threshold of maximum likelihood detector the receiver when on-off keying modulation is used
s	Peak photocurrent energy at the receiver when on-off keying modulation is used.
T_a	Absolute temperature
T_b	Bit duration
T_c	Channel coherence time
T_s	Symbol time duration
$T_S()$	Receiver optical filter
$u(t)$	Electrical baseband signal
$x_t(t)$	Transmitted optical signal

$y_r(t)$	Received signal
$(g_{1i}, g_{2i}, g_{3i}, \text{ and } g_{4i})$	Coefficients the Gaussian radiation pattern model
$E[]$	Expectation of a random variable
$V[]$	Variance of a random variable

Chapter 1

Introduction

In future cities, everything is interconnected using sustainable, ecological and energy-efficient communication links. This ecosystem requires complex and paradigm-shifting communication platforms to handle a high communication speed and capacity demand.

Conventional wireless communication technologies utilise [Radio Frequency \(RF\)](#) and microwaves as part of the electromagnetic spectrum as depicted in [Figure 1.1](#). However, due to the increased demand for high bandwidth and transmission rate for communications platforms, it is expected that [RF](#) and microwave technologies will suffer from 'spectrum crunch' and high interference. Therefore, other technologies such as [Millimetre Wave \(mmWave\)](#) and [Optical Wireless Communications \(OWC\)](#) have been proposed as complementary solutions to support high data rate transmission and broad bandwidth with reduced interference ([Al-Kinani, Wang, Zhou and Zhang, 2018](#)).

[OWC](#) includes communications that use optical frequencies in [infrared \(IR\)](#), visible light and [ultraviolet \(UV\)](#) bands. This thesis considers communications technologies using the visible light frequency bands of the electromagnetic spectrum, known as [Visible Light Communications \(VLC\)](#). This chapter introduces [VLC](#), its features, applications and challenges. This is followed by the problem statement, motivation, objectives, original contributions before outlining the contents of this thesis.

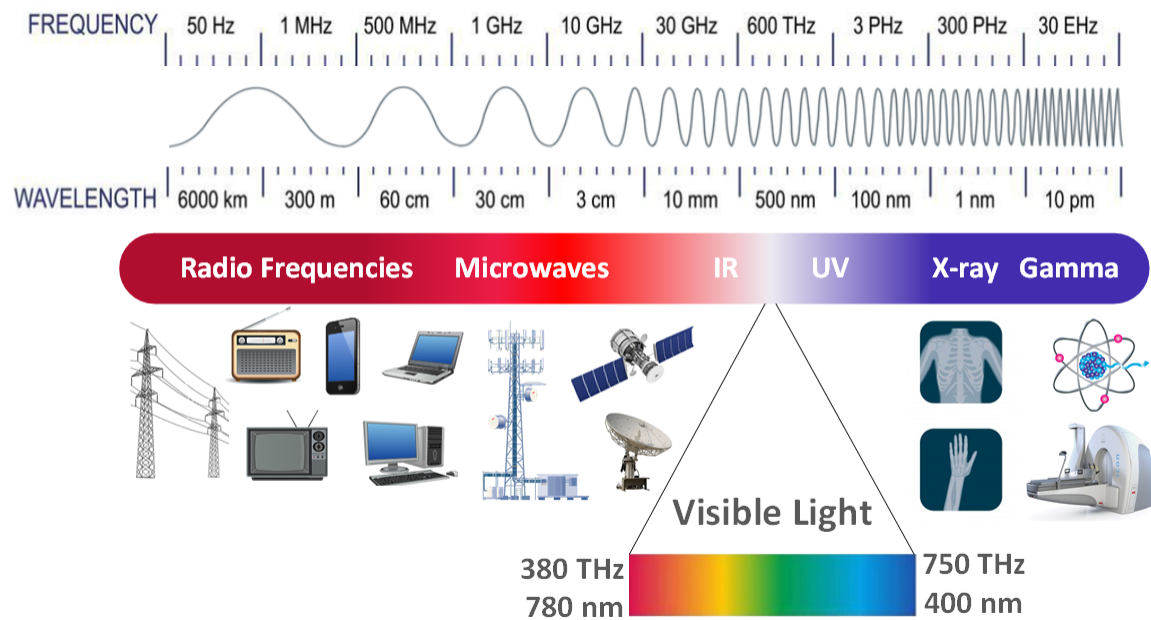


Figure 1.1: *Electromagnetic spectrum including the visible light frequency band*

1.1 Background on VLC

VLC is a subset of OWC that uses visible wavelengths between 400 nm and 780 nm (Ghassemlooy et al., 2019, P. 36). VLC offers a large communication bandwidth of 300 THz. It can support a high data rate of 10 Gbps by exploiting wavelength, space and frequency division multiplexing (Chun et al., 2019). VLC is attractive for high-speed and short-range indoor and outdoor communications as illumination infrastructure can be modified to provide multiple functionalities of illumination, high-speed communications, positioning and sensing, e.g., Visible Light Detection and Ranging (VLiDAR) (Hassan et al., 2015; Ghassemlooy et al., 2017). The following subsections provide background on VLC features, applications, and challenges that might arise with VLC technology.

1.1.1 Features

VLC is a promising communications technology due to its favourable features, which are described below:

Table 1.1: A comparison between RF and VLC-based communications.

Feature	RF-based systems	VLC-based systems
Bandwidth	Limited	Large
Spectrum	Limited Availability	Available
Interference	High	Limited
Energy efficiency	Limited	High
Coverage distance	Long	Short
LOS dependency	Independent	Dependent
Mobility	High	Limited
Security	Limited	High
Commercial availability	Widely available	Limited availability
Deployment	Widely deployed	Limited

License-free broadband and speed of communications are the primary motivations for establishing VLC. Operating in the license-free visible light spectrum, VLC is promising to support the 6G network with a data rate of hundreds of Gb/s (Huang et al., 2019).

Sustainability and energy efficiency due to the reduced power consumption make VLC a cost-effective communication technology (Rajagopal et al., 2012; Pathak et al., 2015). VLC is considered sustainable due to the long lifespan of solid state light (SSL) sources compared to conventional light sources (Pathak et al., 2015). In addition, it uses the available lighting infrastructure to support high-speed communications with reduced additional cost.

Security is one of the most important features of VLC. The restricted propagation of visible light through walls and spatial confinement can provide high secure communications (Arfaoui et al., 2020; Huang et al., 2019). In addition, its directional nature provides immunity to interference and jamming attacks (Ishihara et al., 2015; Huang et al., 2019).

Table 1.1 provides a comparison between RF and VLC-based communications. VLC is a candidate communication platform for many applications, as explained in the following section.

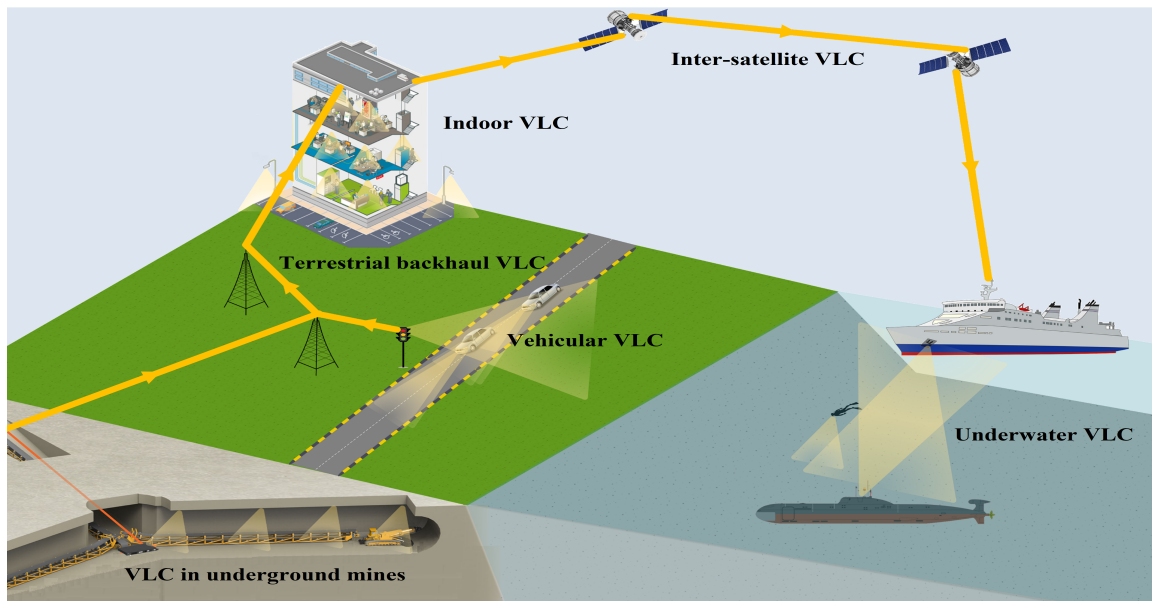


Figure 1.2: Examples of VLC applications proposed in the literature.

1.1.2 Applications

VLC can support underwater, underground and free-space applications as illustrated in Figure 1.2.

Underwater communications: VLC can support high data rate and low-latency communications for underwater and marine networks as acoustic or RF-based underwater networks have limited bandwidth and high latency (Jiang et al., 2020; Elamassie and Uysal, 2020; Ahmad et al., 2016).

Underground communications: VLC is applied to underground mining environments due to its immunity to interference and ability to provide safe communication in such a harsh propagation environment (Játiva et al., 2020; Iturralde et al., 2017; Wang et al., 2018).

Free-space communications: VLC can be used for inter-satellite communication for Low-Earth-Orbit (LEO) small satellite networks (Amanor et al., 2018; Ciaramella et al., 2020), terrestrial communication for backhaul connectivity (Zedini et al., 2015; Gupta et al., 2017), a high-speed internet connection through indoor Li-Fi attocell networks (Kazemi et al., 2019; Haas et al., 2016) and target tracking, positioning and localisation in indoor and outdoor environments where global positioning systems cannot fulfil the expectation (Mousa et al.,

2018; Zhang et al., 2014; Jung et al., 2011; Yasir et al., 2016).

Another key application of VLC is the [intelligent transportation system \(ITS\)](#). Aiming for safer and accident-free roads, VLC was proposed as an alternative communication technology to support traffic management ([Uysal et al., 2015](#)). Vehicular communication can increase drivers' awareness of their environment, thereby reducing human errors, which are believed to be the main cause of road-accidents ([World Health Organization, 2018](#); [Rehman et al., 2019](#)). [Vehicular visible light communications \(VVLC\)](#) systems employ vehicle light sources, traffic lights and street lighting to transmit traffic data between vehicles and interact with pedestrians and infrastructures, enabling connected and autonomous safety features on vehicles ([Al-Kinani, Sun, Wang, Zhang, Ge and Haas, 2018](#); [Rehman et al., 2019](#)).

As discussed above, VLC has a lot of favourable features which make it a potential candidate for many applications. However, there are a few challenges that need to be addressed, as discussed in the following section.

1.1.3 Challenges

An optical signal experiences high propagation attenuation and cannot penetrate through opaque objects. Therefore, VLC is more appropriate for short transmission ranges ([Memedi and Dressler, 2021](#)). Optical signal propagation in free space is subject to multiple reflections, scattering and possible blockage by surrounding objects. This negatively affects the quality of the received signal. In addition to the imposed safety constraints on the transmission power, distortion and clipping caused by the nonlinear characteristics of the optical transmitter (LED/laser diode) add further constraints on the transmission power ([Arfaoui et al., 2020](#)).

In [V2V-VLC](#), the outdoor environment adds challenges, such as attenuation and power fluctuation due to varying weather conditions and atmospheric turbulence ([Elamassie et al., 2018](#); [Naboulsi et al., 2005](#)). Furthermore, [V2V-VLC](#) is subject to additive ambient noise induced by artificial and natural sources ([Islim and Haas, 2017](#); [Trio Adiono and Fuada, 2017](#)). The geometry of [V2V-VLC](#) link is continuously changing due to vehicles mobility and dynamic traffic. Therefore, studying the impact of dynamic traffic on [V2V-VLC](#) channel

modeling that considers the impact of weather and additive ambient noise induced by artificial and natural sources is required.

1.2 Problem Statement

The directional nature of VLC increases its sensitivity to any changes in the link geometry due to the movement of the transmitter, receiver and/or the surrounding vehicles. This adds a factor of randomness to the V2V-VLC link parameters. Hence, a statistical channel model that considers the spatial variation due to dynamic traffic should be established to describe the channel model of V2V-VLC systems.

1.3 Motivations

Few studies have investigated the impact of vehicles mobility and dynamic traffic on the V2V-VLC channel. The majority of VVLC studies were experimental and did not provide a reproducible channel model suitable to design reliable mobile VLC systems. V2V-VLC channel model should account for mobility, relative directions of vehicles movement, and traffic densities at different times of the day. The research aim that addresses these research gap is described in the following section.

1.4 Research aim

The aim of this research is to investigate the impact of unpredictable movement patterns of vehicles due to dynamic traffic on V2V-VLC channel model at different traffic densities during different times of the day. The research also considers the the impact of weather and additive ambient noise.

1.5 Research Objectives

The research objectives of this research are given as follows:

1. Establish a statistical large-scale (path loss) model for **V2V-VLC** systems considering the geometrical variation of the communication link due to dynamic traffic and the angular radiation distribution of the light sources of the vehicle.

The large-scale fading caused by path loss dominates **V2V-VLC** performance. To establish the **V2V-VLC** path loss model, an accurate model to describe the radiation pattern of the vehicle's source is required. This is because the **V2V-VLC** use vehicles' optical sources to transmit data. The radiation pattern of these sources for safety purpose is regulated to be asymmetrical. In addition, the design of these sources varies depending on the purpose of use (taillight, low-beam headlight and high-beam headlight) and the manufacturer. The available **V2V-VLC** channel models can only describe symmetrical sources, one-dimensional link geometry or specific headlight design.

Because the path loss dominates **V2V-VLC** performance, it is vital to consider it to accurately estimate the link budget, outage probability and capacity of the **V2V-VLC** channel.

2. Investigate the impact of dynamic traffic on temporal properties of multipath **V2V-VLC** channel. The temporal properties of the multipath **V2V-VLC** channel quantify the channel variations with propagation time and delay that affect the bit duration, and achievable data rates. Different communication techniques are designed to adapt to the channel impairments. Therefore, it is vital to determine the temporal properties of the multipath **V2V-VLC** channel to design the communication techniques that achieve optimum performance.
3. Estimate the probability of the co-existence of other vehicles in the adjacent lanes and examine its impact on the **signal-to-noise ratio (SNR)** and **bit-error-rate (BER)** performance of dynamic **V2V-VLC** systems.

Surrounding vehicles are the closest reflective objects in vehicular communication systems, including VLC-based systems. However, the presence of surrounding vehicles varies with the dynamic vehicles density and traffic flow that change during the day. Therefore, identifying the probability of co-existence of other vehicles in the adjacent lanes is important to study the performance of V2V-VLC and other vehicular communication systems that use different transmission technologies.

1.6 Original contributions and publications

The areas of original and novel contributions of this study are illustrated in Figure 1.3. As shown in the figure, the main contributions of this study are summarised below:

- Established a statistical large-scale (path loss) model of V2V-VLC which considers realistic traffic conditions. The statistical V2V-VLC channel model considers the LOS and non-Line-of-Sight (NLOS) channel components and reflection from single and multiple reflectors. Reflection from different road and object surfaces with different nature and physical states was examined to identify reflective objects with a more substantial influence on optical signal propagation. The model also considers the impact of weather conditions on V2V-VLC channel gain. The results were validate and verify using MC simulation and the Kolmogorov-Smirnov test.

Novelty: It is the first statistical path loss V2V-VLC channel model that considers realistic traffic conditions and quantifies the path loss of the channel due to reflection from different road and object surfaces with different nature and physical states.

Relevant published papers:

1. F. M. Alsalamy, Z. Ahmad, S. Zvanovec, P. A. Haigh, O. Haas, and S. Rajbhandari. Statistical Channel Modelling of Dynamic Vehicle-to-Vehicle Visible Light Communication System. *Vehicular Communications*, 29: 100339, 2021. <https://doi.org/10.1016/j.vehcom.2021.100339>.

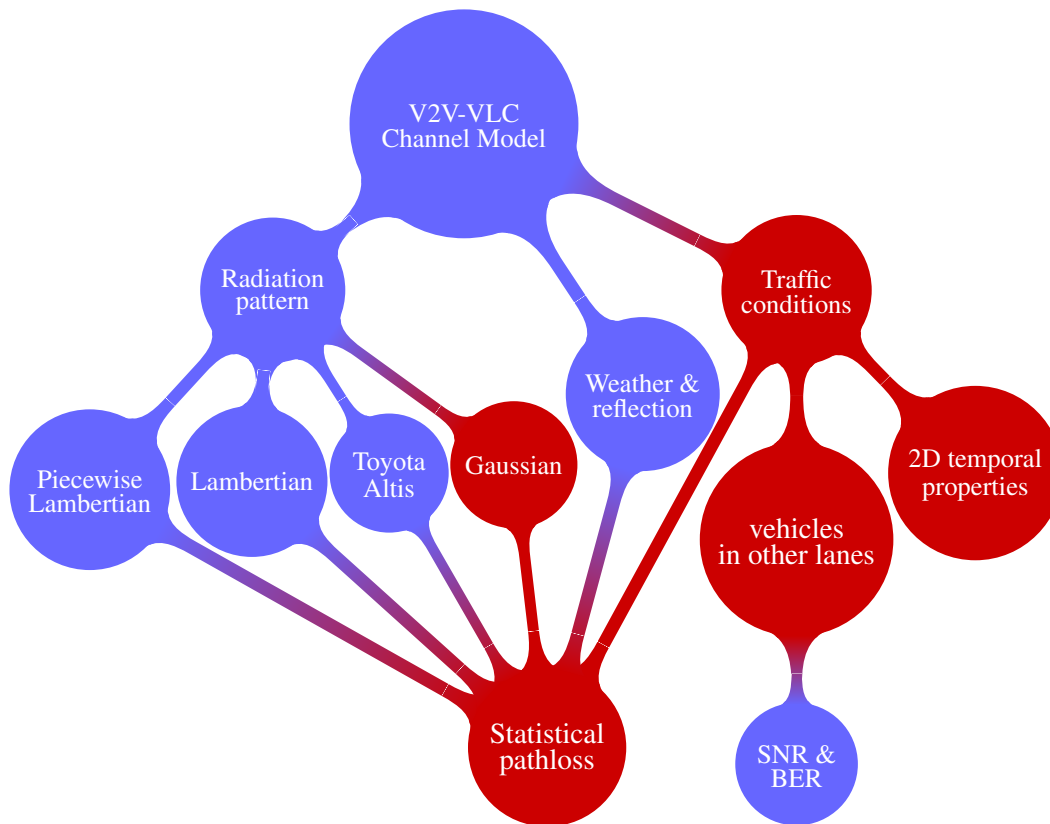


Figure 1.3: Areas of original contributions and novelty. Original contributions (blue): modelling and theoretical work carried out to simulate the system; novel (red): new models, mathematical relationships and results.

2. F. M. Alsalamy, Z. Ahmad, O. Haas, S. Rajbhandari, "regular-shaped Geometry-Based Stochastic Model for Vehicle-to-Vehicle Visible Light Communication Channel. Research Symposium, EEC, Coventry University, Coventry, UK, June 2019. **Best research poster for the IFTC.**
 3. F. M. Alsalamy, Z. Ahmad, O. Haas, and S. Rajbhandari. Regular-shaped geometry-based stochastic model for the vehicle-to-vehicle visible light communication channel. in Proc. 2019 IEEE Jordan Int. Joint Conf. Elect. Eng. Inf. Technol. (JEEIT'19), Amman, Jordan, Apr. 2019, pp. 297–301.
- Described the temporal properties of the **V2V-VLC** channel using a two-dimensional model.

Novelty: This is the first two-dimensional (i.e time and delay) model that describes temporal properties of the **V2V-VLC** channel considering different traffic densities during different times of the day.

Relevant published paper: F. M. Alsalamy, Z. Ahmad, P. A. Haigh, O. Haas, and S. Rajbhandari, "The statistical temporal properties of vehicular visible light communication channel," in Proc. 12th IEEE/IET Int. Symp. Commun. Syst. Netw. and Digit. Signal Process. (CSNDSP'20), Porto, Portugal, July 2020, pp. 1–4.

- Relying on traffic measurements collected from the M42, and M6 motorways, in the UK, this work estimated the probability of co-existence of other vehicles in the adjacent lanes that act as mobile reflectors and evaluated its impact on the **SNR** and **BER** performance of **V2V-VLC** systems.

Novelty: This is the first statistical **V2V-VLC** channel that considered a realistic dynamic traffic scenario and estimates the probability of co-existence of other vehicles in the adjacent lanes.

Relevant published paper: F. M. Alsalamy, O. Haas, A. Al-Kinani, C-X. Wang, Z. Ahmad, and S. Rajbhandari. Impact of Dynamic Traffic on Vehicle-to-Vehicle Visible Light Communication Systems. IEEE Systems Journal, Early access. <http://doi:10.1109/JSYST.2021.3100257>.

- Quantified the impact of radiation patterns of the vehicle's sources on the statistical path loss of dynamic **V2V-VLC** channel using the Lambertian, piecewise Lambertian, Gaussian and Toyota Altis empirical models.

Novelty: This is the first statistical **V2V-VLC** channel model that uses the Gaussian model to describe the asymmetrical radiation pattern of the vehicle's sources.

Relevant published paper: F. M. Alsalamy, N. Aigoro, A. A. Mahmoud, Z. Ahmad, S. Zvanovec, P. A. Haigh, O. Haas, and S. Rajbhandari. Impact of Vehicle Headlights Radiation Pattern on Dynamic Vehicular VLC Channel. IEEE/OSA Journal of Lightwave Technology. 39(10): 3162 - 3168, 2021. <https://doi.org/10.1109/JLT.2021.3064811>

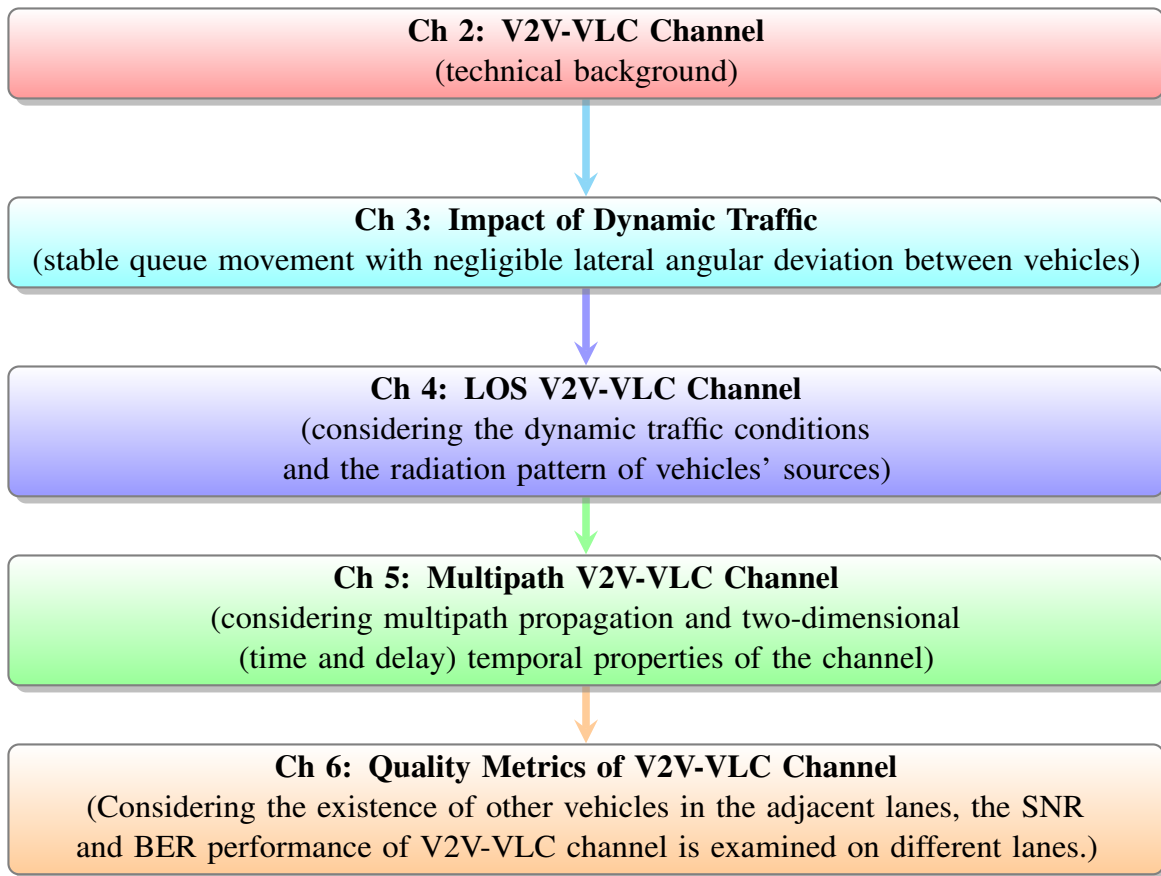


Figure 1.4: A brief description of the thesis substantive chapters and contents.

1.7 Organisation of the thesis

This thesis consists of seven chapters, including the introduction and conclusion chapters. A brief description of the thesis substantive chapters and contents is illustrated in Figure 1.4.

Chapter 2 provides the technical background and fundamental principles considered in this study to investigate the V2V-VLC channel model.

Chapter 3 considers the inter-vehicle spacing variation due to dynamic traffic to develop a statistical path loss channel model. Assuming a stable queue driving scenario with the negligible lateral angular deviation between vehicles, the analysis focuses on inter-vehicle spacing variation exclusively. Hence, the angular distribution of the vehicular source radiation pattern is not considered in Chapter 3.

Chapter 4 examines the impact of the dynamic movement of the vehicles on the LOS

component of the **V2V-VLC** channel. A statistical channel model to describe the path loss of **V2V-VLC**, considering the dynamic traffic conditions and the radiation pattern of vehicles light sources, is established. For this purpose, four radiation patterns models (Lambertian, Gaussian, piecewise Lambertian and empirical) are utilised to describe the radiation angular distribution of vehicles' sources. In addition, Chapter 4 considers the impact of weather conditions on the **LOS V2V-VLC** channel.

Chapter 5 investigates the path loss and channel temporal properties of the **V2V-VLC** channel due to multipath propagation. Reflection from different road objects surfaces is first examined. Path loss of **NLOS V2V-VLC** channel is investigated considering the single and multiple reflectors. Two-dimensional (time and delay) temporal properties of the **V2V-VLC** channel is studied under dynamic traffic conditions at different times of the day.

Chapter 6 estimates the probability of co-existence of other vehicles in the adjacent lanes using real-time traffic measurements. Considering the existence of other vehicles in the adjacent lanes, the **SNR** and **BER** performance of the **V2V-VLC** channel is examined on different Lanes.

Chapter 7 summarises the main research findings and conclusions. This chapter also suggests areas of future works.

Chapter 2

Vehicle-to-Vehicle Visible Light Communications Channel

Any communication system consists of three main parts; transmitter, receiver and communication channel between transmitter and receiver. Studying communication channels is the first step in designing a robust and reliable communication system. In [VLC](#) systems, channel modelling depends on many factors, such as transceiver location and separation, link configuration ([LOS/NLOS](#)), surrounding environment, employed optical devices and geometry of communication link. In addition, in a dynamic environment, the transmitter and the receiver movement follows an unsystematic pattern, which adds a factor of randomness to the communication system performance.

This chapter provides the technical background and fundamental principles required in subsequent chapters to create [V2V-VLC](#) channel models to investigate the impact of motion for transmitters and/or receivers in realistic outdoor environments.

The chapter is organised as follows: the related works, which reviewed [V2V-VLC](#) channel models and the effects of weather conditions, are provided in [Section 2.1](#). The discussion of the [V2V-VLC](#) channel model is provided in [Section 2.2](#). A chapter summary is given in [Section 2.3](#).

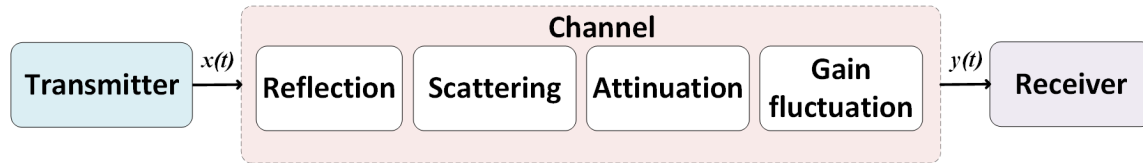


Figure 2.1: A communication system with examples of channel impairments that distort the transmitted signal.

2.1 Related Works

A typical communication system is depicted in Figure 2.1. The figure shows examples of channel impairments that distort the transmitted signal. Therefore, research efforts have been devoted to find a model that best describes **VVLC** channel, including **vehicle-to-vehicle (V2V)** and **vehicle-to-infrastructure (V2I)** structure channels. However, **VVLC** is a complex system and the channel is affected by the variable geometry of the link due to the mobility and radiation pattern of vehicles' sources. In addition, it is affected by the interaction of optical signal with objects of different sizes which causes scattering and reflection.

2.1.1 Vehicle-to-vehicle visible light channel modelling

Previous studies have utilised different approaches and methods to model the **VVLC** channel. A classification of the available channel modelling approaches and methods is shown in Figure 2.2. Channel modelling approaches are classified into deterministic and stochastic (Al-Kinani, Wang, Zhou and Zhang, 2018). The stochastic channel modelling approach considers a time-varying statistical channel model (Papoulis et al., 2002, P. 285). It models the randomness of the communication link geometry as a function of time. As a result, this model provides a statistical distribution that can describe the channel (Al-Kinani, Wang, Zhou and Zhang, 2018). Analytical-based methods, which are validated by simulation-based methods, are used to study stochastic channel models.

The deterministic channel models incorporate a detailed description of the communication link under study. It includes the position and orientation of transmitter and receiver, the

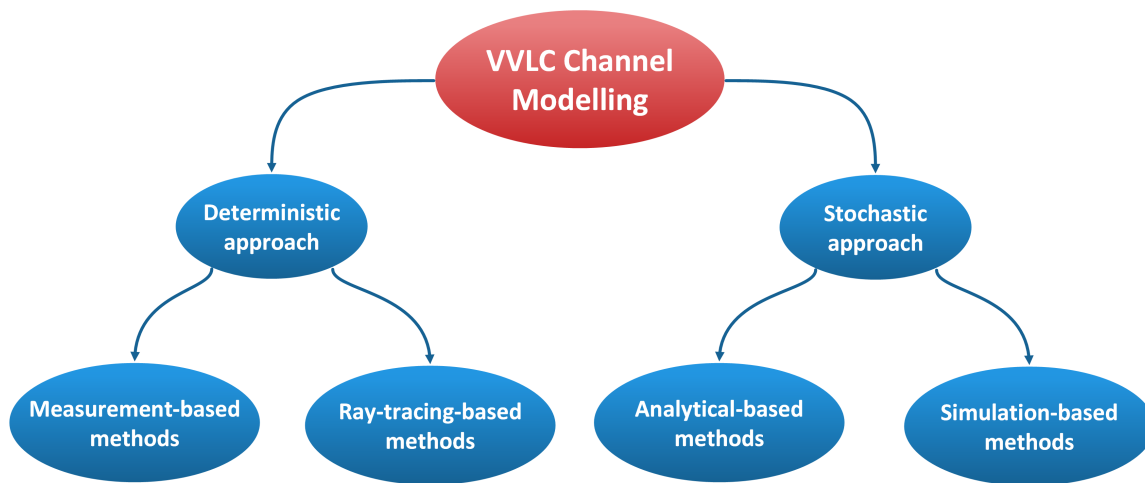


Figure 2.2: A classification of channel modelling approaches and methods.

presence of other objects and the properties of surrounding surfaces (Al-Kinani, Wang, Zhou and Zhang, 2018). Measurement-based and ray-tracing-based channel modelling methods are used to study deterministic channel models.

2.1.1.1 Ray-tracing-based channel modelling

Optical ray-tracing software packages and tools are used to model and examine the performance of VVLC systems. Ray-tracing is a rendering technique that accounts for traces and interactions of a large number of optical rays generated by a source for each receiving point individually. The available packages can accurately mimic realistic radiation patterns of optical sources. Furthermore, they describe the rays' interactions with the surfaces of different materials and physical states. Ray-tracing software are widely utilised to investigate optical phenomena including reflection from surrounding object surfaces, refraction and diffraction due to optics and scattering due to weather conditions.

Lee et al. (2012b) simulate the radiation pattern of vehicles' sources and reflection using LightTools software to study channel impulse response (CIR) and the temporal properties of the VVLC channel. The simulation considered the reflection from the surrounding vehicles and building. However, the study did not provide a reproducible CIR formula.

Relying on ray-tracing software OpticStudio®, Elamassie et al. (2018) used a curve-fitting

technique to derive a **VVLC** path-loss model. The model considered the effect of weather on the **VVLC** channel. In the proposed model, path-loss decays linearly with the inter-vehicle spacing. Similarly, using OpticStudio® and curve-fitting technique, [Eldeeb et al. \(2019\)](#) described the path-loss model for **V2V** channels as exponentially decaying with the inter-vehicle spacing. Both studies considered a deterministic inter-vehicle spacing limited to 20-50 m. None of these studies considered the dynamic variation of the traffic conditions and inter-vehicle spacing during different times of the day.

[Karbalyghareh et al. \(2020\)](#) modified the model proposed by [Poliak et al. \(2012\)](#) to describe the **VVLC** channel. The proposed model combined the effect of geometrical path-loss and scattering effect due to hydrometry weather conditions. [Karbalyghareh et al. \(2020\)](#) used ray-tracing software OpticStudio® to simulate vehicles headlight radiation pattern to validate the proposed model.

Ray-tracing tools provide an important option to study **VVLC** channels. However, the resultant accuracy of the model depends on the simulation parameters ([Memedi and Dressler, 2021](#)).

2.1.1.2 Measurement-based channel modelling

The **VVLC** systems are complex and involve various elements that add random factors to the channel behaviour. Hence, a number of measurements campaigns have investigated **VVLC** channel behaviour and tested the **VVLC** systems performance.

[Kim et al. \(2015\)](#); [Eso et al. \(2019\)](#); [Avătămăniței, Căilean, Done, Dimian and Popa \(2020\)](#) conducted experimental studies to examine the impact of weather conditions on the **VVLC** channel model. [Uyrus et al. \(2019\)](#); [Memedi et al. \(2018\)](#); [Viriyasitavat et al. \(2013\)](#) investigated the **VVLC** channel model associated with the radiation pattern of vehicles' sources. [Chen et al. \(2016\)](#); [Hua-Yen Tseng et al. \(2015\)](#); [Cui et al. \(2014\)](#); [Torres-Zapata et al. \(2020\)](#); [Béchadergue et al. \(2019\)](#); [Turan et al. \(2018\)](#) measured different channel parameters to study the performance of **VVLC** systems.

According to [Cheng et al. \(2018\)](#), the measurement-based method is a preferable channel

modelling approach. It provides a comprehensive and highly realistic description of the VVLC channel. However, the majority of the empirical studies did not provide reproducible models or formulas that can be used to investigate and design a reliable communication system.

2.1.1.3 Analytical and simulation-based channel modelling

Many studies established analytical models to describe the VVLC channel and system performance. The analytical models relied on simulation tools to simulate the vehicles' interactions and their interactions with the environment. Simulation approaches used to validate theoretical findings, include MC simulation (Al-Kinani, Sun, Wang, Zhang, Ge and Haas, 2018), SPCTRAL2 simulation (Lee et al., 2009), simulation of urban mobility (SUMO) and OMNET simulations (Khoder et al., 2020; Masini et al., 2017), VISSIM and SHINE (Masini et al., 2017) and vehicular network open simulator (VENETOS) (Ucar et al., 2018a).

Many analytical-based works used the Lambertian model to describe the VVLC channel model. Al-Kinani, Sun, Wang, Zhang, Ge and Haas (2018); Abualhoul et al. (2018); Béchadergue et al. (2019); Esmail et al. (2017); Chen and Wang (2020) used the Lambertian model as an acceptable theoretical description for the VVLC channel. However, Cui et al. (2014); Viriyasitavat et al. (2013); Chen et al. (2016); Abuella et al. (2019); Hua-Yen Tseng et al. (2015) criticised the employment of the Lambertian model because the asymmetrical radiation pattern of the vehicles sources.

The research work in (Lee et al., 2009) studied VVLC system performance under high optical noise due to daylight. Khoder et al. (2020) used an analytical model to investigate the impact of interference from neighbouring vehicles. Similarly, the theoretical study in (Singh et al., 2020) investigated the effect of interference from nearest vehicles under different weather conditions. Likewise, Singh et al. (2019); Zaki et al. (2019) examined the impact of weather conditions on VVLC systems performance.

Al-Kinani, Sun, Wang, Zhang, Ge and Haas (2018); Al-Kinani et al. (2020) established

two-dimensional and three-dimensional geometry-based stochastic models to describe the LOS and reflection components of the VVLC channel, respectively. Luo, Ghassemlooy, Bentley, Burton and Tang (2015); Luo, Ghassemlooy, Minh, Bentley, Burton and Tang (2015) examined the impact of reflection from road surface for VVLC systems that use on-off-keying (OOK) modulation and multiple-input-multiple-output (MIMO) schemes, respectively. Memedi et al. (2017) considered a realistic radiation pattern of vehicles' headlights to derive an analytical model of VVLC channel path-loss. The model relied on empirical measurements carried out by Hua-Yen Tseng et al. (2015).

In conclusion, analytical studies can provide vital reproducible models to study complex systems. An analytical study that investigates the mobile VVLC systems considering the dynamic nature of traffic and vehicles density is required to establish a reproducible channel model. The following section provides the related work that studied the impact of weather conditions on the VVLC channel.

2.1.2 Impact of weather conditions

The atmosphere is composed of a mixture of gases with atoms and molecules of different sizes, in addition to suspended particles called aerosols. The interaction between these particles and light rays results in power fading due to absorption and scattering (Naboulsi et al., 2005). The outdoor VLC channel is prone to adverse weather conditions that attenuate the optical signal. Possible VVLC channel impairments due to different weather conditions are illustrated in Figure 2.3.

Previous research has considered the impact of different weather condition while using different types of receivers.

Kim et al. (2001) studied the atmospheric attenuation due to scattering and absorption on free-space OWC. The scattering dominates the attenuation while the absorption contributes less to the total attenuation. Unlike the previous models, Kim et al. (2001) indicated that the scattering depends on the size of the atmospheric particles. The Rayleigh model was proposed to describe scattering due to particles with a size less than the light wavelength,

This item has been removed due to 3rd Party Copyright. The unabridged version of the thesis can be viewed at the Lanchester Library, Coventry University.

This item has been removed due to 3rd Party Copyright. The unabridged version of the thesis can be viewed at the Lanchester Library, Coventry University.

(a)

(b)

(c)

(d)

Figure 2.3: Possible VVLC channel impairment due to a) rain ([Sakhastka/Getty, 2021](#)), b) fog ([Singh/National, 2015](#)), c) haze ([Lee/Reuters, 2017](#)) and d) snow-fall ([Hanacekl, 2018](#)).

such as air molecules. Mie model was proposed to describe scattering from particles with a size comparable to the wavelength of the light, such as haze and light fog. Geometrical/Non-selective model was proposed to describe scattering from particles with a size larger than the wavelength of the light, such as dense fog, heavy rain and snow. Figure 2.4 illustrates scattering models according to particle size. Weather conditions (e.g., fog, rain and snow) that reduce the visibility range to less than 500 m affect short-distance links, while haze with visibility ranges over 2 km affects long-distance transmissions. Using Beer-Lambert scattering, [Kim et al. \(2001\)](#) established a piecewise expression to describe the wavelength-dependency of the atmospheric attenuation according to particles sizes. The Beer-Lambert scattering model assumes that the receiver cannot capture the scattered photons.

The experimental study in ([Kim et al., 2015](#); [Eso et al., 2019](#)) used the attenuation model suggested by [Kim et al. \(2001\)](#) to study the attenuation due to fog for car-to-car communications. [Kim et al. \(2015\)](#) used a red LED as a transmitter and a photodiode

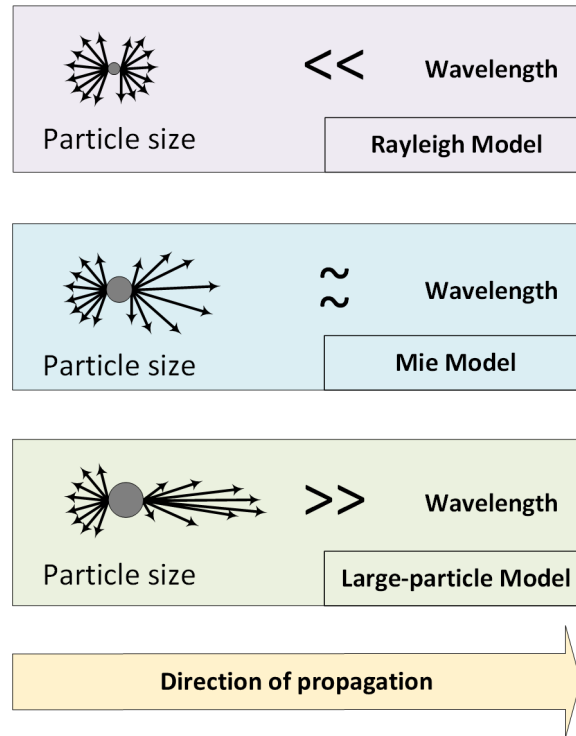


Figure 2.4: Scattering models according to particle size.

(PD) receiver. The results showed that **VVLC** links are severely impaired by fog attenuation. However, reliable communication performance is achievable using Fresnel optic at the receiver. [Eso et al. \(2019\)](#) used Nissan red taillight as a transmitter and Canon Rebel camera as a receiver. The results showed that reliable communication is possible under foggy conditions with a visibility range of 20 m.

[Singh et al. \(2019\)](#); [Singh et al. \(2018\)](#) investigated the effect of weather conditions on the **VVLC** channel. The study considered a **PD** receiver and Beer-Lambert model to examine the power attenuation due to rain, dense fog, light fog, wet snow and dry snow. Among the studied weather conditions, dry snow induces the highest power attenuation value of 131 dB/km, followed by a dense fog that induce 78.8 dB/km. The wet snow has the lowest power attenuation value of 19.86 dB/km. [Zaki et al. \(2019\)](#) studied the effect of rain, wet snow and dry snow for **V2I** system when a single **avalanche PD (APD)** is the receiver. The study considered the Beer-Lambert model to describe the scattering, and it used Marshall, France and Japan models to quantify the rain attenuation. The results showed that dry snow has the

severest impact on the VVLC system, confirming the findings in (Singh et al., 2019; Singh et al., 2018). The results also showed that the Japan model describes the attenuation due to rain accurately compared to the other models. Similarly, the empirical work in (Avătămăniței, Căilean, Done, Dimian and Popa, 2020) examined the impacts of snowfall and blizzard on VVLC systems. The study showed that the blizzard significantly impairs the performance of the VVLC link.

A number of simulation studies have investigated the effect of clear weather, rain, light fog and dense fog on the VVLC channel. Elamassie et al. (2018) quantified the impact of the weather conditions on the channel path-loss, BER and maximum achievable distance using a PD receiver. The study relied on the Mie scattering model regardless of the size of the atmospheric particles. The results show that rain, light fog, and heavy fog reduce the transmission distance by 95%, 73% and 37%, respectively. Similarly, Karbalayghareh et al. (2019) studied the effect of weather conditions on the VVLC channel when a single-photon avalanche diode (SPAD) acts as a receiver. The results showed that the SPAD receiver enhances the BER performance of VVLC and increase the achievable transmission range under the most severe weather conditions compared to PD.

Ebrahim and Al-Omary (2017) studied the effect of different densities of sandstorms on VVLC performance. The results revealed that low-density sandstorms reduces the range of acceptable communication link to 350 m whereas a high-density clay storm reduces it to as low as 90 m.

Research works that studied the impact of weather conditions on VVLC systems are summarised in Table 2.1.

Well-established models that quantify the weather impact are available in the literature. None of the previous studies considered the effect of weather conditions for dynamic V2V-VLC systems to provide a reproducible statistical channel model to design VVLC systems. Therefore, the following sections explain the required technical background of V2V-VLC channel modelling to obtain a reliable mathematical formula that can describe V2V-VLC channel under different weather conditions.

Table 2.1: *Summary of research works that studied the weather conditions on VVLC systems.*

Ref.	Weather condition	Scattering model	Receiver
Kim et al. (2015)	fog	Kim model	PD and Fresnel optic
Eso et al. (2019)	fog	Kim model	Camera
Elamassie et al. (2018)	fog and rain	Mie model	PD
Karbalayghareh et al. (2019)	fog and rain	Mie model	SPAD
Karbalayghareh et al. (2020)	fog and rain	modified Beer Lambert model	PD
Singh et al. (2019) Singh et al. (2018)	fog, rain and snow	Beer-Lambert model	PD
Ebrahim and Al-Omary (2017)	sand storms	Rayleigh and Mie models	PD
Zaki et al. (2019)	fog and rain	Beer-Lambert	APD
(Avătămăniței et al. 2020)	snowfall and blizzard	Experimental measurements	PD

2.2 V2V-VLC Channel Model

Dynamic **V2V-VLC** channel modelling is challenging because it depends on the harsh outdoor environment with adverse weather conditions and ambient noise.

The dynamic **V2V-VLC** channel is influenced by: a) link geometry characterised by inter-vehicle spacing and angle deviation that are changing due to the dynamic traffic conditions, b) the radiation pattern of light sources ([Cheng et al., 2018](#); [Abuella et al., 2019](#)), c) multipath signal propagation due to reflections from surrounding reflective objects and vehicles, d) additional power attenuation due to weather conditions ([Kim et al., 2015](#); [Hu et al., 2007](#)) and e) additive noise sources, which includes ambient and shot noises ([Béchedergue et al., 2019](#);

Luo, Ghassemlooy, Minh, Bentley, Burton and Tang, 2015). Hence, the received signal $y_r(t)$ at any time instance is given by:

$$y_r(t) = \gamma h_T(t) \otimes x_t(t) + n_o(t), \quad (2.1)$$

where \otimes denotes convolution, $x_t(t)$ is the transmitted optical signal, $h_T(t)$ is CIR, γ is receiver responsivity and $n_o(t)$ is the additive white Gaussian noise (AWGN) process, which combines the effect of the shot and thermal noise. The noise is white, i.e. has uniform gain across the spectrum. However, its impact on the received signal is limited by the bandwidth B_w of the electrical filter that follows the photodetector (Ghassemlooy et al., 2019, P.463). Therefore, total noises variance σ_{total}^2 of $n_o(t)$ is given by:

$$\sigma_{total}^2 = \sigma_{shot}^2 + \sigma_{th}^2, \quad (2.2)$$

where σ_{shot}^2 is the shot noise which is induced by the ambient lighting from the natural and artificial optical sources, and it is given by (Ghassemlooy et al., 2019):

$$\sigma_{shot}^2 = 2q(P_R + P_I)\gamma B_w + 2qI_{bg}I_2B_w, \quad (2.3)$$

and σ_{th}^2 is the thermal noise, which is given by (Ghassemlooy et al., 2019):

$$\sigma_{th}^2 = \frac{8\pi K_p T_a C_{pd} A_r I_2 B_w^2}{G_\nu} + \frac{16\pi^2 K_p T_a \Gamma_k C_{pd}^2 A_r^2 I_3 B_w^3}{g_m}. \quad (2.4)$$

The definitions of the parameters of (2.3) and (2.4) are given in Table 2.2.

The total CIR $h_T(t)$ accounts for geometrical propagation effects $h(t)$ and the weather conditions effects h_w , and is given by:

$$h_T(t) = \gamma h(t) h_w. \quad (2.5)$$

The effect of the weather is discussed in the following subsection. In section 2.2.2, the geometrical propagation effect is presented.

2.2.1 Impact of weather conditions

An optical signal travelling through free space is prone to absorption and scattering by suspended atmospheric particles such as gaseous molecules and water droplets (Ghassemlooy

Table 2.2: Parameters of (2.3) and (2.4).

Symbol	Parameter
P_R	Received power
P_I	Interference power
q	Electron charge
γ	PD responsivity
K_p	Boltzmann's constant
T_a	Absolute temperature
A_r	Receiver area
C_{pd}	PD capacitance per unit area
I_2	Noise bandwidth factor
I_3	Noise bandwidth factor
B_w	Noise bandwidth
G_v	Open-loop voltage gain
Γ_k	FET channel noise factor
g_m	FET transconductance
I_{bg}	Background current (Silicon PD)
ρ	Reflection index

et al., 2019; Esmail et al., 2017; Zaki et al., 2019, P. 105). Therefore, weather conditions such as rain and fog can severely degrade the quality of the optical signal resulting in communication system outage (Zaki et al., 2019).

Weather conditions induce a wavelength-dependent power attenuation of optical signals, and hence, limit the visibility ranges of VVLC links. Kim et al. (2001) proposed a model which was adopted to describe weather attenuation in V2V-VLC channel by experimental studies Kim et al. (2015); Eso et al. (2019). The CIR component of weather conditions h_w depends on the visibility range l_v (Kim et al., 2001; Kim et al., 2015):

$$h_w = e^{-l_v \Gamma(\lambda)}, \quad (2.6)$$

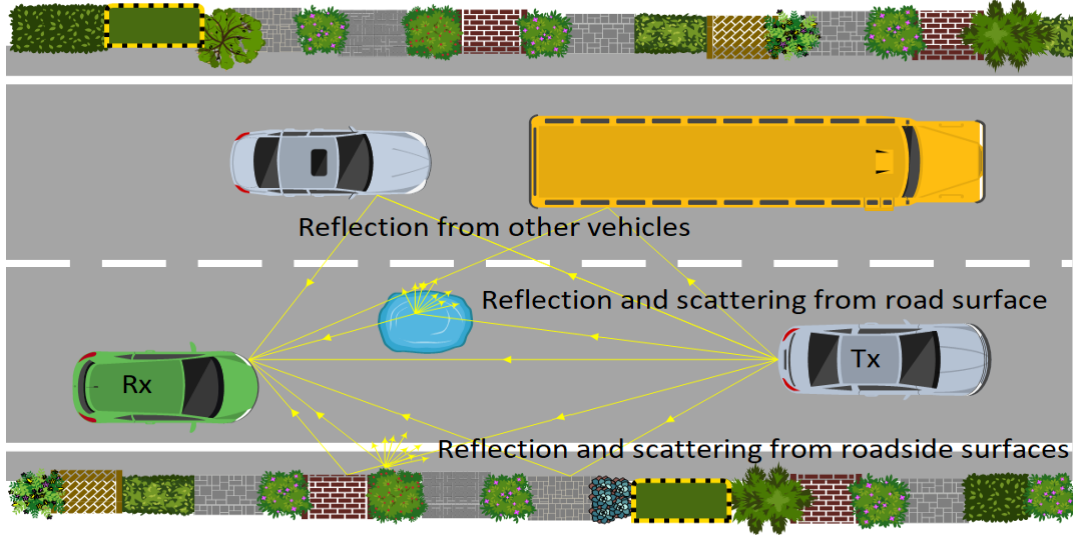


Figure 2.5: Illustration of multipath propagation of the optical signal between transmitter and receiver vehicles due to reflection and scattering from other vehicles, road surface and roadside objects.

where $\Gamma(\lambda)$ (in dB/km) is the attenuation coefficient due to different weather conditions. The coefficient $\Gamma(\lambda)$ is a function of the light wavelength λ and visibility range l_v (Kim et al., 2015; Hu et al., 2007):

$$\Gamma(\lambda) = \frac{17.35}{l_v} \left(\frac{\lambda}{550} \right)^{-\eta}, \quad (2.7)$$

where η is a visibility range dependent parameter. Weather conditions and the geometrical propagation of the optical signal are independent events. The effect of weather conditions on the statistical characteristic of V2V-VLC channel under dynamic traffic conditions is investigated in Section 4.3. In the following section, the geometrical propagation effect on the V2V-VLC channel is discussed.

2.2.2 Geometrical propagation effect

V2V-VLC channel can be described as a multipath channel. The signal travels from the transmitter to the receiver over multiple paths, with each propagation path associated with a reflector object (Goldsmith Andrea, 2005, P. 64), as shown in Figure 2.5. The figure shows

multipath propagation of the optical signal between the transmitter and receiver vehicles due to reflection and scattering from other vehicles, road surface and roadside objects, and hence, the figure shows the significance of studying the reflection from different road objects and surfaces and identifying the probability of the existence of other vehicles (as it is detailed in Chapter 5 and Chapter 6). Considering the electro-optical conversion, the transmitted optical signal $x_t(t)$ in (2.1) is given as $x_t(t) = g_t u(t)$, where g_t is the optical gain of the transmitter and $u(t)$ is the equivalent electrical baseband transmitted signal (Hranilovic, 2005, P. 40). Without loss of generality, neglecting additive noise, the received signal is given as a sum of randomly attenuated and time-delayed copies of the transmitted signal (Rappaport, 2002; Goldsmith Andrea, 2005, P. 183, P. 65) which is given as:

$$y(t, \tau) = \sum_{j=0}^{J_r} \alpha_j(t) u(\tau - \tau_j(t)), \quad (2.8)$$

where J_r is the total number of reflectors. $\alpha_j(t)$ is the amplitude and $\tau_j(t)$ is the propagation delay of the j^{th} propagation path of the signal. The propagation path $j = 0$ corresponds to the LOS component of the channel. The amplitude $\alpha_j(t)$ is associated with the path-loss of the NLOS component of the channel when each NLOS component associated with a single j^{th} reflector (Goldsmith Andrea, 2005, P. 65).

The received signal is given by the convolution between the equivalent electrical baseband signal $u(t)$ and the CIR $h(t)$ as below:

$$y_r(t) = \int_{-\infty}^{\infty} h(t, \tau) u(t - \tau) d\tau. \quad (2.9)$$

The two dimensional time-variant CIR is given by:

$$h(t, \tau) = \sum_{j=0}^{J_r} \alpha_j(t) \delta(\tau - \tau_j(t)), \quad (2.10)$$

where $\delta()$ is the Dirac delta function.

Therefore, the CIR component for the geometrical propagation effect $h(t)$ combines a LOS component $h_{LOS}(t)$ when $j = 0$ and a NLOS multipath component $h_{NLOS}(t)$ when $j = 1 \dots J_r$, which is given as:

$$h(t) = h_{LOS}(t) + h_{NLOS}(t). \quad (2.11)$$

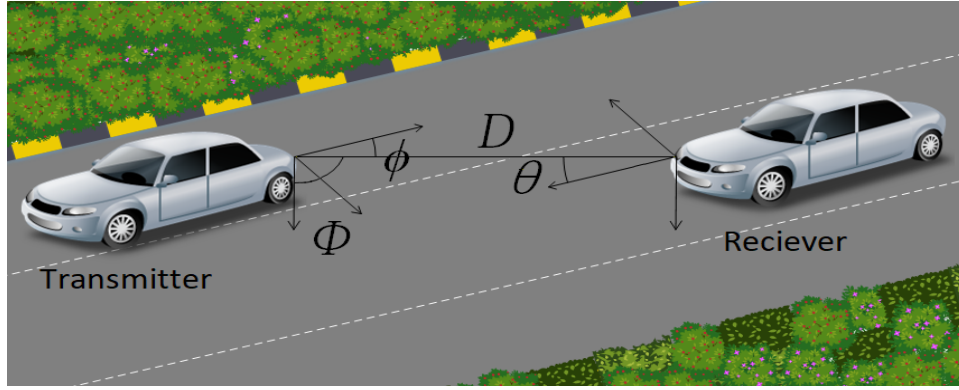


Figure 2.6: Illustration of three-dimensional geometry of V2V-VLC link.

Due to the unpredicted movement pattern of transmitters and receivers, the CIR of the V2V-VLC link changes spatially. The following sections discuss the impact of unpredicted movement pattern on the LOS and NLOS components of the CIR, the temporal properties due to multipath propagation and the BER performance of the communication link.

2.2.2.1 LOS component

The CIR of the LOS component $h_{LOS}(t)$ is influenced by the three-dimensional radiation intensity distribution $I(\phi, \Phi)$ of the light sources. The radiation irradiance distribution (or illuminance) (W/m^2) at distance D is given by (Ghassemlooy et al., 2019; Luo, Ghassemlooy, Minh, Bentley, Burton and Tang, 2015; Moreno and Sun, 2008):

$$E(\phi, \Phi, \theta) = \frac{I(\phi, \Phi) \cos(\theta)}{D^2}, \quad (2.12)$$

where ϕ is the azimuth (horizontal) irradiance angle, Φ denotes the elevation (vertical) irradiance angle and θ represents the incident angle, as illustrated in Figure 2.6.

Assuming a receiver with an area of A_r , an optical filter of $T_S(\theta)$ gain and a concentrator of $g_S(\theta)$ gain, then the CIR of the LOS component is given by (Cheng et al., 2018):

$$h_{LOS}(t) = \frac{I(\phi, \Phi)}{D^2} A_r T_S(\theta) g_S(\theta) \cos(\theta) \delta\left(t - \frac{D}{c}\right), \quad (2.13)$$

where c is the speed of light and D/c represent the propagation delay of the signal. However, assuming the alignment between vehicles headings (i.e., $\phi = \theta$) and a unit gain of the optical filter and a concentrator, the CIR of the LOS component is simplified as:

$$h_{LOS}(t) = \frac{I(\phi, \Phi)}{D^2} A_r \cos(\phi) \delta\left(t - \frac{D}{c}\right). \quad (2.14)$$

The DC gain of the **LOS** component of the channel $H_{LOS}(0)$ is given by:

$$H_{LOS}(0) = \int_{-\infty}^{\infty} h_{LOS}(t) dt. \quad (2.15)$$

According to [Chen et al. \(2016\)](#), the vertical movement of vehicles due to irregular road surface results in a sudden change in the received power of less than 5 dB for a short time duration that does not exceed 0.5 s. Therefore, the alignment between the receiver and transmitter is assumed for most of the driving time. Hence, the elevation irradiance angle Φ is considered constant. As a result, channel gain in decibels (dB) P_L (i.e. channel path-loss) is given by:

$$P_L = 10 \log(A_r) + 10 \log(I(\phi) \cos(\phi)) - 20 \log D. \quad (2.16)$$

The **LOS** component depends on the geometry of the communication link given by the distance D and angle ϕ , which change continuously in dynamic systems. The impact of dynamic traffic on the inter-vehicle spacing D is investigated in Chapter 3 to estimate the statistical distribution that describes the variation of D and the channel path loss, considering spatial variation only. The spatial and angular (i.e., D and ϕ) variation due to dynamic traffic and vehicles' sources radiation pattern is discussed in Chapter 4. In the following section, the **NLOS** component of the channel due to multipath propagation is discussed.

2.2.2.2 NLOS component

The optical signal experiences multiple reflections and scattering from the surfaces of the surrounding objects, which affects the received power and the temporal properties of the optical signal as given in (2.10).

Figure 2.7 shows a **LOS** link between two vehicles A and B along with an **NLOS** link due to reflection from vehicle j . Considering a Lambertian diffuse reflection, the **CIR** from J_r reflectors is given as ([Huang et al., 2017](#)):

$$h_{NLOS}(t) = \sum_{j=1}^{J_r} \frac{\rho A_r h_{NLOS_j}(t)}{2\pi r_j^2} \cos(\phi_s^j) \cos(\theta_R^j) \delta\left(\frac{t - (r_j + r_1)}{c}\right), \quad (2.17)$$

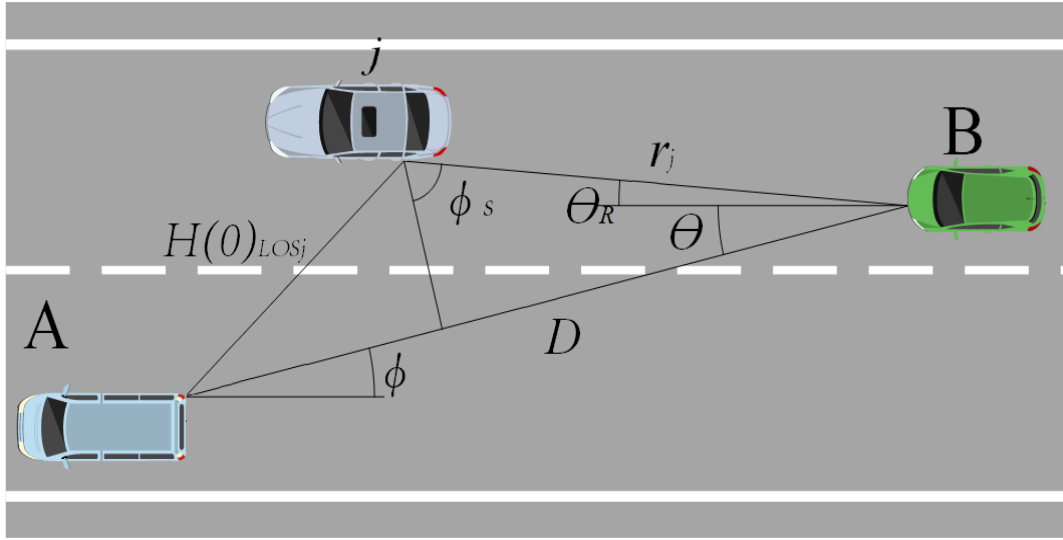


Figure 2.7: Illustration of a communication link between two vehicles A & B and NLOS component due to reflection from vehicle j .

where $h_{LOS_j}(t)$ is the **LOS CIR** from the source to the j^{th} reflector, ϕ_s is the angle of irradiance with respect to the normal to the reflector, θ_R is the incidence angle at the receiver, r_1 and r_j are the distances from the transmitter to the reflector and from the reflector to the receiver, respectively. Consequently, the DC gain of the **NLOS** component is given as:

$$H_{NLOS}(0) = \sum_{j=1}^{J_r} \frac{\rho A_r H_{LOS_j}(0)}{2\pi r_j^2} \cos(\phi_s^j) \cos(\theta_R^j). \quad (2.18)$$

The **NLOS** component also depends on the geometry of the communication link given by the distance and angles between transmitter, reflector and receiver. Chapter 5 discusses the impact of the geometrical changes on the **NLOS** component of a dynamic **V2V-VLC** channel to establish statistical distributions that describe the **NLOS** component of a dynamic **V2V-VLC** channel when single and multiple reflectors are considered. The following section introduces the temporal properties of the **V2V-VLC** channel.

2.2.2.3 Temporal properties

In a multipath channel, the optical signal experiences delays with a duration that depends on the propagation path length (Al-Kinani, Wang, Zhou and Zhang, 2018). As a result, the

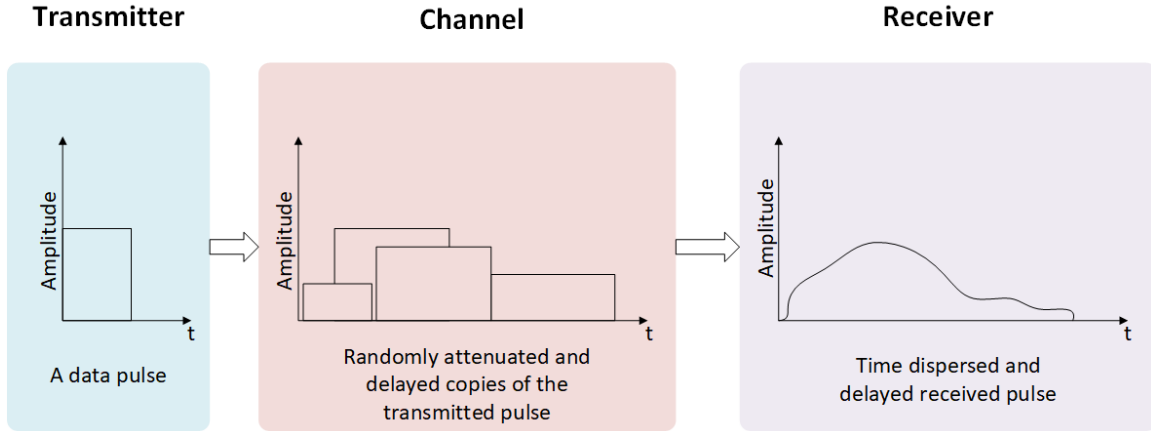


Figure 2.8: Effect of multipath propagation on the transmitted signal.

received signal is a time dispersed copy of the transmitted signal as illustrated in Figure 2.8. Therefore, if a train of pulses is transmitted, then due to the time dispersion of each pulse-width, *inter-symbol-interference (ISI)* can occur (Goldsmith Andrea, 2005; Rappaport, 2002, P. 83, P. 207). Time parameters, including the mean excess delay, the *root-mean-square (RMS)* delay and the two-dimensional autocorrelation function quantify the temporal properties of the multipath channel.

The time dispersion parameters, mean excess delay and the *RMS* delay, characterise the temporal pulse broadening due to multipath propagation. The time parameters of the multipath channel are identified from the power delay profile of the channel which is provided by (Goldsmith Andrea, 2005; Rappaport, 2002, P. 86, P. 185):

$$P_d(t, \tau) = h(t, \tau). \quad (2.19)$$

The mean excess delay τ_{excess} of the channel is the first central moment of the power delay profile given by (Rappaport, 2002; Goldsmith Andrea, 2005, P.199, P. 70):

$$\tau_{excess} = \frac{\int \tau P_d(\tau) d\tau}{\int P_d(\tau) d\tau}. \quad (2.20)$$

The *RMS* delay spread σ_{rms} of the channel is the square root of the second central moment of the power delay profile, and it is given by (Ghassemlooy et al., 2019)

$$\sigma_{rms} = \sqrt{\frac{\int (\tau - \tau_{excess})^2 P_d(\tau) d\tau}{\int P_d(\tau) d\tau}}. \quad (2.21)$$

Table 2.3: Matrix of channel classification depending on the time parameters of the channel and the transmitted signal properties.

	Slow Fading	Fast fading
Frequency selective fading	$B_s > B_c$	$B_s > B_c$
	$T_s < \sigma_{rms}$	$T_s < \sigma_{rms}$
	$B_s > B_D$	$B_s < B_D$
	$T_s < T_c$	$T_s > T_c$
Flat fading	$B_s < B_c$	$B_s < B_c$
	$T_s > \sigma_{rms}$	$T_s > \sigma_{rms}$
	$B_s > B_D$	$B_s < B_D$
	$T_s < T_c$	$T_s > T_c$

The RMS delay spread of the channel σ_{rms} is reciprocal to the channel coherence bandwidth B_c (Al-Kinani, Wang, Zhou and Zhang, 2018):

$$\sigma_{rms} = \frac{1}{5B_c}. \quad (2.22)$$

If the bandwidth of the signal B_s is less than the coherence bandwidth B_c of the channel and the symbol time duration T_s is larger than the RMS delay spread σ_{rms} of the channel, then the channel undergoes a flat fading (Rappaport, 2002; Goldsmith Andrea, 2005, P. 206, P. 89). Otherwise, the channel undergoes a frequency selective fading, which induces ISI (Rappaport, 2002; Goldsmith Andrea, 2005, P. 83, P. 207), see Table 2.3. In the frequency selective fading, specific frequencies of the signal spectrum pose a larger gain than others because the received signal consists of a combination of multiple attenuated and timed delayed copies of the original signal (Rappaport, 2002, P. 207). In the flat fading, the channel gain fluctuates, and hence, the amplitude of the received signal changes with time, while the spectral characteristics of the signal are preserved (Rappaport, 2002, P. 205).

The two-dimensional autocorrelation function determines the time statistical characterization of the channel and the time stationary properties and coherence time of the channel (Goldsmith Andrea, 2005, P. 71) and it is given by:

$$A_c(t; \tau) = \mathbf{E}[h(t, \tau)h^*(t, \tau)], \quad (2.23)$$

where $h^*(t, \tau)$ is the complex conjugate of the CIR. Note that, the **Intensity Modulation/Direct Detection (IM/DD) VLC** system only deals with real and positive signals.

The autocorrelation function offers information about the time variation of a dynamic channel due to the relative motion of objects (Goldsmith Andrea, 2005, P. 71-72). The channel is considered **wide sense stationary (WSS)** when the joint statistics of the channel measured at t and $t + \Delta t$ are time-independent, i.e. depends on the time difference Δt only. Furthermore, the channel is considered to have **uncorrelated scattering (US)** when a multipath component of a delay τ_1 is uncorrelated with another multipath component of a delay τ_2 , and $\tau_1 \neq \tau_2$. Hence, this means that the two components are caused by different scatterers (Goldsmith Andrea, 2005, P. 85). Therefore, the channel is known as the **WSS-US** channel. Furthermore, the channel is considered nonstationary if the autocorrelation function depends on the propagation delay (or propagation time difference) τ .

This work uses the autocorrelation function to identify the coherence time of the channel T_c , which is defined as the time duration over which the autocorrelation function is not zero. After T_c seconds, the time-varying channel decorrelates. The coherence time is also reciprocal to the Doppler spread of the channel:

$$T_c = \frac{1}{B_D}. \quad (2.24)$$

If the bandwidth of the signal B_s is larger than the Doppler spread B_D of the channel and the channel coherence time T_c is larger than the symbol time duration T_s , the channel is classified as slow faded (Rappaport, 2002; Goldsmith Andrea, 2005, P. 209, P. 90). Otherwise, the channel is classified as fast faded, see Table 2.3. Fast and slow fading explain the rate of change of the channel impulse response within the symbol duration (Rappaport, 2002; Goldsmith Andrea, 2005).

In Section 5.4, the **RMS** delay spread, two-dimensional autocorrelation function and coherence time of **V2V-VLC** channel are estimated to evaluate the stationary and fading behaviour of the channel.

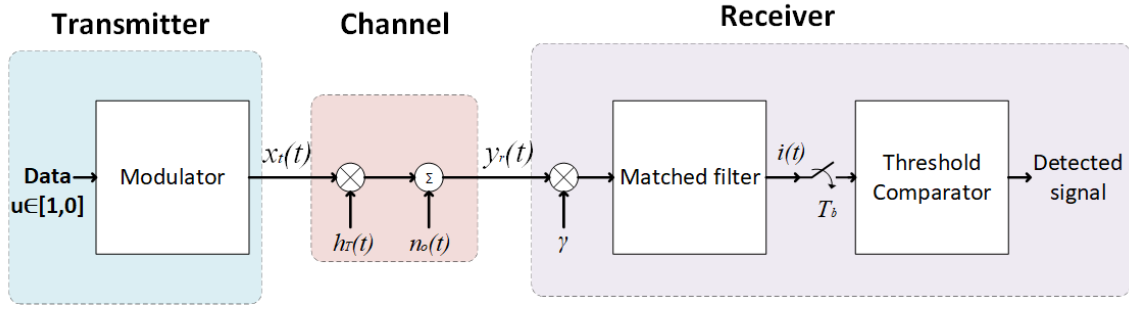


Figure 2.9: Block diagram of a communication system that uses OOK modulation scheme.

2.2.2.4 The performance of V2V-VLC system

The OOK modulation scheme is the most common modulation technique for IM/DD in VLC because it is simple and resilient to the nonlinearity of the LED (Ghassemlooy et al., 2019, P. 164). Therefore, the OOK modulation scheme is adopted in this work for examining the performance of V2V-VLC channel under dynamic traffic conditions. Figure. 2.9 illustrates a block diagram of a communication system that uses OOK modulation. The OOK is a one-dimensional modulation scheme that transmits binary data $u \in [1, 0]$ by an optical pulse $x_t(t)$ which is given by (Ghassemlooy et al., 2019; Hranilovic, 2005, P. 164, P. 52):

$$x_t(t) = \begin{cases} 2P_{avg} & t \in [0, T_b) \quad u = 1 \\ 0 & \quad \quad \quad u = 0 \end{cases}, \quad (2.25)$$

where P_{avg} is the average transmitted power. The transmitted signal is affected by the channel as given in (2.1).

At the receiver, a matched filter is used to demodulate the signal (Proakis, 2001, P. 242). This receiver is a continuous-time filter that has an impulse response that matches the pulse shape of the transmitted signal $x_t(t)$ with an amplitude $1/\sqrt{T_b}$ and duration T_b (Ghassemlooy et al., 2019, P. 173). The output of the matched filter is given by (Proakis, 2001; Sklar et al., n.d., P. 242, P. 108):

$$i(t) = \begin{cases} s + n_o(t) & u = 1 \\ n_o(t) & u = 0 \end{cases}, \quad (2.26)$$

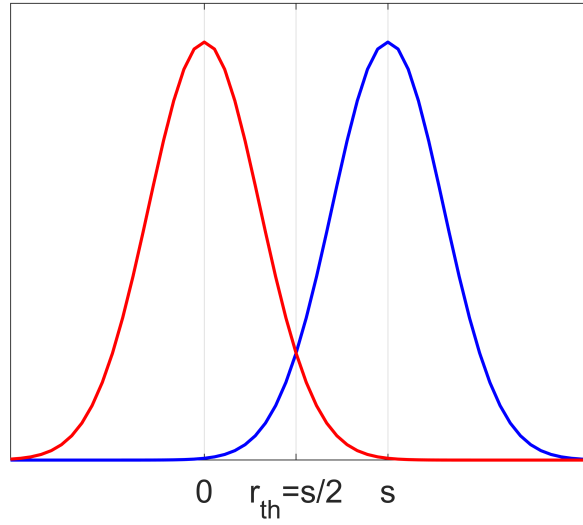


Figure 2.10: Conditional probability density function of OOK modulation signals.

where $s = \sqrt{E_p} = 2\gamma h_T(t) P_{avg} \sqrt{T_b}$ and E_p is peak photocurrent energy. The noise component is Gaussian random variable with **probability density function (PDF)** (Sklar et al., n.d., P. 109):

$$P(n_o) = \frac{1}{\sigma_T \sqrt{2\pi}} \exp\left(-\frac{1}{2} \left(\frac{n_o}{\sigma_T}\right)^2\right). \quad (2.27)$$

Noise variance at the output of the matched filter is $\sigma_T^2 = N_0/2$, where $N_0/2$ is double-sided power spectral density (Sklar et al., n.d., P. 117). Hence, $i(t)$ is a Gaussian random variable with a mean of s when $u = 1$ or a mean of 0 when $u = 0$.

A maximum likelihood detector is employed to decide each pulse interval T_b , such that the probability of correct detection is the maximum and the probability of error is the minimum (Proakis, 2001, P. 242). According to the maximum likelihood detector, the optimum decision threshold of OOK is $r_{th} = s/2 = \sqrt{E_p}/2$, as shown in Figure 2.10.

Under the assumption that the interference increases the shot noise only but does not induce ISI (Ghassemlooy et al., 2019; Sklar et al., n.d., P. 167, P. 215), an error occurs if $i(t) < r_{th}$ while $u = 1$ or if $i(t) > r_{th}$ while $u = 0$. Therefore, the BER is given as (Proakis, 2001; Ghassemlooy et al., 2019, P. 256, P. 168)

$$BER = P(1)P(er/1) + P(0)P(er/0), \quad (2.28)$$

where $P(1)$ and $P(0)$ are the probability of transmitting 1 and 0, respectively. $P(er/1)$ and $P(er/0)$ are the probability of incorrectly decoding the received signal when $u = 1$ and $u = 0$, respectively. Assuming that $P(1)=P(0)=1/2$ when $u = 1$ and $u = 0$ are equally likely then the BER is given as (Proakis, 2001; Ghassemlooy et al., 2019, P. 256,P. 168)

$$BER = \frac{1}{2} \int_{-\infty}^{r_{th}} \frac{1}{\sigma_T \sqrt{2\pi}} \exp\left(-\frac{er^2}{2\sigma_T^2}\right) + \frac{1}{2} \int_{r_{th}}^{\infty} \frac{1}{\sigma_T \sqrt{2\pi}} \exp\left(-\frac{(er-s)^2}{2\sigma_T^2}\right). \quad (2.29)$$

Hence, the BER is given by

$$BER = Q\left(\frac{r_{th}}{\sigma_T}\right), \quad (2.30)$$

where

$$Q(x) = \frac{1}{\sqrt{2\pi}} \int_0^{\infty} e^{-y^2/2} dy. \quad (2.31)$$

Considering the bit energy $E_b = E_p/2$ then $r_{th} = \sqrt{E_p}/2 = \sqrt{E_b/2}$ and $\sigma_T = \sqrt{N_0/2}$, the BER of the system can be re-written as (Ghassemlooy et al., 2019, P. 175)

$$BER = Q\left(\sqrt{E_b/N_0}\right), \quad (2.32)$$

where E_b/N_0 is the SNR per bit at the receiver, which is also given by (Ghassemlooy et al., 2019, P. 166):

$$SNR = \frac{\gamma^2 P_R^2}{\sigma_T^2} = \frac{\gamma^2 H(0)^2 P_T^2}{\sigma_T^2}. \quad (2.33)$$

Therefore, to study the SNR and the associated BER of V2V-VLC systems, modelling the V2V-VLC channel is vital to determine the received power P_R . In Chapter 6 the BER performance of OOK modulation under dynamic traffic conditions is examined. The received power P_R is determined considering the LOS and NLOS components of the V2V-VLC channel in different lanes and during different times of the day.

2.3 Summary

This chapter provided the technical background required to investigate the V2V-VLC channel model and its performance. The movement of the transmitter, receiver and surrounding vehicles adds a factor of randomness to the communication system. The chapter introduced

the **V2V-VLC CIR** that combines the weather and geometrical effects. Focusing on the geometrical description of the channel, the **LOS** and **NLOS** components of the **CIR** were discussed. The analysis showed that the channel model depends on the geometry of the **V2V-VLC** link described by the inter-vehicle spacing and angles. This provided a background to model the inter-vehicle spacing variation due to dynamic traffic in Chapter 3 and establish statistical path loss models for the **LOS** and **NLOS** components in Chapter 4 and Chapter 5, respectively.

Furthermore, this chapter defined the temporal properties of the communications channels that are used in Chapter 5 to evaluate the stationary and fading behaviour of the **V2V-VLC** channel. The **BER** performance of **OOK** discussed in this chapter is used in Chapter 6 to investigate the impact of reflection from other vehicles in the adjacent lanes.

Therefore, the following chapter investigates the impact of dynamic traffic on the **V2V-VLC** channel model, considering a stable queue driving mode with variable inter-vehicle spacing. Chapter 4 investigates the impact of the radiation pattern of vehicles' sources on the **LOS V2V** communication channel, considering dynamic traffic conditions. Chapter 5 discusses the multipath **V2V-VLC** channel model, and Chapter 6 examines the **BER** performance of the **V2V-VLC** channel.

Chapter 3

Impact of Dynamic Traffic on Vehicle-to-Vehicle Visible Light Communications Channel

Chapter 2 has identified that **V2V-VLC** channel modelling should take into account the geometry of the communication link. In particular, the channel path loss depends on the angular distribution of vehicular radiation sources and propagation distance of the optical signal, which varies according to the inter-vehicular distances. The latter is continuously changing due to traffic conditions that affect the mobility of the vehicles. Therefore, studying traffic conditions is vital to establish a statistical model to describe **V2V-VLC** channel path loss.

This chapter considers the inter-vehicular distance variation due to dynamic traffic to develop a statistical path loss channel model. **MC** simulation of 10^6 iterations are used in this chapter to examine similarity between the simulated path loss and the developed statistical distribution of the path loss. The simulation assumes a receiver with an active area A_r of 1 cm^2 and receiver **field of view (FOV)** of 80° , unless otherwise stated. The Kolmogorov-Smirnov test was employed to measure the similarities between simulation and established statistical distributions. The null hypothesis states that a sample from simulation data and a sample from

the established statistical distribution come from a population with the same distribution. The analysis relies on using real-world traffic data collected from the M6 and M42 motorways in the UK. Assuming a stable queue driving scenario with negligible lateral angular deviation between vehicles, the analysis focuses on inter-vehicular distance variation exclusively. The work in this chapter is then extended in Chapter 4 to include both the angular distribution of radiation pattern and the inter-vehicular distance.

The remainder of this chapter is organised as follows: related work are given in Section 3.1. Traffic data analysis and discussion to obtain inter-vehicular distance statistical distribution is provided in Section 3.2. A statistical channel model of channel path loss is discussed in Section 3.3. The chapter summary is given in Section 3.4

3.1 Related works

Only a few studies have considered traffic conditions while studying V2V-VLC systems. Lee et al. (2012b) simulated two stationary urban traffic scenes for metropolitan streets and crossroads using the CATIA V5 tool to study the CIR and time delay of the channel for different stationary scenarios. Tomaš et al. (2014) designed a physical layer model for the discrete-event network simulator JiST/SWANS. The design considered a transceiver model that supports multiple transmitters and receivers transmission to estimate the link geometry and vehicles locations, transmission range and angles. Similar to Lee et al. (2012b), the simulator considered a static network layout.

Ishihara et al. (2015) proposed a hybrid RF/VLC-based message delivery MAC protocol for an autonomous platoon to mitigate RF jamming attacks. Ishihara et al. used network simulator Scenargie® to examine the delay and packet delivery rate of the proposed protocol. However, authors did not provide the simulation parameters considered to simulate the physical layer (channel model) of the VLC-based transmission. Similarly, Ucar et al. (2018a) proposed a security protocol for hybrid RF/VLC-based communications for an autonomous platoon. Ucar et al. used the VENETOS to evaluate the reliability of the proposed protocol. The simulator VENETOS mimics a realistic mobility model of vehicles to study RF-based

vehicular networks. [Ucar et al.](#) extended [VENETOS](#) to consider [VLC](#)-based vehicular networks and vehicle's headlight/taillights radiation pattern. The study focused on the MAC layer and did not provide a reproducible [VLC](#) channel model.

[Masini et al. \(2017\)](#) proposed message delivery with a MAC protocol for full-duplex [VVLC](#) systems. The message delivery rate performance of the proposed protocol was examined using the SHINE simulation platform, a heterogeneous interworking networks, under a dynamic traffic scenario. The vehicular traffic simulator VISSIM was employed to simulate dynamic traffic conditions. The study used the Lambertian model to design the physical layer of the network.

[Khoder et al. \(2020\)](#) studied the performance of a [VLC](#)-based platoon system in the presence of vehicles on the adjacent lanes that induce interference. Traffic was modelled using the vehicular traffic simulator [SUMO](#). The failure probability, throughput, virtual service time and interference activity period of the network were examined using the network simulator OMNET. The study did not provide the physical layer model that was considered to simulate the [VLC](#) channel.

Table 3.1 provides a summary of the research works that considered traffic conditions. The majority of work that considered the dynamic traffic focused on studying the MAC and network layers of vehicular networks. The research works in ([Lee et al., 2012a](#); [Tomaš et al., 2014](#); [Ucar et al., 2018a](#)) that investigated the impact of dynamic traffic conditions on the physical layer of vehicular networks and the [V2V-VLC](#) channel model did not provide a reproducible channel model that can be used to design [VVLC](#) systems. Therefore, this thesis establishes a statistical model of the [V2V-VLC](#) channel path loss, considering the variation in the inter-vehicle spacing at different times of the day. The following section discusses the impact of dynamic traffic on the inter-vehicle spacing relying on traffic data collected from the M42 and M6 motorways in the UK.

Table 3.1: Summary of the research that considered the impact of traffic conditions on VVLC systems.

Ref.	System under study	PHY or MAC layer	Dynamic or static traffic scenario	Simulator
Lee et al. (2012a)	V2V and V2I-VLC system	PHY layer	Static	CATIA V5 tool and LightTools
Tomaš et al. (2014)	V2V VLC system	PHY layer	Static	JiST/SWANS
Ishihara et al. (2015)	hybrid RF/VLC autonomous platoon	MAC layer	Dynamic	Scenargie®
Ucar et al. (2018a)	hybrid RF/VLC autonomous platoon	PHY and MAC layers	Dynamic	VENETOS
Masini et al. (2017)	full-duplex VVLC Systems	MAC layer	Dynamic	SHINE and VISSIM
Khoder et al. (2020)	VVLC platoon Systems	MAC layer	Dynamic	SUMO and OMNET

3.2 Impact of dynamic traffic on the inter-vehicle spacing

Highways England collects traffic data from a distributed network of bridge-mounted multiple-loop sensors for 60 consecutive minutes over 24 hours period ([Highways England, n.d.](#)). This work utilises traffic measurements collected from the motorways M42 and M6 in the UK (see Figure 3.1). It was collected from 318 sensors in M42 and 154 sensors in M6 on the days 21-24-28 November 2017 and 6-7-8 December 2017, respectively.

The traffic flow and inter-vehicle spacing D variation during 24 hours are shown in

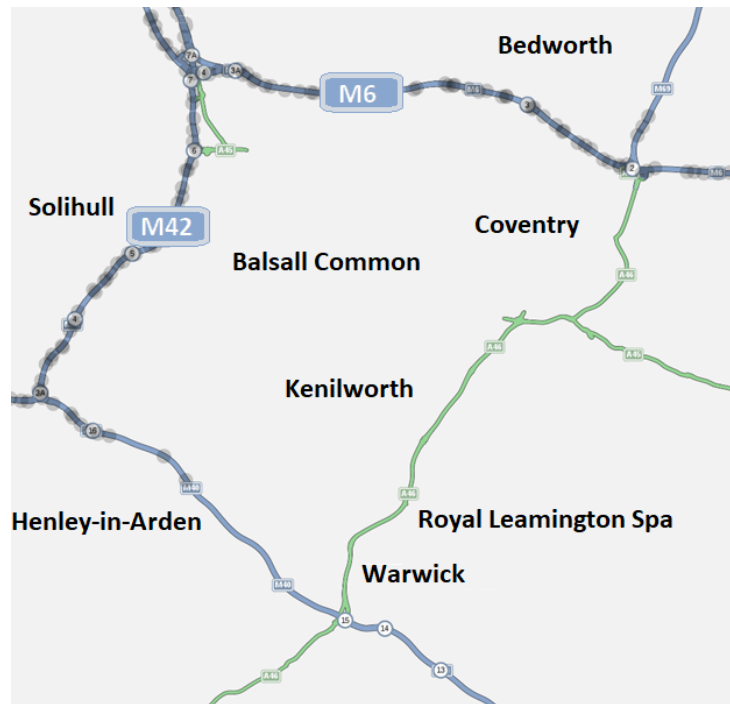


Figure 3.1: Map showing M42 and M6 in the West Midlands, UK (*Highways England, n.d.*).

Figure 3.2. According to the figure, the traffic flow exceeds 1000 veh/h and inter-vehicle spacing D values fall below 20 m between 6:00 and 18:00. The figures also show that the traffic flow is below 500 veh/h and D is above 40 m during the nighttime hours 23:00 to 7:00 in the morning.

The M42 is a smart motorway with controlled variable speed limits and a hard shoulder that runs at peak hours. The M6 was a standard motorway when this set of data was collected. Therefore, this section will first evaluate if there is a statistical difference between measurements from the M42 and M6 motorways.

According to Figure 3.2, sample time windows (16:00-19:00) and (0:00-3:00) are used to study the inter-vehicle spacing variation per lane D_l during the high and low-density traffic, respectively. A **cumulative density function (CDF)** curve-fitting method of traffic measurements was performed to identify the distribution that describes the variation of the inter-vehicle spacing in consistent with the works in (Greenberg, 1966; Wisitpongphan et al.,

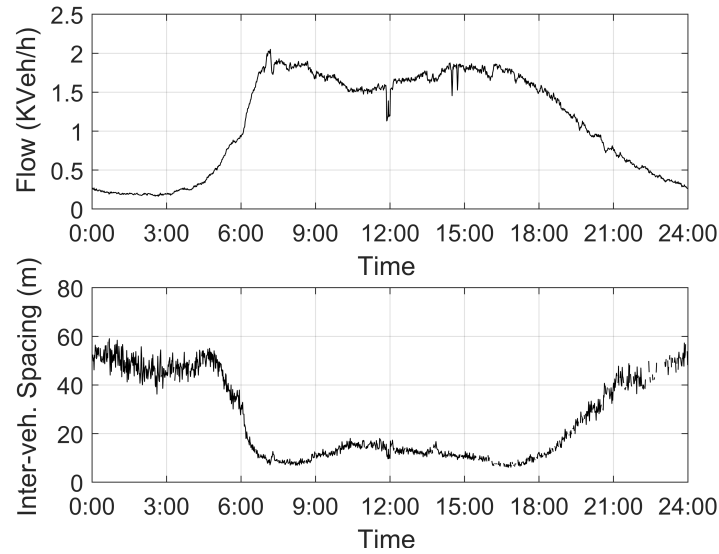
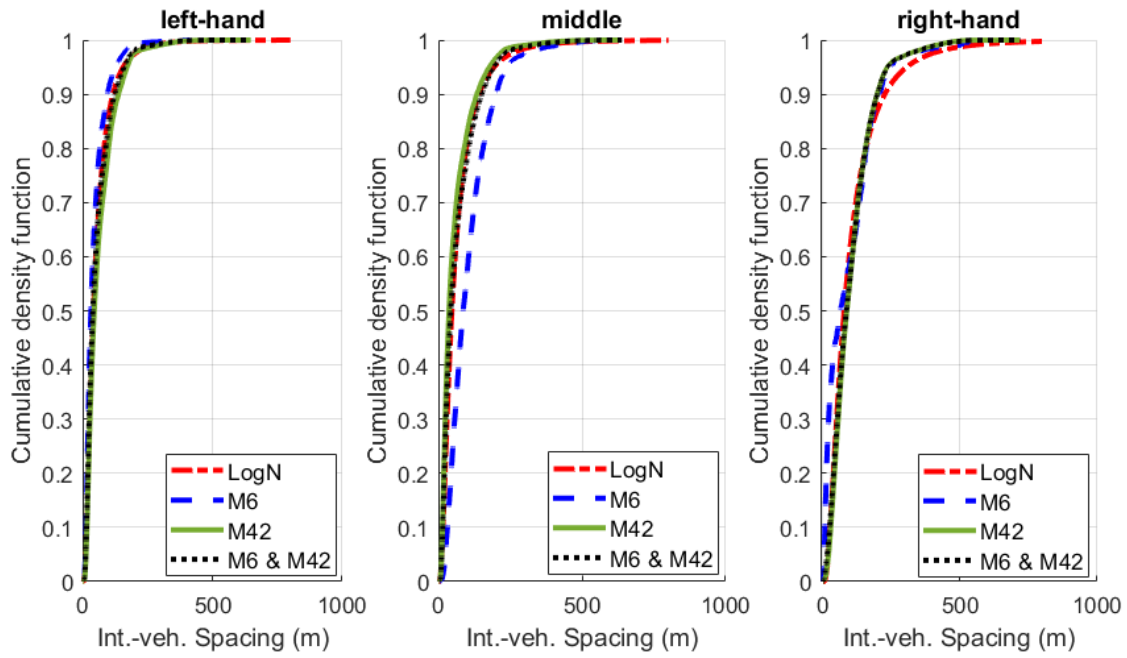


Figure 3.2: Traffic flow variation and inter-vehicle spacing variation during the day.

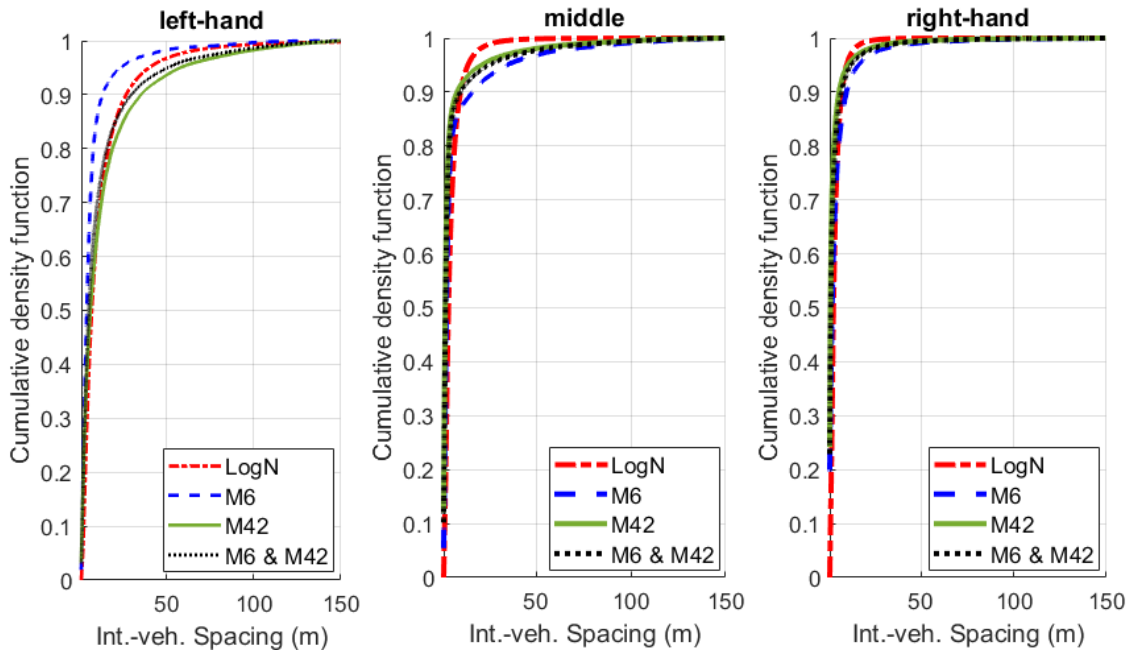
2007; Yan and Olariu, 2011; Roy and Saha, 2018). CDF curves of traffic measurements that describe the variation of the inter-vehicle spacing values in the left-hand, middle and right-hand lanes on the M42, M6 and combined M42 & M6 at sample time windows 00:00-03:00 and 16:00-19:00 are provided in Table 3.2 and illustrated in Figure 3.3. The table and figure show that data from M42, M6 and a combination of data from M42 and M6 follow log-normal distribution with minor variation between the numerical values of the parameters. Therefore, since the data follow the same statistical distribution, averaging the data is required to improve the model generalisation. Note that the justification for the proposed log-normal distribution is given in Section 3.2.1.

3.2.1 inter-vehicle spacing variation per lane

The inter-vehicle spacing changes continuously due to dynamic vehicular traffic density during different periods of the day and with vehicle position in different lanes. The CDF curve-fitting method is used to establish the statistical distribution that best describes the variation of the inter-vehicle spacing. Normal, log-normal, exponential and Nakagami distributions were



(a)



(b)

Figure 3.3: Inter-vehicular distribution provided by traffic measurements in three lanes on the M42, M6 and combined M42 & M6 at a) 00:00-03:00 and b) 16:00-19:00.

Table 3.2: Parameters of log-normal distribution that describes the inter-vehicle spacing per lane on the M42, M6 and combined M42 & M6.

Time	Lane	M42 & M6			M42			M6		
		Mean	μ_d	δ_d	Mean	μ_d	δ_d	Mean	μ_d	δ_d
00:00-03:00	left (1)	57.2	3.72	0.80	64.5	3.5	0.75	45.2	3.8	0.81
	middle (2)	67.1	3.82	0.87	58.0	4.4	0.71	106.8	3.7	0.84
	right (3)	109.8	4.35	0.83	108.7	3.9	1.24	109.5	4.4	0.76
16:00-19:00	left (1)	7.8	1.35	1.18	8.1	1.47	0.89	7.1	1.9	1.19
	middle (2)	3.9	0.81	1.05	3.6	1.14	1.03	4.7	0.83	0.96
	right (3)	2.5	0.50	0.90	2.0	0.93	1.02	3.8	0.58	0.86

considered to identify the distribution that best describes the variation of the inter-vehicle spacing per lane. Table 3.3 provides parameters of the considered distributions. The standard error values of the distribution's parameters that achieve the least estimation errors were used to measure the distributions fit. The table shows that a log-normal distribution provides a close fit to the inter-vehicle spacing because it provides the least standard error values. Therefore, the variation of the inter-vehicle spacing values per lane can be described by a log-normal distribution (Papoulis et al., 2002):

$$P_{D_l}(d_l) = \frac{1}{\delta_d \sqrt{2\pi}} \frac{1}{d_l} \exp\left\{-\frac{(\ln(d_l) - \mu_d)^2}{2\delta_d^2}\right\}. \quad (3.1)$$

The distribution parameters μ_d and δ_d are given in Table 3.3. The CDF curves of the inter-vehicle spacing in the three lanes are shown in Figure 3.4, 3.5 and 3.6 and Figure 3.7, 3.8 and 3.9 during 00:00-03:00 and 16:00-19:00. The figures show the CDF curves of the inter-vehicle spacing fit log-normal distribution closely for the three lanes and during 00:00-03:00 and 16:00-19:00. The inter-vehicle spacing distribution in different lanes is used in Chapter 6 to investigate the BER performance of the V2V-VLC system considering the existence of other vehicles in the adjacent lanes. To study the V2V-VLC channel, variation of inter-vehicle spacing per motorway is considered. Therefore, analysis and discussion of inter-vehicle spacing variation per motorway are provided in the following section.

Table 3.3: Parameters of log-normal distribution that describes the inter-vehicle spacing per lane.

Time	Lane	Distribution	Mean Value (m)	μ_d	μ_d estimation error (%)	δ_d	δ_d estimation error(%)
00:00-03:00	left (1)	log-normal	57.2	3.72	0.45	0.80	0.32
	middle (2)		67.1	3.82	0.44	0.87	0.31
	right (3)		109.8	4.35	0.64	0.83	0.45
	left (1)	Nakagami	62.1	0.5	0.33	6032	4844
	middle (2)		73.3	0.45	0.26	8770	6630
	right (3)		107.9	0.59	0.54	17131	1723
	left (1)	Normal	57.2	57.2	29.8	52.3	21.0
	middle (2)		67.1	67.1	33.2	65.3	23.4
	right (3)		104.0	104.0	78.9	61.2	43.3
	left (1)	Exponential	57.5	57.5	32.7	-	-
	middle (2)		67.1	67.1	34.1	-	-
	right (3)		104.0	104.0	81.0	-	-
16:00-19:00	left (1)	log-normal	7.8	1.35	0.45	1.18	0.31
	middle (2)		3.9	0.81	0.42	1.05	0.29
	right (3)		2.5	0.50	0.27	0.90	0.39
	left (1)	Nakagami	11.9	0.2	0.10	325	256
	middle (2)		8.3	0.2	0.09	169	148
	right (3)		5.2	0.2	0.11	63.3	57.7
	left (1)	Normal	8.6	8.6	6.0	15.8	4.2
	middle (2)		5.1	5.1	4.8	11.9	3.4
	right (3)		3.1	3.1	6.0	7.3	2.2
	left (1)	Exponential	8.6	8.6	3.27	-	-
	middle (2)		5.1	5.1	2.0	-	-
	right (3)		3.1	3.1	1.3	-	-

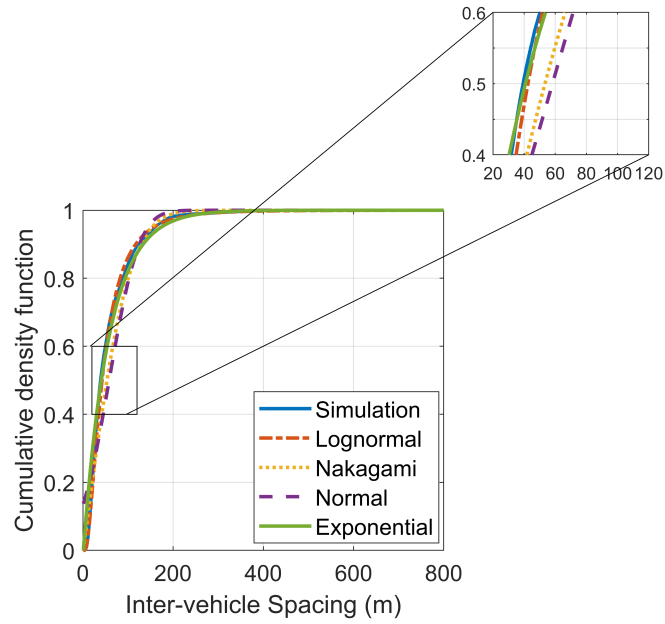


Figure 3.4: The cumulative density function of inter-vehicle spacing in the left-hand lane at 00:00-03:00.

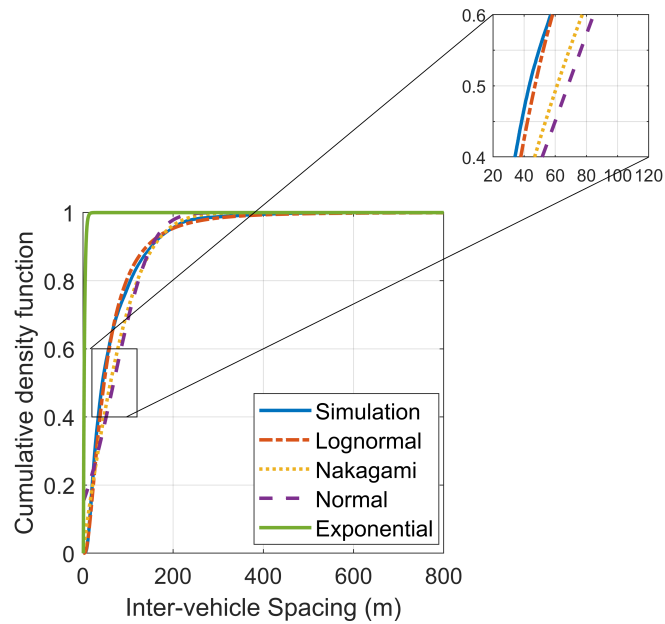


Figure 3.5: The cumulative density function of inter-vehicle spacing in the middle lane at 00:00-03:00.

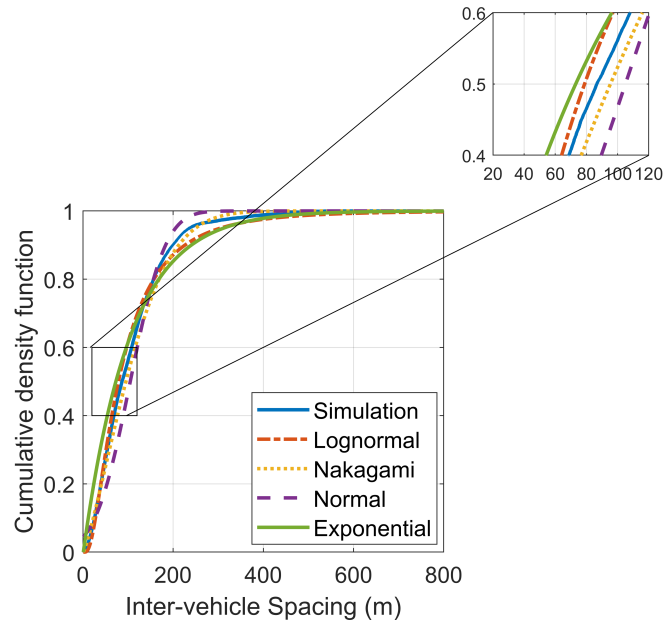


Figure 3.6: The cumulative density function of inter-vehicle spacing in the right-hand lane at 00:00-03:00.

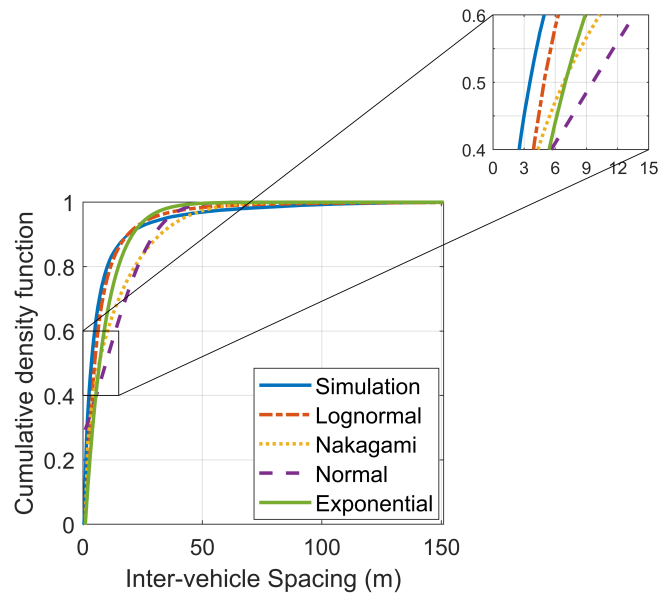


Figure 3.7: The cumulative density function of inter-vehicle spacing in the left-hand lane at 16:00-19:00.

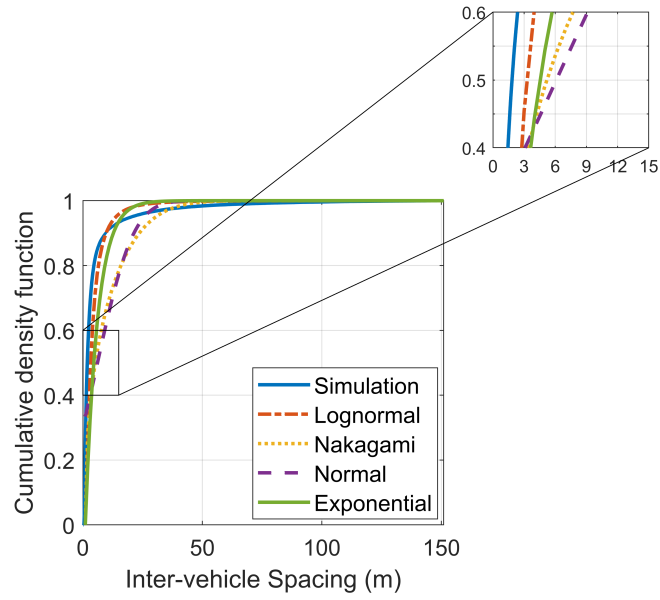


Figure 3.8: *The cumulative density function of inter-vehicle spacing in the middle lane at 16:00-19:00.*

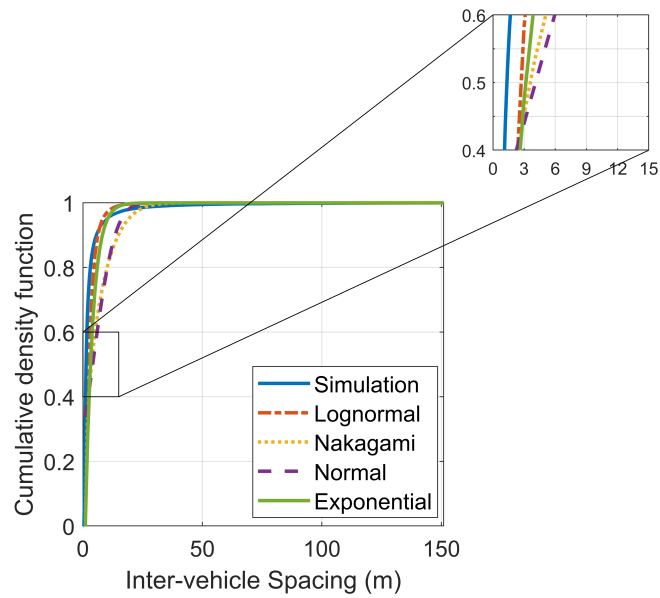


Figure 3.9: *The cumulative density function of inter-vehicle spacing in the right-hand lane at 16:00-19:00.*

3.2.2 inter-vehicle spacing variation per motorway

According to Figure 3.2, it is observed that between 6:00 and 20:00, the traffic flow exceeds 1000 *veh/h* and D values are below 20 m. However, between 23:00 to 7:00, the traffic flow is below 500 *veh/h* and D exceeds 40 m. However, when the data was collected, in November 2017, the sun rose between 07:00 and 07:52 and set between 16:30 and 16:00 (TimeandDate, 2017). In December 2017, the sun rose between 07:53 and 08:16 and set around 16:00 (TimeandDate, 2017). Therefore, over the two months considered, the sun influences the evening traffic peak. Hence, time periods for two traffic conditions are considered in this work. The first window between 12:00 and 15:00 is characterised by heavy traffic during the early afternoon, just before the evening peak traffic and before the sunsets. The second window between 00:00 and 03:00 corresponds to very low traffic observed at night, well before the sun rises after 07:00.

Different distributions were considered including, log-normal, Normal, exponential and Nakagami distributions to establish the statistical distribution that best describes the variation of the inter-vehicle spacing. The standard error values of the distributions' parameters were used to measure the accuracy of curve-fitting. Parameters of different distributions that are expected to describe the inter-vehicle spacing at the sample time windows 00:00-03:00 and 12:00-15:00 are given in Table 3.4. The table shows that among the examined distributions, the log-normal fits the inter-vehicle spacing D closely and it is given by (Papoulis et al., 2002):

$$P_D(d) = \frac{1}{\sigma_s \sqrt{2\pi}} \frac{1}{d} \exp\left(-\frac{(\ln(d) - \mu_s)^2}{2\sigma_s^2}\right), \quad (3.2)$$

where the parameters μ_s and σ_s of the distribution are given in Table 3.4. The log-normal distribution provides a realistic description of the inter-vehicle spacing because it takes the safe spacing between following vehicles and the speed limits of the road into account (Greenberg, 1966; Yan and Olariu, 2011; Roy and Saha, 2018).

The log-normal distributions of the inter-vehicle spacing D during the sample time windows 00:00-03:00 and 12:00-15:00 are shown in Figure 3.10.

Wisitpongphan et al. (2007) used a real-world traffic measurement on the I-80 freeway in

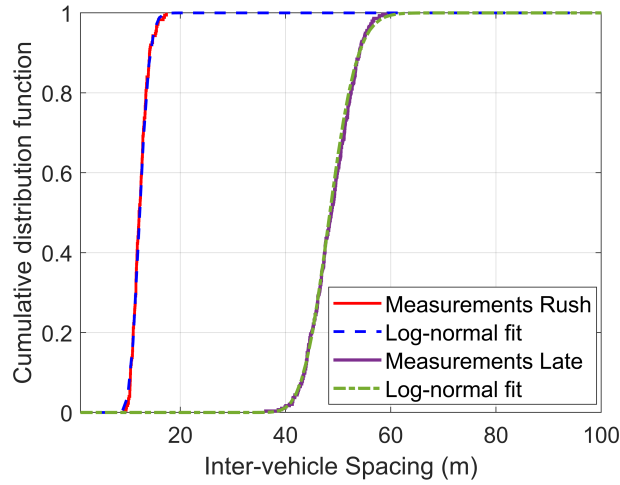


Figure 3.10: The cumulative density function of reflection at late 00:00-03:00 and rush 12:00-15:00 hours.

Table 3.4: Parameters of different distributions that expected to describe the inter-vehicle spacing per motorway.

Time	Distribution	Mean Value (m)	μ_s	μ_s estimation error (%)	δ_s	δ_s estimation error(%)
00:00-03:00	log-normal	48.72	3.88	0.71	0.09	0.50
	Nakagami	48.82	29.0	307.3	2404	3351
	Normal	48.82	48.82	34.0	4.54	24.0
	Exponential	48.80	48.80	366.9	-	-
12:00-15:00	log-normal	12.37	2.51	0.87	0.12	0.61
	Nakagami	12.45	18.2	190.5	157.1	275.2
	Normal	12.44	12.44	11.1	1.48	7.9
	Exponential	12.44	12.44	93.0	-	-

California to find the statistical distribution of the inter-vehicle spacing D . [Wisitpongphan et al. \(2007\)](#) showed that at day time hours when the traffic flow is larger than 1000 veh/h , the inter-vehicle spacing D follows a log-normal distribution. However, at late night hours between 01:00 and 03:00, the traffic flow is less than 1000 veh/h and the inter-vehicle spacing

D can be approximated by an exponential distribution with mean $\lambda_s=0.0039$ (Papoulis et al., 2002);

$$f_D(d) = \lambda_s e^{-\lambda_s d}. \quad (3.3)$$

As discussed in chapter 2, the path loss of V2V-VLC is a function of the inter-vehicle spacing. Therefore, having estimated the statistical distributions that describe the inter-vehicle spacing variation during different times of the day, the following section establishes the statistical distribution of V2V-VLC channel path loss for a stable queue driving scenario.

3.3 Impact of dynamic traffic on the channel path loss

The dynamic nature of traffic varies the inter-vehicle spacing D and the lateral angular deviation between vehicles ϕ . To study the impact of the inter-vehicle spacing variation D only on the path loss in (2.16), a queue movement pattern of vehicular platoon is assumed Ucar et al. (2018b); Zhang et al. (2019). Based on this assumption, the vehicles move in a straight line with a negligible lateral angular deviation between vehicles ($\phi = 0$). Therefore, the path loss (in dB) in (2.16) can be given by:

$$P_L = 10 \log(A_r) - 10 \log(2\pi) - 20 \log(D), \quad (3.4)$$

where the terms $(A_r) - 10 \log(2\pi)$ are constants and the inter-vehicle spacing D is a log-normally distributed random variable given in (3.2). Therefore, the last term of the path loss is given by the logarithmic transformation of the inter-vehicle spacing distribution $\log(D)$, and hence, it can be described by a normal distribution (Papoulis et al., 2002):

$$P_{\log(D)}(x; \mu_g, \sigma_g) = \frac{1}{\sigma_g \sqrt{2\pi}} \exp\left(-\frac{(x - \mu_g)^2}{2\sigma_g^2}\right), \quad (3.5)$$

where $\sigma_g = 20\sigma_s \ln(10)$ and $\mu_g = 20\frac{\mu_s}{\ln(10)}$. According to the linear transformation principles, the path loss in (3.4) is given by a normal distribution with a standard deviation $\sigma_m = \sigma_g$ and mean value $\mu_m = 10\frac{A_r}{2\pi} - \mu_g$, as follows (Papoulis et al., 2002)

$$P_L(x; \mu_m, \sigma_m) = \frac{1}{\sigma_m \sqrt{2\pi}} \exp\left(-\frac{(x - \mu_m)^2}{2\sigma_m^2}\right). \quad (3.6)$$

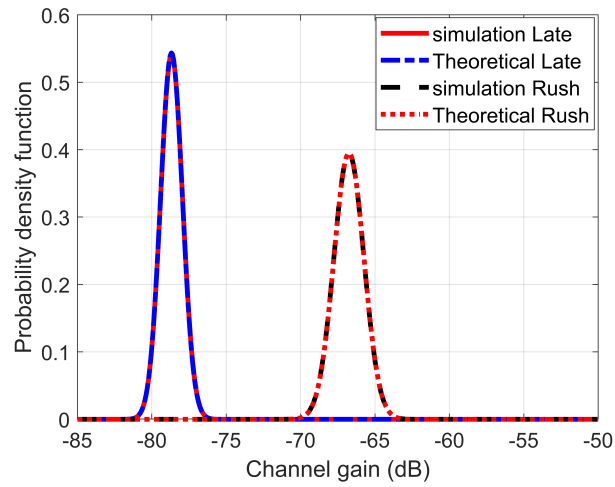
Table 3.5: Summary of mean and variance values of the statistical path loss when the inter-vehicle spacing D has a log-normal distribution for time intervals 00:00-03:00 and 12:00-15:00.

Time	Distribution of D	mean D (m)	mean value (dB)	standard deviation
0:00-3:00	log-normal	48.72	-78.7	0.73
	exponential	256.41	-88.2	8.68
12:00-15:00	log-normal	12.37	-66.8	1.01

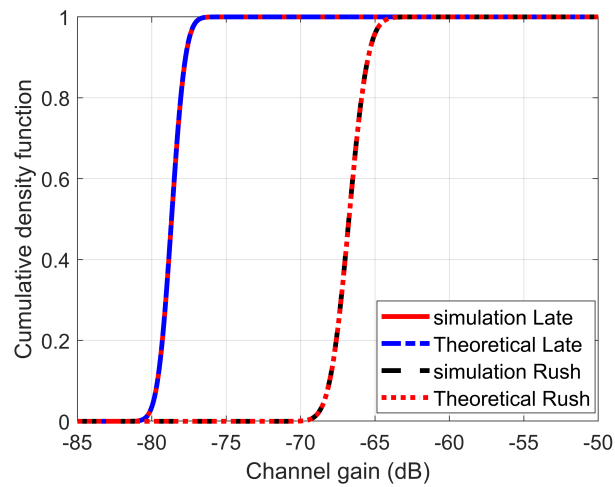
MC simulation of 10^6 iterations are used to examine similarity between the simulated path loss in (3.4) and the equivalent statistical distribution of the path loss in (3.6). The simulation assumes a receiver with an active area A_r of 1 cm^2 and receiver FOV of 80° . The Kolmogorov-Smirnov test was employed to measure the similarities between simulation and theoretical distributions. The null hypothesis states that a sample from simulation data and a sample from the theoretical distribution come from a population with the same distribution. Figure 3.11 shows the PDF and CDF curves of the LOS component of V2V-VLC path loss to illustrate the similarity between the simulated path loss in (3.4) and the equivalent statistical distribution in (3.6), when the inter-vehicle spacing D has a log-normal distribution with parameters given in Table 3.4, at late 00:00-03:00 and rush 12:00-15:00 hours. The figure shows that the path loss distribution obtained using MC simulation matches with the theoretical distribution in (3.6). The mean and standard deviation values are summarised in Table 3.5. The table and figures show that the standard deviation and the mean of path loss values match the statistical values σ_m and μ_m for both periods of the day. The Kolmogorov-Smirnov test does not reject the null hypothesis at the 1% significance level, validating the theoretical analysis prove the accuracy of predicted mean and standard deviation values.

Figure 3.11 also shows that the path loss values at 12:00-15:00 are less than its values at 00:00-03:00. This is expected as Table 3.4 shows that the mean inter-vehicle spacing values at 12:00-15:00 are less than its values at 00:00-03:00 due to the high vehicular density.

According to Wisitpongphan et al. (2007), the exponential distribution is considered to



(a)



(b)

Figure 3.11: The a) PDF and b) CDF curves of the *LOS* component of V2V-VLC the simulated path loss in (3.4) and the equivalent statistical distribution (theoretical) in (3.6), when the inter-vehicle spacing D has a log-normal distribution with parameters given in Table 3.4, at 00:00-03:00 (late hours) and 12:00-15:00 (rush hours).

describe the inter-vehicle spacing D at late hours from 00:00 to 03:00 when the traffic density is very low and the mean inter-vehicle spacing is larger than 250 m. Therefore, the logarithmic transformation of the exponential distribution describes the last term of path loss in (3.4), $\log(D)$. According to [Abdelkader and Al-Marzouq \(2010\)](#), if a random variable X has an exponential distribution, then $\lambda_s - \beta_s \log X/\lambda_s$ has **generalized extreme value distribution (GEV)** type I (Gumbel distribution). Therefore, to make the path loss in (3.4) of the form $\lambda_s - \beta_s \log X/\lambda_s$, the terms $+20 \log \lambda_s - 20 \log \lambda_s + \lambda_s - \lambda_s$ are added to the (3.4), as follows

$$P_L = 10 \log(A_r) - 10 \log(2\pi) - 20 \log \lambda_s + 20 \log \lambda_s - \lambda_s + \lambda_s - 20 \log D, \quad (3.7)$$

then, by rearranging (3.7), the path loss can be written as

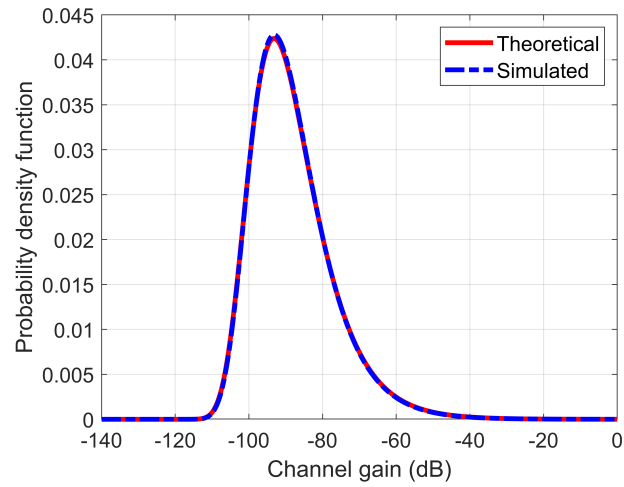
$$P_L = 10 \log(A_r) - 10 \log(2\pi) - 20 \log \lambda_s - \lambda_s + \lambda_s - 20 \log \frac{D}{\lambda_s}. \quad (3.8)$$

The last two terms represent a **GEV** distribution and the other terms are constants which shift in the mean value of the **GEV** distribution. Therefore, the probability distribution function of the path loss (in dB) is given by ([Papoulis et al., 2002](#)):

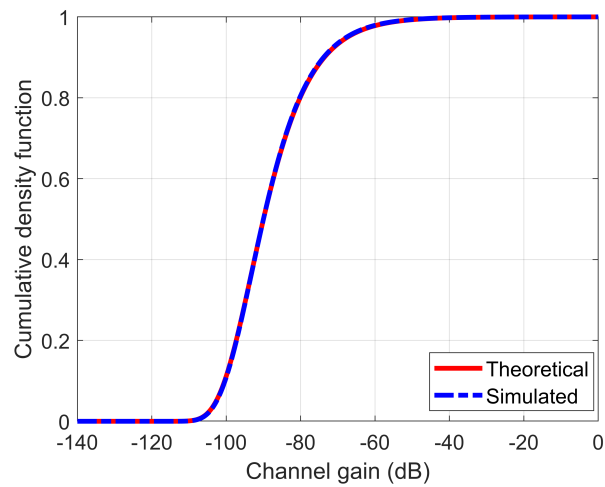
$$P_L(x; \mu_n, \sigma_n) = -\frac{1}{\sigma_n} \exp \left(-\exp \left(-\frac{x - \mu_n}{\sigma_n} \right) - \frac{x - \mu_n}{\sigma_n} \right), \quad (3.9)$$

where the standard deviation is $\sigma_n = 20/\ln 10$ and the mean $\mu_n = -10 \log(A_r/2\pi) + 20 \log \lambda_s - \lambda_s$.

Figure 3.12 shows the **PDF** and **CDF** of the path loss, when the inter-vehicle spacing D has an exponential distribution with $\lambda_s = 0.0039 \text{ veh.m}^{-1}$ ([Wisitpongphan et al., 2007](#)). The figure illustrates that the simulated path loss matches the theoretical prediction (3.9) with distribution parameters σ_n and μ_n values that match the statistical values. The Kolmogorov-Smirnov test does not reject the null hypothesis at the 1% significance level. The mean and standard deviation values are summarised in Table 3.5. The table shows that the mean of path loss value when the inter-vehicle spacing D has an exponential distribution is larger than mean path loss values when it has log-normal because the mean the inter-vehicle spacing is larger.



(a)



(b)

Figure 3.12: The a) PDF and b) CDF of the LOS component of V2V-VLC path loss when the inter-vehicle spacing D has an exponential distribution with $\lambda_s = 0.0039 \text{ veh.m}^{-1}$.

3.4 Summary

The impact of the inter-vehicular variation was exclusively studied, assuming a stable queue movement pattern of vehicles. Relying on traffic measurements collected from the M6 and

M42 motorways, distributions that describe inter-vehicle spacing and associated channel path loss variation were established. The analysis showed that a log-normal distribution provides the best fit to describe inter-vehicle spacing variation at different times of the day, and consequently the path loss has a normal distribution. However, when the exponential distribution is considered to describe the inter-vehicle spacing at late night hours, then the channel path loss is given by generalised extreme value distribution.

In conclusion, dynamic traffic affects the channel path loss of **V2V-VLC** systems because it changes the geometry of the link. Therefore, the impact of vehicles' headlight radiation pattern due to the angular deviation between vehicles and variation of inter-vehicle spacing on the **LOS** component of the **V2V-VLC** channel is investigated next in Chapter 4.

Chapter 4

Line-of-Sight Vehicle-to-Vehicle Visible Light Communications Channel

The **V2V-VLC** channel model depends on the geometry of the communication link presented by the inter-vehicle spacing and angle deviation between vehicles. The geometry of the **V2V-VLC** link changes dynamically and continuously due to the movement of vehicles. As explained in Section 2.2.2, **V2V-VLC CIR** combines the **LOS** and **NLOS** propagation paths. This chapter examines the impact of the dynamic movement of the vehicles on the **LOS** component of the **V2V-VLC** channel. A statistical channel model to describe the path loss of **V2V-VLC**, considering the dynamic traffic conditions and the radiation pattern of vehicles' sources, is established. For this purpose, four radiation pattern models (Lambertian, Gaussian, piecewise Lambertian and empirical) are utilised to describe the radiation angular distribution of vehicles' sources. Furthermore, this chapter considers the impact of weather conditions on the **LOS V2V-VLC** channel.

The chapter is organised as follows: the related works are discussed in Section 4.1. Examination of the radiation pattern of vehicles sources to quantify the effect of the radiation pattern on the **V2V-VLC** channel model is given in Section 4.2. The impact of weather conditions on the **LOS V2V-VLC** channel accounting for the radiation pattern of vehicles' sources is investigated in Section 4.3. Chapter summary is given in Section 4.4.

4.1 Related works

International and local standards regulate the design of vehicular light sources to prevent or minimise the risk to road users. In the UK, the Road Vehicles Lighting Regulations 1989 standardised the illumination pattern of vehicles headlights to illuminate the road without causing dazzle to road users, pedestrians and oncoming drivers ([The Road Vehicles Lighting Regulations, 1989](#)). The United Nation [Economic Commotion for Europe Regulation No. 112 \(ECE R112\)](#) also standardised the illumination pattern of vehicular light sources internationally to prevent the temporal blindness of drivers and pedestrians ([Chen et al., 2010](#); [Uni, 2013](#)). The regulations mandated the asymmetrical radiation pattern that directed the light intensity toward the road surface and away from the oncoming traffic lanes ([Cheng et al., 2018](#)). The asymmetric illumination pattern is a design requirement for the low-beam lamps that are used for short-range. Therefore, the vehicles manufacturers adopted different designs and optical elements to shape the illumination pattern of vehicular light sources to satisfy the regulations.

[Lee et al. \(2012b\)](#) considered the radiation pattern of the Audi R8 low-beam headlamp and streetlamp to study the delay profiles and channel impulse response of [V2V](#) and [V2I](#) channels. The Audi R8 headlight design is shown in [Figure 4.1 \(a\)](#). The study utilised ray-tracking software to simulate the illumination patterns of the light sources. However, the results did not provide an expression to describe the channel which can be used in the communication link design. In addition, the studies did not consider dynamic street scenarios where the traffic density varies during different periods of the day.

[Viriyasitavat et al. \(2013\)](#) carried out empirical measurements using off-the-shelf Yamaha Cygnus-X scooter taillight to derive a piecewise Lambertian expression of the [VVLC](#) channel. The design of the Yamaha Cygnus-X scooter taillight is illustrated in [Figure 4.1 \(b\)](#). [Viriyasitavat et al.](#) relied on a linear least-square method to estimate the parameters of the channel model expression. However, the radiation pattern of a scooter taillight is different from other types of vehicular light sources such as low-beam and high-beam headlights ([Cheng et al., 2018](#)).

The illumination patterns of tungsten-halogen high and low-beam lamps were considered by [Luo, Ghassemlooy, Minh, Bentley, Burton and Tang \(2015\)](#) to study the road-surface reflection and performance of VVLC systems. The study showed that the high-beam lamp has a symmetrical illumination pattern with a narrow and flat horizontal beam tilted at a few degrees to the left, while the low-beam lamp has an asymmetrical pattern. However, the used tungsten-halogen headlights differ from the LED headlights that can support high-speed vehicular communication.

[Cui et al. \(2014\)](#) employed the 2015 Toyota Corolla Altis pair of taillights to measure the path loss, autocorrelation function and coherence time of the VVLC channel. The study assumed a single LED source radiation pattern. Hence, the Lambertian model was used to describe the radiation pattern of the taillights. The Toyota Corolla Altis taillight design is depicted in Figure 4.1 (c). Likewise, [Hua-Yen Tseng et al. \(2015\)](#) studied the illumination pattern of the 2015 Toyota Corolla Altis left low-beam lamp of the headlight, left positioning and brake lamps of the taillight to investigate the link asymmetry due to the received power difference over the incoming and outgoing links. The results revealed that the headlight has an irregular pattern with a long operating range of 100 m, compared to the taillight, which has a limited range of up to 30 m. In addition, the study provided an interesting comparison between the illuminance of halogen-based lamps and LED-based lamps. The results showed that the illuminance of halogen-based and LED-based lamps match the transmission range up to 15 m in headlights and match for a full-transmission range in taillights.

[Chen et al. \(2016\)](#) considered the illumination pattern of the low-beam lamp of the 2015 Toyota Corolla Altis left headlight to study the impacts of vehicle mobility traces and behaviours on the VVLC channel time variation and correlation characteristics. The study considered the worst-case scenario of illumination pattern irregularity and hence a faster channel time variation. Although the provided measurement results were vital to characterise the VVLC channel, the study did not consider the change in traffic density during different periods of the day. The 2015 Toyota Corolla Altis headlight design is given in Figure 4.1 (d).

[Memedi et al. \(2017\)](#) utilised the illumination pattern obtained by [Hua-Yen Tseng et al. \(2015\)](#) for the 2015 Toyota Corolla Altis left low-beam headlight to derive an analytical

expression of **VVLC** channel path loss. The expression consists of two parts: propagation and geometrical path loss. [Karbalyghareh et al. \(2020\)](#) used this as a benchmark to compare the proposed and simulated **VVLC** channel models. The simulated model used a non-sequential ray-tracing software tool to study the radiation pattern of the low-beam headlight, which uses a Philips Luxeon Rebel white **LED** source. Although [Karbalyghareh et al.](#)'s model considered the geometrical path loss, the comparison did not consider the geometrical path loss part of [Memedi et al.](#)'s model.

[Memedi et al. \(2018\)](#) extended the investigation by conducting an experimental study of the optical radiation pattern for different vehicular light sources, high and low-beams of two Sedans and a SUV. The measurements were carried out in an environment that simulates a realistic outdoor channel model accounting for the ambient noise and the nature of surface materials. The results confirmed that low-beams have relatively shorter luminous ranges and asymmetrical radiation pattern tilted away from the oncoming traffic. The high-beams have longer illumination ranges and radiation patterns that can be considered symmetrical. The comparison between different high-beam lamps designs for the same vehicle type showed a non-negligible difference between the radiation patterns of these lamps.

[Shen and Tsai \(2017\)](#) carried out an experimental study to investigate the feasibility of the **VVLC** system. The study utilised a taillight of the 2015 Ford Focus C346 1.6L. The radiation pattern of taillight was considered to be symmetrical. Hence, the Lambertian model was used to describe the channel. Similarly, [Béchadergue et al. \(2019\)](#) utilised the taillight of three different vehicles, 2015 Ford Focus, Toyota Corolla, and Mitsubishi Outlander. The study considered that the Lambertian model is applicable to describe the channel when the angular deviation between vehicles is within 10° .

[Elamassie et al. \(2018\)](#) considered the radiation pattern of a high-beam lamp (Philips Luxeon Rebel **LED**) to find path loss, **BER** and maximum achievable distance under the effect of rain and fog. The proposed path loss expression considered the propagation distance but did not consider the geometrical impact of the asymmetrical radiation pattern of the light source. Similarly, [Abuella et al. \(2019\)](#) utilised Philips Luxeon Rebel **LED**-based vehicle's headlights to implement the **VLiDAR** which estimates vehicles' speed. A simulation-based model of the

low-beam lamp was considered to model the channel. The results revealed that the path loss obtained by the Lambertian model is higher than the path loss of the simulation-based model.

Eldeeb, Eso, Uysal, Ghassemlooy, Zvanovec and Sathian (2020) considered the illumination pattern of Audi A5 S5 near side (left-hand side) LED outer taillight to study VVLC channel path loss at a fixed transmission range. The design of the Audi A5 S5 taillight is illustrated in Figure 4.1 (e). The study used the Lambertian model as a benchmark. The results showed 8° difference in the half-power angle of the illumination pattern between the two sides of the beam.

A measurement-based illumination pattern of the 2017 Ford Mondeo multibeam headlight was considered by Uyrus et al. (2019) to study the V2V-VLC channel. The Ford Mondeo multibeam headlight design is illustrated in Figure 4.1 (f). The study accounted for the existence of other vehicles in single and multiple lanes scenarios and LOS blockage scenario. The measurements were carried out in an indoor parking garage for a transmission distance limited to 25 m, which does not reflect realistic dynamic traffic, ambient noise and weather conditions of the outdoor VVLC channel.

Despite the mandatory asymmetrical design of the illumination pattern of vehicles headlights, the Lambertian model was used to describe the symmetrical radiation pattern of LED-based headlight and taillight in (Al-Kinani, Sun, Wang, Zhang, Ge and Haas, 2018; Abualhoul et al., 2018; Béchadergue et al., 2019; Esmail et al., 2017; Chen and Wang, 2020).

Cheng et al. (2018) emphasized the importance of studying the illumination pattern of vehicles light sources to model the VVLC channel accurately. However, due to the variety and complexity of vehicles' light sources designs, finding a universal model that can describe the radiation pattern of different sources is difficult.

Moreno and Sun (2008); Ding et al. (2016) proposed a series of Gaussian functions to model the radiation intensity distribution of asymmetrical radiation patterns of different LEDs. The proposed model showed high accuracy in describing the radiation intensity distribution of asymmetrical radiation patterns for LEDs from various manufacturers.

In conclusion, different vehicle source designs are available from various manufacturers. Therefore, the radiation pattern of vehicles' sources varies with the source design. This



Figure 4.1: Examples of vehicular light sources design from different manufacturers including a) 2010 Audi R8 headlight ([Lee et al., 2012b](#)), b) Yamaha Cygnus-X scooter taillight ([Viriyasitavat et al., 2013](#)), c) 2015 Toyota Corolla Altis taillight ([Toyota, 2018](#)), d) 2015 Toyota Corolla Altis headlight ([Toyota, 2018](#)), e) 2017 Ford Mondeo multibeams headlight ([Ford, 2020](#)) and f) Audi A5 S5 taillight ([Audi, 2021](#)).

Table 4.1: *Examples of vehicular light sources that were considered in the literature.*

Ref.	Source	Lamp
Lee et al. (2012a)	Audi R8	low-beam
Viriyasitavat et al. (2013)	Yamaha Cygnus-X scooter	taillight
Cui et al. (2014)	2015 Toyota Corolla Altis	pair of taillights
Hua-Yen Tseng et al. (2015)	2015 Toyota Corolla Altis	low and taillight
Chen et al. (2016)	2015 Toyota Corolla Altis	left low-beam
Luo et al. (2015)	Tungsten-halogen	high and low-beams
Shen and Tsai (2017)	2015 Ford Focus C346 1.6L	taillight
Memedi et al. (2018)	Two Sedans and an SUV	high and low-beams
Elamassie et al. (2018) Karbalyghareh et al. (2020)	Philips Luxeon Rebel LED	high-beams
Abuella et al. (2019)	Philips Luxeon Rebel LED	low-beam
Uyrus et al. (2019)	2017 Ford Mondeo	multibeam
Béchadergue et al. (2019)	2015 Ford Focus Toyota Corolla Mitsubishi Outlander	taillight
Eldeeb et al. (2020)	Audi A5 S5	left low-beam

increases the complexity of studying the **V2V-VLC** channel. The majority of the previous studies have considered a specific source design to model the radiation pattern and **VVLC** channels. Therefore, four different models are examined in the following section to quantify the impact of radiation pattern variation on modelling the **V2V-VLC** channel.

4.2 Impact of the radiation pattern on LOS V2V-VLC channel

The radiation pattern of the vehicle's sources varies according to the manufacturer and design parameters such as the number and alignment of LEDs, types of optics and shapes of reflectors (Cheng et al., 2018). Therefore, as given in (2.16), the radiation intensity distribution $I(\phi)$ should be considered to study the V2V-VLC channel.

Four models are examined in this study to investigate the impact of the luminous intensity distribution on the V2V-VLC channel: a) the conventional Lambertian model that describes the symmetrical radiation intensity patterns, b) a piecewise Lambertian model established by Viriyasitavat et al. (2013) to describe the asymmetrical radiation intensity pattern of Yamaha Cygnus-X scooter taillight, c) a series of Gaussian functions which describes the asymmetrical radiation intensity patterns, and d) an empirical model proposed by Memedi et al. (2017) to describe the path loss of a 2015 Toyota Altis low-beam headlight.

4.2.1 The Lambertian model

The asymmetry condition is mandatory for the low-beam lamp to mitigate drivers' temporary blindness caused by direct lights from preceding or oncoming vehicles on the opposite side of travel. The low-beam lamp is utilised at high-density traffic when the inter-vehicle spacing is short. Therefore, its radiation pattern is designed to be asymmetrical, directed towards the road surface and with a shorter luminous range (Chen et al., 2010; Uni, 2013; Cheng et al., 2018). However, the regulations do not restrict the high-beam lamp radiation pattern. Therefore, the radiation of the high-beams has a less asymmetrical pattern (Luo, Ghassemlooy, Minh, Bentley, Burton and Tang, 2015; Memedi et al., 2018). Furthermore, Béchadergue et al. (2019) showed that vehicle taillight has a symmetrical radiation pattern. Hence, it can be described by the Lambertian model.

The Lambertian angular distribution of the radiation intensity pattern model is given by

(Ghassemlooy et al., 2019):

$$I(\phi) = \frac{(m+1)}{2\pi} \cos^m(\phi), \quad (4.1)$$

where $m = \frac{-0.6931}{\ln(\cos(\Psi_{1/2}))}$ is the Lambertian order and $\Psi_{1/2}$ is the half-power angle of the radiation. The path loss in (2.16) can be simplified to:

$$P_L = 10 \log(A_r(m+1)) - 10 \log(2\pi) - 20 \log D + 10(m+1) \log \cos(\phi). \quad (4.2)$$

Therefore, the distribution of the path loss P_L depends on the sum of the inter-vehicle spacing D and the angle deviation ϕ distributions. If the inter-vehicle spacing D has a log-normal distribution as given in (3.2), then the term $10 \log(A_r(m+1)) - 20 \log D$ is a linear transform of the normal distribution as given in (3.6) with a standard deviation $\sigma_b = 20\sigma_s \ln(10)$ and mean value $\mu_b = 10 \frac{A_r(m+1)}{2\pi} - \mu_s$.

The angle ϕ represents the lateral offset between the following vehicles that is continuously varying due to vehicles' relative motion. Many variables influence the variation of the lateral offset, such as lane width, traffic density, driving speed, vehicles types and manoeuvring (Pal and Mallikarjuna, 2010; Kim et al., 2015). Hence, various distributions have been used to describe the lateral offset as a function of a specific variable (Pal and Chunchu, 2019; Pal and Mallikarjuna, 2010; Wang et al., 2014). Other variables are averaged out to examine the radiation pattern of vehicles' sources as a function of ϕ only. Therefore, the lateral offset between the following vehicles and hence the angle ϕ is assumed uniformly distributed $\phi \sim U(0, \phi_o)$ (Kim et al., 2015).

The statistical distribution of the last term in (4.2), $10(m+1) \log \cos(\phi)$, is a logarithmic transform of $\cos(\phi)$. The cosine distribution of uniformly distributed angle ϕ is given by (Papoulis et al., 2002, P. 99):

$$f_{Z_\phi}(z_\phi) = \frac{1}{\phi_o \sqrt{1 - z_\phi^2}} \quad \cos(\phi_o) < z_\phi < 1. \quad (4.3)$$

Consequently, the term $10(m+1) \log \cos(\phi)$ is given by (Papoulis et al., 2002, P. 97):

$$f_Y(y) = \frac{1}{g\phi_o \sqrt{e^{-2y/g} - 1}} \quad 0 < y < 10(m+1) \log \cos(\phi_o), \quad (4.4)$$

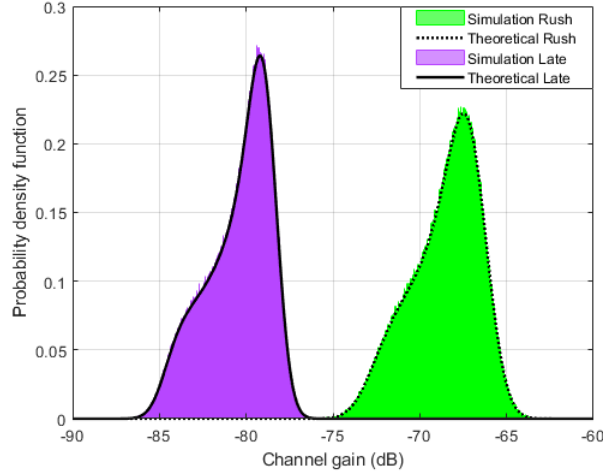


Figure 4.2: The probability density function of channel path loss obtained by the Lambertian at 00:00-03:00 (late hours) and 12:00-15:00 (rush hours).

where $g = 10(m + 1) \log e$ and e is the Napierian number.

The statistical distribution of the sum of two random variables is given by the convolution between the distributions of these variables (Papoulis et al., 2002). Therefore, the statistical distribution of path loss in (4.2) is given by the convolution between the normal distribution of the inter-vehicle spacing D in (3.6) and the log-cosine distribution in (4.4) (Papoulis et al., 2002, P. 136):

$$P_L(x; \mu_b, \sigma_b) = \frac{1}{g\phi_o\sigma_b\sqrt{2\pi}} \int_{\alpha_m}^0 \frac{\exp\left(-\frac{(x-y-\mu_b)^2}{\sigma_b^2}\right)}{\sqrt{e^{-2y/g} - 1}} dy, \quad (4.5)$$

where $\alpha_m = 10(m + 1) \log(\cos(\phi_o))$.

Figure 4.2 shows the PDFs of channel path loss obtained by the Lambertian model at 00:00-03:00 (late hours) and 12:00-15:00 (rush hours) when $\phi \sim U(0, 60^\circ)$ and D has a log-normal distribution with a mean value μ_s and a standard deviation σ_s given in Table 3.4. The figure shows that the simulated path loss matches the theoretical distribution given in (4.5). Furthermore, the figure shows that the path loss values at late hours are higher than values at rush hours, as the mean values of the inter-vehicle spacing μ_s and μ_d are larger at late hours compared to the rush hours as provided in Table 3.4.

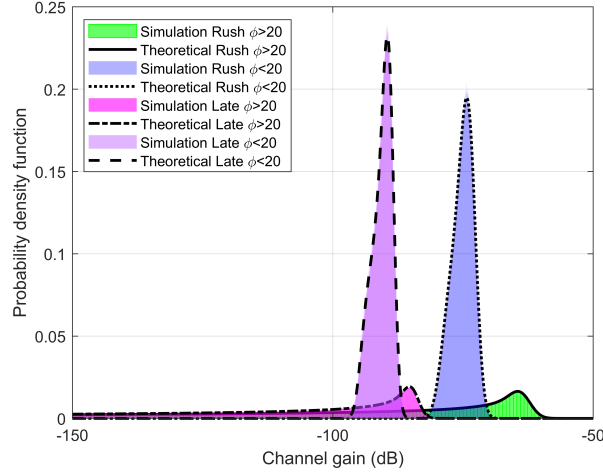


Figure 4.3: The statistical and simulated PDFs of the LOS component of the V2V-VLC path loss using the piecewise Lambertian model when the inter-vehicle spacing D has a log-normal distribution at 00:00-03:00 (late hours) and 12:00-15:00 (rush hours).

4.2.2 Piecewise Lambertian model

Viriyasitavat et al. (2013) considered the radiation pattern of a Yamaha Cygnus-X scooter taillight to establish a path loss model of the V2V-VLC channel. The study described the path loss (in dB) by a piecewise Lambertian model:

$$P_L = 10 \log(A_r(m+1)) - 10 \log(2\pi) - 10\zeta \log D + 10(m+1) \log \cos(\phi), \quad (4.6)$$

where ζ is the path loss exponent. A linear least-square method was used to estimate ζ and the associated half-power angles $\Psi_{1/2}$ for different irradiance angles ϕ as given in Table 4.2.

Considering the similarity between the path loss of the Lambertian model in (4.2) and the piecewise Lambertian model in (4.6), the statistical distribution of the path loss is given by:

$$P_L(x; \mu_k, \sigma_k) = \frac{1}{g\phi_o\sigma_k\sqrt{2\pi}} \int_{\alpha_m}^0 \frac{\exp\left(-\frac{(x-y-\mu_k)^2}{\sigma_k^2}\right)}{\sqrt{e^{-2y/g} - 1}} dy, \quad (4.7)$$

where the standard deviation is $\sigma_k = 20\sigma_s/\ln(10)$ and the mean is $\mu_k = 10 \log(A_r(m+1)/2\pi) - 10\zeta\mu_s/\ln(10)$.

Table 4.2: Parameters of the piecewise Lambertian model (Viriyasitavat et al., 2013).

Irradiance angle, ϕ	Path loss exponent, ζ	Half-power angle, $\Psi_{1/2}$
$\phi \leq 20^\circ$	$\zeta = 2.597$	$\Psi_{1/2} = 61.33^\circ$
$\phi \geq 20^\circ$	$\zeta = 3.55$	$\Psi_{1/2} = 4.51^\circ$

Figure 4.3 illustrates the PDFs of the channel path loss obtained by the piecewise Lambertian model at 00:00-03:00 (late hours) and 12:00-15:00 (rush hours), when $\phi \sim U(0, 60^\circ)$ and log-normally distributed D as given in Table 3.4. The figure shows that the path loss distribution obtained using the simulation fits the theoretical distribution given in (4.7). The figure shows the impact of irradiance angle ϕ on the distribution of V2V-VLC path loss. The mean values of -90 dB and -75.1 dB, at 0:00-03:00 and 12:00-15:00 respectively, when $\phi \leq 20^\circ$, while the mean values are -288 dB and -266.4 dB, at 0:00-03:00 and 12:00-15:00, respectively, when $\phi \geq 20^\circ$. Hence, establishing a communication link is feasible at a narrower irradiance angle ϕ .

4.2.3 Gaussian model

Moreno and Sun (2008) and Ding et al. (2016) proposed a series of Gaussian functions to model the asymmetrical three-dimensional intensity distribution of LEDs from different manufacturers. According to Moreno and Sun (2008); Ding et al. (2016), the horizontal intensity distribution of LEDs is given by:

$$I(\phi) = g1_1 \exp\left(-\ln(2)\left(\frac{|\phi| - g2_1}{g3_1}\right)^2\right) + g1_2 \exp\left(-\ln(2)\left(\frac{|\phi| + g2_2}{g3_2}\right)^2\right), \quad (4.8)$$

where ($g1_i$, $g2_i$ and $g3_i$) are coefficient identified by linear regression. Moreno and Sun (2008) reported that two to three terms of Gaussian functions can accurately describe the radiation distribution of optical sources.

The Philips LUXEON® Rebel is taken as an example of a vehicle source to develop the Gaussian model where radiation intensity is simulated with a non-sequential raytracing

Table 4.3: *Coefficients of Gaussian function which describes luminous intensity distribution of Philips LUXEON® Rebel LED (Moreno and Sun, 2008; Ding et al., 2016).*

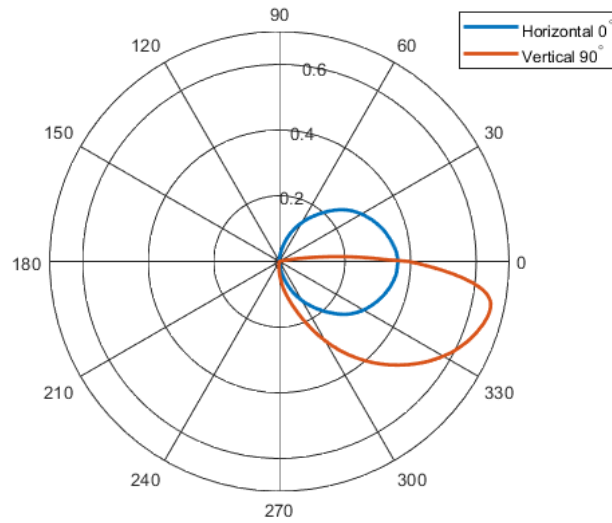
coefficient	Lower bound	Upper bound
g_{1_1}	0.76	1
g_{1_2}	0.11	1.10
g_{2_1}	0	0
g_{2_2}	45°	45°
g_{3_1}	29°	29°
g_{3_2}	21°	21°

software OpticStudio®. Figure 4.4 (a) illustrates the horizontal and vertical planes of the radiation pattern of the vehicle's source. The linear regression method is used to calculate the numerical values of the coefficients g_{1_1} , g_{1_2} , g_{2_1} , g_{2_2} , g_{3_1} and g_{3_2} from the normalized intensity of the source intensity pattern in Figure 4.4 (b). The results reveal that the normalized intensity of the source pattern in the horizontal plane matches the normalized intensity of a single Philips LUXEON® Rebel LED. This is due to the alignment between the transmitter and receiver (as explained in Section 2.2.2.1 $\Phi = 0^\circ$) in the horizontal plane is evidenced by Figure 4.4 (b) that shows that the radiation intensity of a vehicle source in this plane has the same pattern for a single LED. Hence, the linear regression results of the numerical coefficients provide similar values to that obtained in (Moreno and Sun, 2008; Ding et al., 2016) with a root-mean-square-error (RMSE) value of 0.02. The numerical values of the coefficients g_{1_1} , g_{1_2} , g_{2_1} , g_{2_2} , g_{3_1} and g_{3_2} are given in Table 4.3.

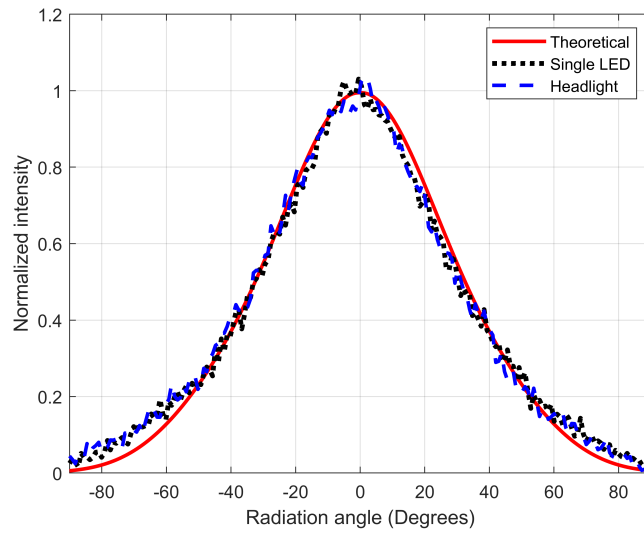
Considering that $I(\phi)$ is given by a combination of two shifted Gaussian functions, the term $I(\phi) \cos(\phi)$ in (2.16) can be approximated by (Ben-Arie, 1991):

$$I_C(\phi) = I(\phi) \cos(\phi) = c_1 \cos(c_2\phi) + c_3, \quad (4.9)$$

where the coefficients (c_1 , c_2 , and c_3) are established numerically. Therefore, the statistical distribution of the term $10 \log(I(\phi) \cos(\phi))$ in (2.16) is given by the logarithmic transforma-



(a)



(b)

Figure 4.4: a) Polar plot of the radiation pattern of vehicle source which uses Philips LUXEON® Rebel in the horizontal 0° and vertical 90° planes b) The normalized intensity pattern of the theoretical Gaussian model, single Philips LUXEON® LED and vehicle source which uses Philips LUXEON®.

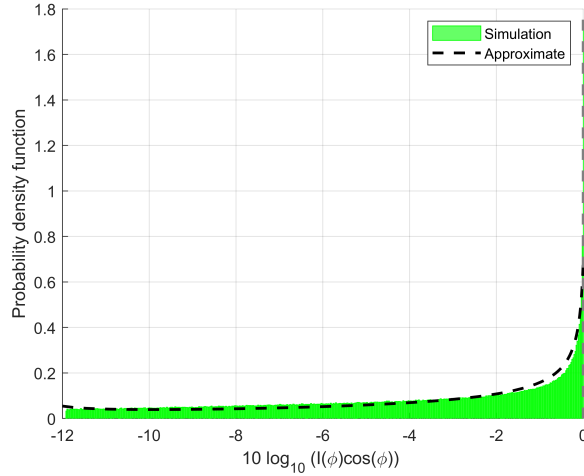


Figure 4.5: The numerical evaluation of the term $10 \log(I_C(\phi))$ when $\phi \sim U(0, 60^\circ)$ and the LED Philips LUXEON[®] Rebel is used.

tion of the sinusoidal function $I_C(\phi)$, which can be approximated by (Papoulis et al., 2002, P. 97):

$$f_Y(y) = \frac{e^{y/a}}{a c_2 \phi_o \sqrt{c_1^2 - (e^{y/a} - c_3)^2}} \quad c_4 < y < c_5, \quad (4.10)$$

where c_4 and c_5 are numerical boundary constants and $a = 10/\ln(10)$. For example, Figure 4.5 shows a numerical fit of $10 \log(I_C(\phi))$ and analytical distribution in (4.10) when $\phi \sim U(0, 60^\circ)$, with the coefficients $g1_1, g1_2, g2_1, g2_2, g3_1$ and $g3_2$ given in Table 4.3. The numerical evaluation shows that $c_1 = 0.48, c_2 = 1/3, c_3 = 0.534, c_4 = 0$ and $c_5 = 11.9$ offers a close fit with a mean square error of 0.25.

Therefore, the distribution of path loss in (2.16) is given by the convolution between the normal distribution of terms $10 \log(A_r) - 10 \log(2\pi) - 20 \log D$ in (3.6) and the distribution given in (4.10). This convolution gives the following distribution (Papoulis et al., 2002):

$$P_L(x; \mu_m, \sigma_m) = \frac{1}{a c_2 \phi_m \sigma_m \sqrt{2\pi}} \int_{c_5}^{c_4} \frac{\exp\left(-\frac{(x-y-\mu_m)^2}{\sigma_m^2} - \frac{y}{a}\right)}{\sqrt{c_1^2 - (e^{y/a} - c_3)^2}} dy. \quad (4.11)$$

The PDFs of the channel path loss obtained by the Gaussian model at 00:00-03:00 (late hours) and 12:00-15:00 (rush hours) are shown in Figure 4.6, with $\phi \sim U(0, 60^\circ)$ and log-normally distributed D given in Table 3.4. The figure shows that the MC simulation of

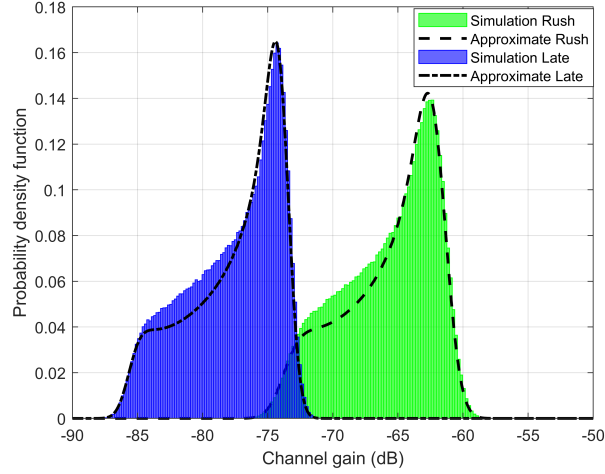


Figure 4.6: The probability density function of channel path loss obtained by the Gaussian model of the LED Philips LUXEON® Rebel at 00:00-03:00 (late hours) and 12:00-15:00 (rush hours).

the path loss distribution in (2.16), when $I(\phi)$ is described by the Gaussian model in (4.8), matches the theoretical distribution in (4.11) for the Philips LUXEON® Rebel LED.

Furthermore, Figure 4.7 shows the CDFs of the path loss obtained by MC simulation and raytracing using the Gaussian model at 00:00-03:00 and 12:00-15:00. The figure shows the path loss obtained by raytracing matches the path loss obtained by the Gaussian model and predicts the mean values at 00:00-03:00 and 12:00-15:00.

In general, the results show that the path loss values at late hours are higher than the values at rush hours because the mean values of the inter-vehicle spacing are larger at late hours than at rush hours see Table 3.4.

4.2.4 Empirical model of Toyota Altis Headlight

The radiation intensity pattern of the Toyota Altis Headlight was used by Memedi et al. (2017) to derive an analytical formula of the V2V-VLC channel path loss given by:

$$P_L[dB] = \alpha - 10\beta \log(D + 1) + \epsilon \cos\left(\frac{2\pi(\phi + 90)}{\omega}\right), \quad (4.12)$$

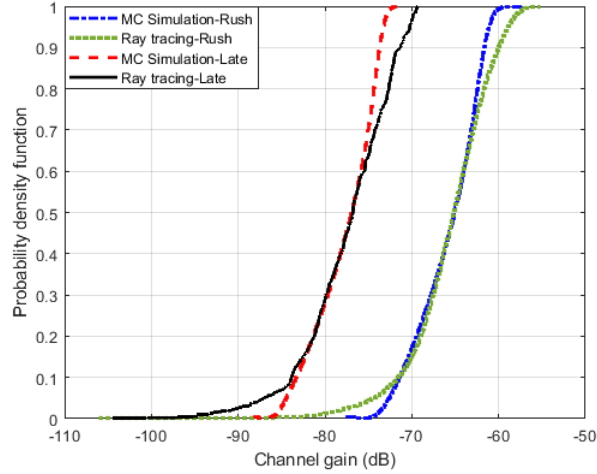


Figure 4.7: The CDFs of the path loss obtained by raytracing and the *MC* simulation of the Gaussian model of a *LED* at 00:00-03:00 and 12:00-15:00.

where the numerical coefficients $\alpha = 695.3$, $\delta = -717.3$, $\beta = 4.949$, $\epsilon = 63.13$ and $\omega = 173$ were calculated from the received power measurements of the vehicle headlight using the non-linear least squares method. Given that D follows a log-normal distribution with mean values given in Table 3.4 (i.e mean values $\gg 1$), the term $10\beta \log(D + 1)$ can be approximated by a normal distribution:

$$P_L(x; \mu_o, \sigma_o) = \frac{1}{\sigma_o \sqrt{2\pi}} \exp\left(-\frac{(x - \mu_o)^2}{2\sigma_o^2}\right), \quad (4.13)$$

where σ_o is the standard deviation and μ_o is the mean. The values of the standard deviation σ_o and the mean μ_o can be found numerically by $\mu_o + \sigma_o^2/2 = \ln(1 + e^{\mu_s + \sigma_s^2/2})$ because the constant shift of $D + 1$ affects the standard deviation σ_o and the mean μ_o . The numerical values of σ_o and μ_o are given in Table 4.4.

Considering that angle ϕ has a uniform distributed $\phi \sim U(0, \phi_o)$, the statistical distribution of the term $\epsilon \cos\left(\frac{2\pi(\phi+90)}{\omega}\right)$ is given as a linear transformation of a cosine distribution (Papoulis et al., 2002, P. 97):

$$f_{Z_\phi}(z_\phi) = \frac{\omega}{2\pi\phi_o\sqrt{\epsilon^2 - z_\phi^2}} \quad \alpha_{cmin} < z_\phi < \alpha_{cmax}, \quad (4.14)$$

Table 4.4: Parameters of log-normal distribution that describes the inter-vehicle spacing.

Time	Distribution	Mean value (m)	μ_s	σ_s	μ_o	σ_o
0:00-3:00	Log-normal	48.72	3.88	0.09	3.9	0.08
12:00-15:00	Log-normal	12.37	2.51	0.12	2.59	0.11

where $\alpha_{cmin} = \epsilon \cos(2\pi(\phi_o)/\omega)$ and $\alpha_{cmax} = \epsilon \cos(2\pi(\phi_o + 90)/\omega)$.

Therefore, P_L , the statistical distribution of the path loss in (4.12) is given by a convolution between the distribution in (4.13) and the distribution in (4.14)

$$P_L(x; \mu_c, \sigma_c) = \frac{\omega}{(2\pi)^{(3/2)}\phi_o\sigma_c} \int_{\alpha_{cmin}}^{\alpha_{cmax}} \frac{\exp\left(-\frac{(x-y-\mu_c)^2}{\sigma_c^2}\right)}{\sqrt{\epsilon^2 - y^2}} dy, \quad (4.15)$$

where $\sigma_c = 10\beta\sigma_o/\ln(10)$ is the standard deviation and $\mu_c = \alpha - 10\beta\mu_o/\ln(10)$ is the mean.

The PDFs of channel path loss obtained by the empirical radiation model at 00:00-03:00 (late hours) and 12:00-15:00 (rush hours) is illustrated in Figure 4.8. The figure shows that the path loss distribution obtained using MC simulation matches the theoretical analysis given by (4.15) for the empirical model. This model also shows that the path loss values at late hours are higher than values at rush hours due to the large mean values of the inter-vehicle spacing μ_s , and μ_o at late hours compared to the rush hours as illustrated in Table 3.4.

4.2.5 Comparison between different radiation pattern models

A comparison between the CDFs for path loss of Lambertian, piecewise Lambertian, empirical and Gaussian models is given in Figure 4.9. Table 4.5 summarises the mean and standard deviation values of the path loss. The Gaussian model has the lowest path loss values with a difference of 2 dB between the Gaussian and Lambertian radiation pattern. The difference exceeds 8 dB between Gaussian and empirical radiation patterns. This difference in path loss values indicates that path loss depends on the radiation pattern of the vehicles' sources. Since different manufacturers use different technologies and optical systems that significantly

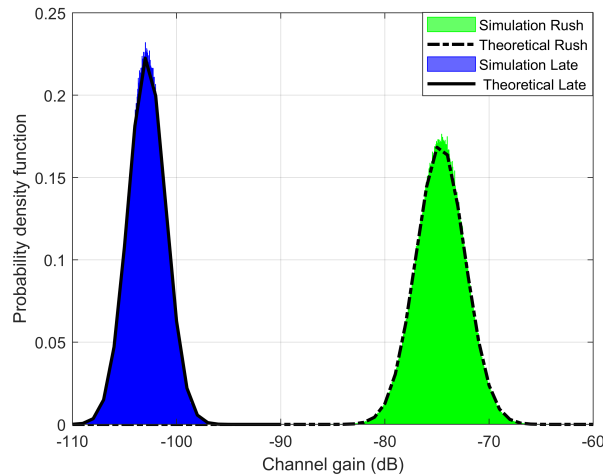


Figure 4.8: *The PDF of channel path loss obtained by the empirical radiation model at 00:00-03:00 (late hours) and 12:00-15:00 (rush hours).*

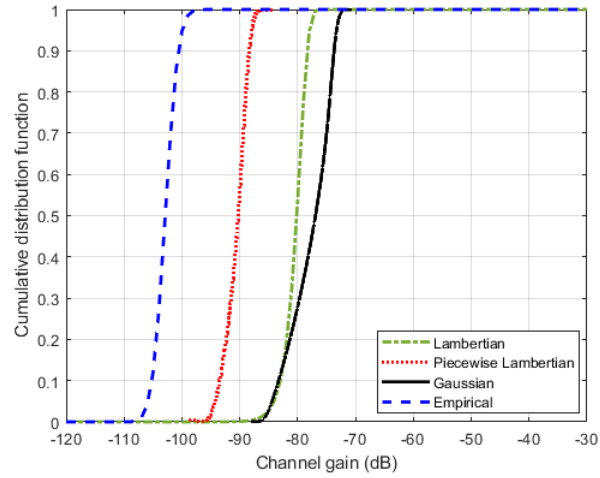
affect the radiation pattern, the path loss for the V2V-VLC system also varies for various light sources.

The following section investigates the impact of weather conditions on the statistical path loss model of the LOS V2V-VLC channel component.

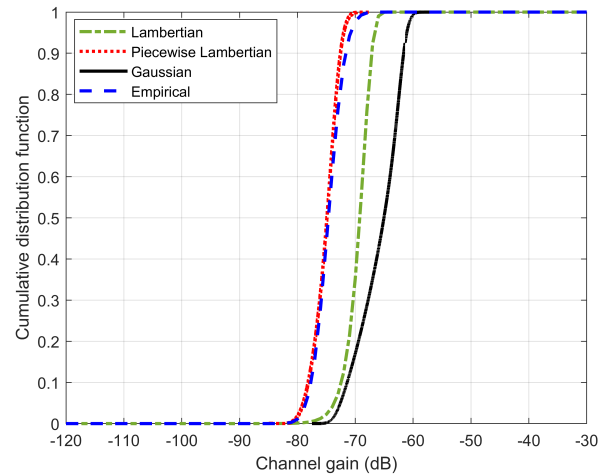
4.3 Impact of weather conditions on LOS V2V-VLC channel

Kim et al.'s model is used to study the effect of weather conditions on the V2V-VLC channel. As explained in Section 2.2.1, the experimental models showed that weather conditions induce a wavelength-dependent power attenuation of optical signals and limit the visibility ranges of VVLC links. This section examines the effect of weather conditions on the V2V-VLC channel under the variable traffic density at different times of the day, when D has a log-normal distribution with parameters given in Table 3.4.

Figure 4.10 shows the impact of weather on the V2V-VLC path loss in (2.5) when the geometrical propagation path loss is described by a) Lambertian in (4.5), b) Piecewise



(a)



(b)

Figure 4.9: The CDFs of path loss for the Lambertian model, Gaussian angular distribution model and empirical asymmetric radiation patterns at a) 00:00-03:00 and b) 12:00-15:00.

Lambertian in (4.7) c) empirical in (4.15), d) Gaussian models in (4.11) at 00:00-03:00 (right-side) and 12:00-15:00 (left-side). The angular deviation is $\phi \sim U(0, 60^\circ)$ and D has a log-normal distribution with a mean value μ_s and a standard deviation σ_s given in Table 3.4. The numerical values of the weather attenuation and parameters in (2.6) and

Table 4.5: Summary of mean and variance values of the statistical path loss distributions.

Time	Model	mean value (dB)	variance
0:00-3:00	Lambertian	-79.6	3.7
	Piecewise Lambertian	-90.7 ($\phi < 20^\circ$)	3.9
		-288.2 ($\phi > 20^\circ$)	inf
	Gaussian	-77.7	13.1
	Empirical	-102.8	3.2
12:00-15:00	Lambertian	-68.6	4.7
	Piecewise Lambertian	-75.1 ($\phi < 20^\circ$)	5
		-266.4 ($\phi > 20^\circ$)	inf
	Gaussian	-65.8	14.2
	Empirical	-74.7	5.4

(2.7) for different weather conditions are provided in Table 4.6 (Kim et al., 2015; Hu et al., 2007). These attenuation values assumed a red wavelength 650 nm and a PD responsivity of $\gamma = 10.2 \text{ mV} \cdot (\mu\text{W} \cdot \text{cm}^{-2})^{-1}$ (Kim et al., 2015; Hu et al., 2007). The resulting mean path loss values are summarised in Table 4.7. The figure and table show that weather conditions induce additional attenuation by shifting the mean path loss values without changing the statistical distribution of the V2V-VLC path loss. This is expected as the events of weather conditions and geometrical changes due to vehicles' mobility are independent. Furthermore, the results show that heavy fog adds high attenuation values that can cause a communication link outage.

4.4 Summary

This chapter has analysed the impact of dynamic traffic and radiation pattern of vehicles' sources on the LOS component of the V2V-VLC channel. Statistical models were developed to describe the path loss considering dynamic traffic conditions that change the inter-vehicle

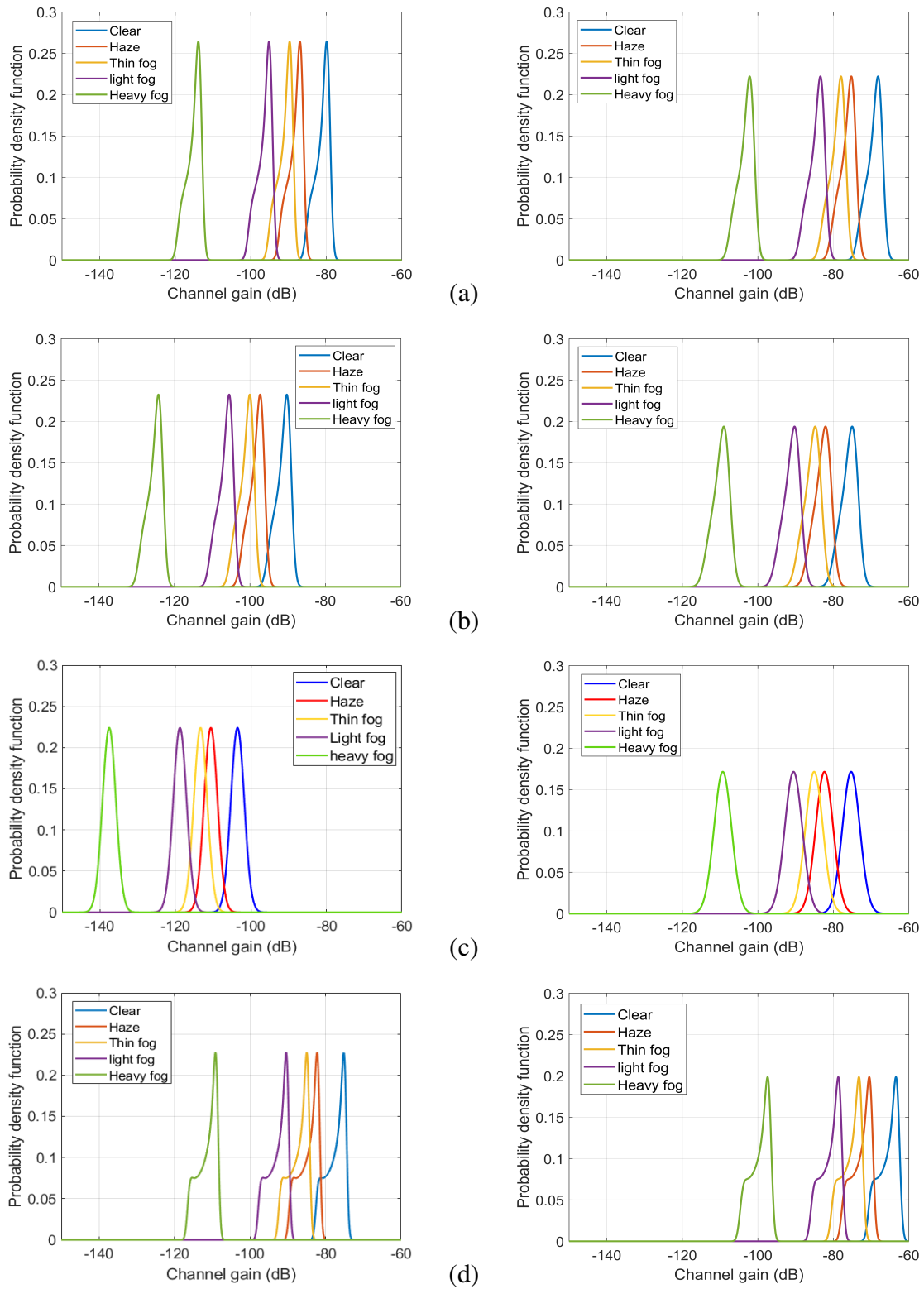


Figure 4.10: Weather impact on V2V-VLC path loss for a) Lambertian, b) Piece-wise Lambertian c) Empirical, d) Gaussian models at 00:00-03:00 (right-side) and 12:00-15:00 (left-side).

Table 4.6: *Attenuation values and parameters for different weather conditions (Kim et al., 2015; Hu et al., 2007).*

This item has been removed due to 3rd Party Copyright. The unabridged version of the thesis can be viewed at the Lanchester Library, Coventry University.

Table 4.7: *Summary of mean path loss values of the statistical path loss (in dB) for different weather conditions and radiation models.*

Time	Model	Clear	Haze	Thin fog	Light fog	heavy fog
0:00-3:00	Lambertian	-80.3	-87.37	-90.1	-95.56	-114.29
	Piecewise Lambertian	-91.4	-98.47	-101.2	-106.66	-125.34
	Gaussian	-78.4	-85.47	-88.2	-93.66	-112.39
	Empirical	-103.5	-110.57	-113.3	-118.76	-137.49
12:00-15:00	Lambertian	-69.3	-76.37	-79.1	-89.56	-103.29
	Piecewise Lambertian	-75.8	-82.87	-85.6	-91.06	-109.79
	Gaussian	-66.5	-73.57	-76.3	-81.76	-100.5
	Empirical	-75.4	-82.5	-85.2	-90.7	-109.4

spacing as well as the irradiance angle. The study examined four radiation pattern models (Lambertian, piecewise Lambertian, Gaussian and empirical) to describe the asymmetrical angular distribution of the light sources of the vehicles. The radiation pattern differs depending on the function, design and manufacturer of the light sources. The proposed statistical models showed that the path loss model is given by the convolution between inter-vehicle spacing and radiation pattern distributions. Among all radiation pattern models, the Gaussian model

can be adopted to describe the radiation pattern of vehicles' sources with different designs.

This chapter has also investigated the impact of the weather on the LOS component of the V2V-VLC channel. The results showed that different weather conditions add attenuation that shifts the mean path loss value with the highest attenuation value observed under heavy fog condition. The statistical distributions of the channel path loss due to dynamic traffic do not change with various weather conditions.

As explained in Section 2.2.2, V2V-VLC CIR combines the LOS and NLOS propagation paths. This chapter investigated the LOS component of the V2V-VLC channel. The multipath propagation and NLOS component is discussed in the following Chapter 5.

Chapter 5

Multipath Vehicle-to-Vehicle Visible Light Communications Channel

The **V2V-VLC** channel can be described as a multipath channel where the signal arrives from **LOS** and **NLOS** propagation paths. Each **NLOS** path is associated with a reflector object. Hence, the received signal consists of multiple attenuated and time-delayed copies of the original signal. This causes a variation in the received power and the temporal properties of the channel. The dynamic nature of the **V2V-VLC** channel adds further variation to the received power and the temporal properties of the channel.

Therefore, path loss and channel temporal properties due to multipath propagation and reflection are examined in this chapter. Reflection from different road objects surfaces is first examined. A statistical path loss of the **NLOS V2V-VLC** channel model is investigated considering single and multiple reflectors. Two-dimensional (time and delay) temporal properties of **V2V-VLC** channel is studied under dynamic traffic conditions at different times of the day.

For mathematical simplicity, Lambertian and piecewise-Lambertian models are used in this chapter to establish the analytical model of the **NLOS** component. However, other models (i.e. Gaussian and empirical) can be used with additional mathematical complexity.

The rest of this chapter is organised as follows: an overview of research works that

considered the impact of reflection and temporal properties of multipath V2V-VLC channel is provided in Section 5.1. Reflection from different objects and surfaces is examined in Section 5.2. A statistical path loss model of the multipath V2V-VLC channel is established in Section 5.3. A discussion and analysis of the temporal properties of the V2V-VLC channel are provided in Section 5.4. A summary of the chapter is given in Section 5.5.

5.1 Related works

Multipath propagation is a result of reflection and scattering from the surrounding objects. Its impact depends on the operation wavelength, size of detector and mobility (Ghassemlooy et al., 2019, P. 78). The detector offers a spatial diversity that limits the impact of multipath fading because the operation wavelengths of the VLC systems are three orders of magnitude less than the size of the detector area (Ghassemlooy et al., 2019, P. 78). However, changes associated with the mobile transmitter, receiver and surrounding objects locations, which are in the order of centimetres or higher, affect the channel path loss and temporal characteristics (Ghassemlooy et al., 2019, P. 79). The following sections discuss the previous work that investigated the multipath propagation due to reflection and temporal properties of the VVLC channel.

5.1.1 Impact of Reflection on VVLC Channel

The impact of reflection from the surrounding surfaces on VVLC channel was studied in the literature. Liu et al. (2011) measure the impact of reflection from vehicles on the packet delivery rate (PDR) of the VVLC system. The study showed that 100% PDR can be achieved from reflection only when the LOS is blocked and the distance between the reflector and the receiver is less than 1.5 m.

Lee et al. (2012b) studied the reflection from vehicles and surrounding buildings at cross-road and in urban street scenarios for V2V and V2I communications. The study considered a full-absorbing road surface material and ignored reflection from the road surface. The results

showed that the reflection in the street scenario is higher than in the crossroad scenario. The number of NLOS channel taps in the V2I communication link is higher than that in the V2V communication link.

Luo, Ghassemlooy, Minh, Bentley, Burton and Tang (2015) examined light reflection from the road surface for different receiver positions and road surface physical states. The study indicated that the power received from reflection from the road surface depends on the heights of the receiver and the physical state of the road surface as the reflection from wet roads is higher than from dry roads.

The measurement-based study in (Turan et al., 2018) compared the channel gain for LOS and NLOS components. The NLOS component was examined in the presence and absence of nearby vehicles. The results showed that the LOS channel gain is higher than the NLOS channel gain by more than 10 dB and the presence of nearby vehicles induces an additional channel gain of 3.519 dB. However, the analytical study in (Al-Kinani, Sun, Wang, Zhang, Ge and Haas, 2018) showed that the received power from the reflection component of the channel is less than the received power from the LOS component by at least two orders of magnitude.

Abuella et al. (2019) proposed a VLiDAR system that estimates the vehicles speed by sensing the variation of the vehicle's headlamp pattern. The study examined a simulation-based path loss model against the Lambertian model for the asymmetric radiation pattern of the vehicle's headlamp. The results revealed a difference of more than 10 dB between the Lambertian and the simulated path loss values. This difference was attributed to reflection from the road surface. Similarly, Eldeeb, Eso, Uysal, Ghassemlooy, Zvanovec and Sathian (2020) examined a simulation-based path-loss model against the Lambertian model while studying the asymmetrical radiation pattern of a vehicle's taillight. The results reported a non-negligible received power from road reflection that is up to 30% of the received power from the LOS path. However, reflection from the road surface should be reduced to the minimum possible values (Strbac-Hadzibegovic et al., 2019; Adrian and Jobanputra, 2005; Puttonen et al., 2009; Technical Committee CPL/34, 1996).

Previous studies have investigated the reflection from the surrounding vehicles considering different scenarios. However, none of these studies have established a reproducible statistical

model that describes the path loss of the **NLOS** component of the **V2V-VLC** channel. The following section provides an overview of the temporal properties of the multipath **VVLC** channel.

5.1.2 Temporal properties of multipath VVLC channel

Few studies have investigated the temporal properties of the **VVLC** channel. [Cui et al. \(2014\)](#); [Chen et al. \(2016\)](#) measured the coherence time and autocorrelation function of **VVLC** channels. The measurements in ([Chen et al., 2016](#)) showed that the coherence time of the channel is of the order of hundreds of milliseconds. Similarly results were obtained in [Cui et al. \(2014\)](#) by estimating the autocorrelation function and coherence time for different vehicles traces. Therefore, considering the data symbol duration, the **VVLC** channel shows slow fading behaviour.

Simulation-based studies in ([Lee et al., 2012b](#)) showed that the delay spread of **V2V-VLC** and **V2I-VLC** channels is in the range of 5 ns to 30 ns. [Turan et al. \(2018\)](#) measured the delay profile and delay spread of the **VVLC** channel. The results showed that the time dispersion increases with the increase in inter-vehicle spacing between vehicles. The estimated **RMS** delay spread values were two orders of magnitude higher than the values of [Lee et al. \(2012b\)](#). [Al-Kinani, Sun, Wang, Zhang, Ge and Haas \(2018\)](#) showed that the **RMS** delay spread fit Gaussian distributions with a mean value of 0.55 ns.

[Torres-Zapata et al. \(2020\)](#) studied the time variation of a full-duplex **V2I-VLC** system in an urban tunnel. The measurement for two transmitter positions centred on the ceiling and mounted on the sidewall of the tunnel showed that the downlink channel has slow fading behaviour with a coherence time of <150 ns and 200 ns, respectively. The up-link channel has a larger fading with a coherence time of <160 ns. The study also showed that the **RMS** delay spread values of the downlink and the uplink channel are <1 ns and between 1 ns and 6 ns, respectively.

The previous studies estimated single-dimensional temporal properties, which do not provide information about the time stationary properties of the channel during different times

of the day. In addition, studies adopted different assumptions about the magnitude of reflection from road materials.

To avoid inaccurate assumptions about reflection from the surrounding objects, it is vital to quantify the path loss of reflection component from different road materials. The following section examines the path loss from reflection CIR component from road surface materials with different nature and physical states.

5.2 Reflection from different objects and surfaces

Considering that the LOS DC gain from the source to the j^{th} reflector $H_{LOS_j}(0)$ in (2.18) can be described by Lambertian or piecewise-Lambertian models (depends on ζ^1) and given by:

$$H_{LOS_j}(0) = \frac{A_r(m+1)}{2\pi r_j^\zeta} \cos^m(\phi_T^j) \cos(\theta_s^j), \quad (5.1)$$

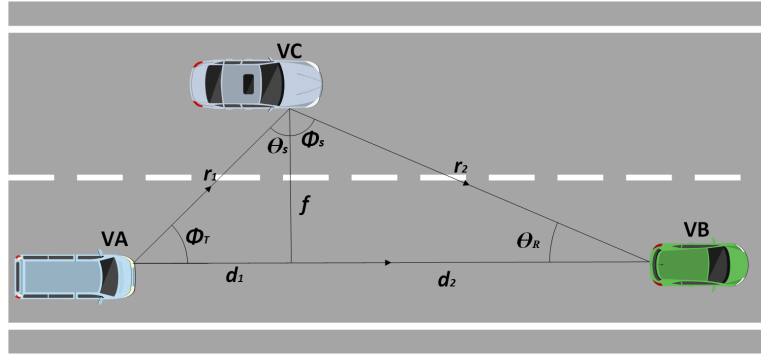
where, ϕ_T^j is the irradiance angle, θ_s^j is the incidence angle with respect to the normal to the j^{th} reflector and r_j is the distance from the transmitter to the j^{th} reflector. Therefore, the DC gain of V2V-VLC in (2.18) can be re-written as:

$$H_{NLOS}(0) = \sum_{j=1}^{J_r} \frac{\rho A_r(m+1)}{(2\pi)^2 r_j^\zeta r_2^2} \cos^m(\phi_T^j) \cos(\phi_s^j) \cos(\theta_s^j) \cos(\theta_R^j). \quad (5.2)$$

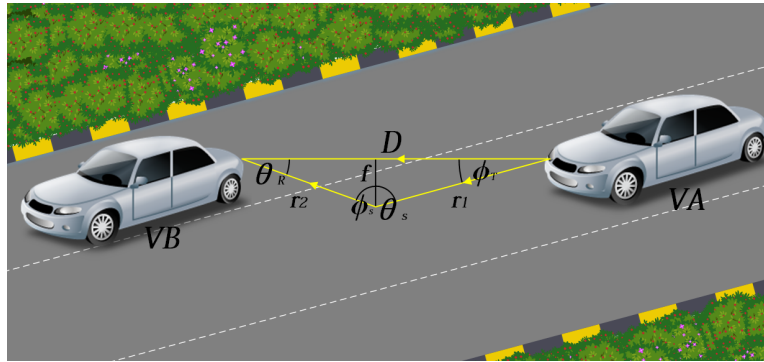
NLOS links due to reflection from the road surface and neighbouring vehicle are illustrated in Figure 5.1. The figure shows V2V-VLC links between vehicles VA and VB. The vehicle VA transmits the data using a headlight, and the vehicle VB receives it with a PD centred at the rear end of the vehicle. In Figure 5.1 a) a vehicle VC is the nearest potential reflector.

The inter-vehicle spacing ($D = d_1 + d_2$) changes continuously with the movement of VA, VB and VC. Consequently, the angles ϕ_T , θ_R , ϕ_s and θ_s also change because they depend on the relative location of VA, VB and VC. Using trigonometric relations, the terms $\cos(\phi_T)$,

¹ $\zeta=2$ for the Lambertian model and it is given in Table 4.2 for the piecewise-Lambertian model



(a)



(b)

Figure 5.1: Geometry of NLOS link when reflection from road surfaces and neighbouring vehicles is considered.

$\cos(\theta_R)$, $\cos(\phi_s)$ and $\cos(\theta_s)$ can be given by:

$$\cos(\phi_T) = \frac{d_1}{r_1}, \quad (5.3)$$

$$\cos(\theta_R) = \frac{d_2}{r_2}, \quad (5.4)$$

$$\cos(\phi_s) = \frac{f}{r_2}, \quad (5.5)$$

$$\cos(\theta_s) = \frac{f}{r_1}, \quad (5.6)$$

where d_1 and d_2 are the longitudinal inter-vehicle spacing, r_1 and r_1 are the distances from the transmitter to the reflector and from the reflector to the receiver, respectively, and f is the lateral inter-vehicle spacing.

Table 5.1: Reflective indexes of different road object materials.

Object	Reflective index
Vehicles	0.80 (Al-Kinani et al. 2018)
Wet road surface	0.25 (Luo et al. 2014)
Portland cement concrete	0.10 (Adrian and Jobanputra, 2005)
Asphalt with a very smooth texture	0.08 (Adrian and Jobanputra, 2005)

Reflectivity indices of vehicles and conventional road object materials with different natural and physical states are summarized in Table 5.1. The table shows that the reflectivity of vehicle surface (i.e. coated steel) is 0.8 which is relatively high compared to other objects surfaces with reflectivity index values that do not exceed 0.25.

Figure 5.2 shows a comparison between reflection from different objects and surfaces, including reflections from a vehicle, wet road surfaces, Portland cement concrete and asphalt with a very smooth texture, according to the reflectivity indexes in Table 5.1. The figure is obtained using MC simulation assuming a half-power angle of $\Psi_{1/2} = 20^\circ$, both the transmitter and receiver are mounted at 0.4 m, the lateral distance between vehicles is 1 m and the inter-vehicle spacing follows a log-normal distribution with parameters given in Table 3.4.

Figure 5.2 shows that the mean values of the path loss are -111.7 dB, -124.5 dB, -128.5 dB and -129.5 dB for reflection from vehicles, wet road surfaces, Portland cement concrete and asphalt with a very smooth texture, respectively. Hence, the power received from reflection of vehicles is at least 12 dB higher than the reflection from other material. This is because the reflectivity index value of the vehicle surface is higher than other materials. Therefore, without loss of generality, this thesis focuses on the reflection from adjacent vehicles.

5.3 Path loss of NLOS V2V-VLC channel

In realistic scenarios, multiple reflectors can co-exist in the adjacent lanes. Therefore, a statistical path loss model is established for single and multiple reflectors scenarios in the

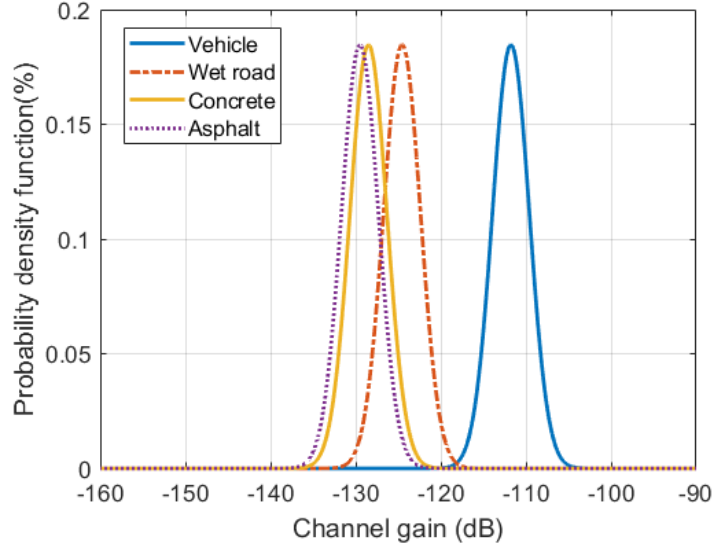


Figure 5.2: Reflection from different surfaces with different nature and physical state includes reflection from vehicles, wet road surface, Portland cement concrete and asphalt with a very smooth texture.

following section.

5.3.1 Single reflector scenario

The path loss of NLOS V2V-VLC channel for a single reflector scenario can be obtained from (5.2) when $j=1$ and using the trigonometric relations (5.3-5.6). Therefore, channel DC gain of a single reflector can be given as:

$$H_{NLOS}(0) = \frac{\rho A_r (m+1) f^2 d_1^m d_2}{(2\pi)^2 r_1^{(m+\zeta+1)} r_2^4}. \quad (5.7)$$

The path loss (in dB) of the NLOS component for a single reflection is given by:

$$P_L = 10 \log(\rho A_r (m+1)) + 20 \log(f) + 10 m \log(d_1) + 10 \log(d_2) \\ - 20 \log(2\pi) - 10(m+\zeta+1) \log(r_1) - 40 \log(r_2). \quad (5.8)$$

Finding a realistic statistical distribution to describe the lateral distances f depends on many variables such as traffic density, size of vehicles, speed limits, manoeuvring and lane

width (Pal and Mallikarjuna, 2010; Kim et al., 2015). Different distributions were proposed and each distribution was obtained to a specific variable (Pal and Chunchu, 2019; Pal and Mallikarjuna, 2010; Wang et al., 2014). Therefore, to avoid an unrealistic assumption about the statistical distribution, lateral distances f is assumed to be quantized in the analysis. Considering that the inter-vehicle spacing d_1 and d_2 follows a log-normal distribution with parameters given in Table 3.2 and f is constant, the distances r_1 and r_2 are given by:

$$r_1 = \sqrt{d_1^2 + f^2}, \quad (5.9)$$

$$r_2 = \sqrt{d_2^2 + f^2}. \quad (5.10)$$

Because f is constant, r_1 and r_2 can be described by a log-normal distribution with μ_r and σ_r (Papoulis et al., 2002):

$$\mu_r = \frac{1}{2} \ln \left(\frac{E^2}{\sqrt{V + E^2}} \right), \quad (5.11)$$

$$\sigma_r = \frac{1}{2} \sqrt{\ln \left(\frac{V + E^2}{E^2} \right)}, \quad (5.12)$$

and

$$E = \exp \left(2(\mu_s + \sigma_s^2) \right) + f^2, \quad (5.13)$$

$$V = \exp \left(4(\mu_s + 2\sigma_s^2) \right) - \exp \left(4(\mu_s + \sigma_s^2) \right), \quad (5.14)$$

where E is the expectation and V is the variance of the terms $d_1^2 + f^2$ and $d_2^2 + f^2$.

If d_1 , d_2 , r_1 and r_2 have log-normal distributions, then the terms $\log(d_1)$, $\log(d_2)$, $\log(r_1)$ and $\log(r_2)$ have normal distributions (Papoulis et al., 2002, P. 97). As a result, the path loss in (5.8), which is given as a summation of normal distributions, has a normal distribution (Papoulis et al., 2002, P. 198), as follows:

$$P_L(x; \mu_q, \sigma_q) = \frac{1}{\sigma_q \sqrt{2\pi}} \exp \left(-\frac{(x - \mu_q)^2}{2\sigma_q^2} \right), \quad (5.15)$$

where the variance is given as (Papoulis et al., 2002, P. 141):

$$\begin{aligned} \sigma_q^2 = & \left(10m \frac{\sigma_s}{\ln(10)} \right)^2 + \left(10 \frac{\sigma_s}{\ln(10)} \right)^2 + \left(10(m + \zeta + 1) \frac{\sigma_r}{\ln(10)} \right)^2 + \left(40 \frac{\sigma_r}{\ln(10)} \right)^2 \\ & - Cov(d_1, r_1) - Cov(d_2, r_2). \end{aligned} \quad (5.16)$$

Table 5.2: Results summary of the reflection component path loss when a single reflector is considered for various half-power angles $\Psi_{1/2}$.

Time	half-power angle $\Psi_{1/2}$ value (degree)	Theoretical (μ_q, σ_q)	Simulation (μ_q, σ_q)
0:00-3:00	20	(-147.2, 2.17)	(-147.2, 2.17)
	30	(-150.4, 2.17)	(-150.4, 2.17)
	60	(-155.0, 2.17)	(-155.0, 2.17)
12:00-15:00	20	(-111.7, 2.13)	(-111.7, 2.13)
	30	(-114.8, 2.14)	(-114.8, 2.14)
	60	(-119.4, 2.15)	(-119.4, 2.15)

$Cov(d_1, r_1)$ and $Cov(d_2, r_2)$ are the covariances, which are given by:

$$Cov(d_1, r_1) = 100Corr(d_1, r_1)(m^2 + (\zeta + 1)m) \frac{\sigma_s \sigma_r}{(\ln(10))^2}. \quad (5.17)$$

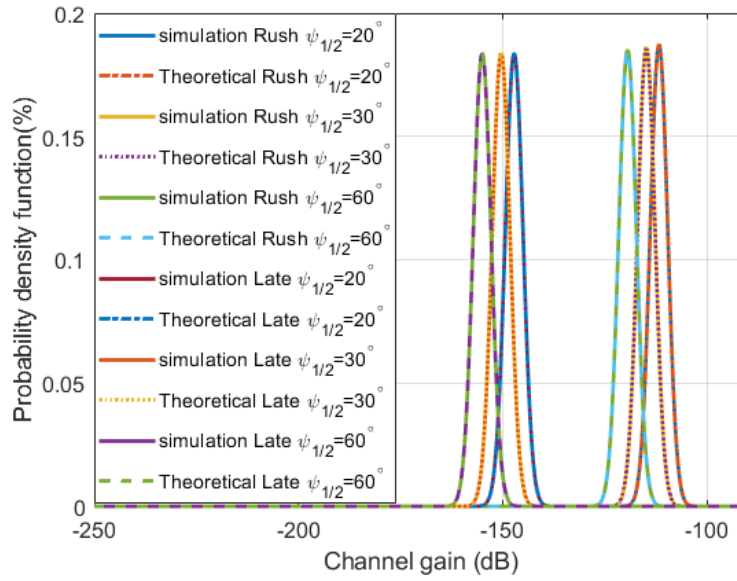
$$Cov(d_2, r_2) = 400Corr(d_2, r_2) \frac{\sigma_s \sigma_r}{(\ln(10))^2}. \quad (5.18)$$

$Corr(d_1, r_1)$ and $Corr(d_2, r_2)$ are the correlation coefficients.

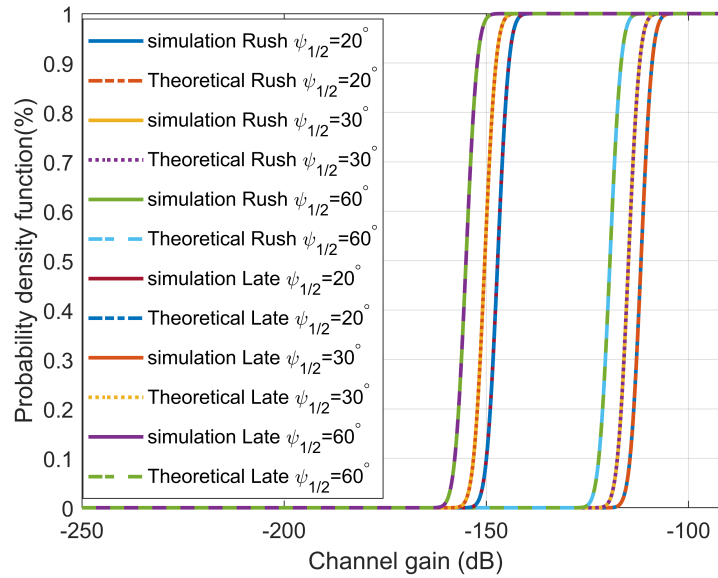
and the mean is given by:

$$\begin{aligned} \mu_q = 10 \log \frac{\rho A_r (m+1) f^2}{(2\pi)^2} + \left(10m \frac{\mu_s}{\ln(10)} \right) \\ + \left(10 \frac{\mu_s}{\ln(10)} \right) + \left(10(m + \zeta + 1) \frac{\mu_r}{\ln(10)} \right) + \left(40 \frac{\mu_r}{\ln(10)} \right). \end{aligned} \quad (5.19)$$

Figure 5.3 depicts statistical and simulated PDFs and CDFs of the NLOS component of V2V-VLC path loss when the inter-vehicle spacing D has a log-normal distribution with parameters given in Table 3.4 for different half-power angle $\Psi_{1/2}$ values. The standard deviation and mean values are summarised in Table 5.2 for different half-power angle $\Psi_{1/2}$ values. The figure and table show that path loss distribution, standard deviation and mean values obtained using MC simulation for a Lambertian source ($\zeta = 2$) matches with the theoretical analysis given by (5.15, 5.16 and 5.19). The Kolmogorov-Smirnov test does not



(a)



(b)

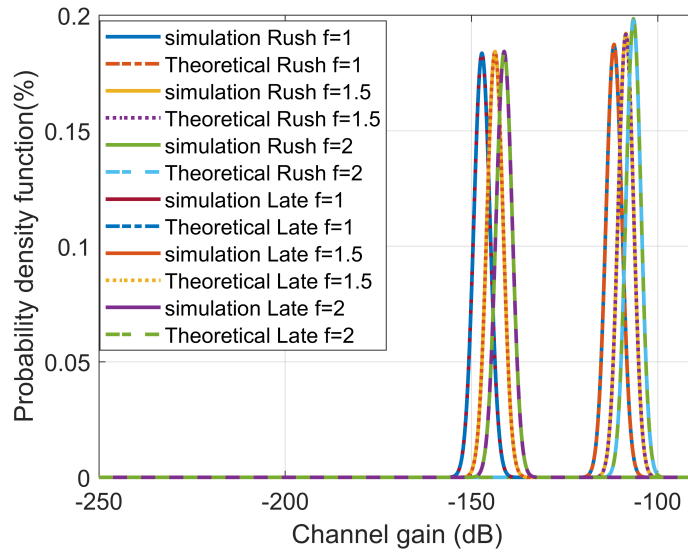
Figure 5.3: The a) PDFs and b) CDFs of NLOS component of V2V-VLC path loss for a Lambertian source when a single reflector is considered and the inter-vehicle spacing D has a log-normal distribution for various half-power angles $\Psi_{1/2}$ for the time intervals 00:00-03:00 and 12:00-15:00.

Table 5.3: Results summary of the reflection component path loss when a single reflector is considered for three different values of f 2 m, 1.5 m.

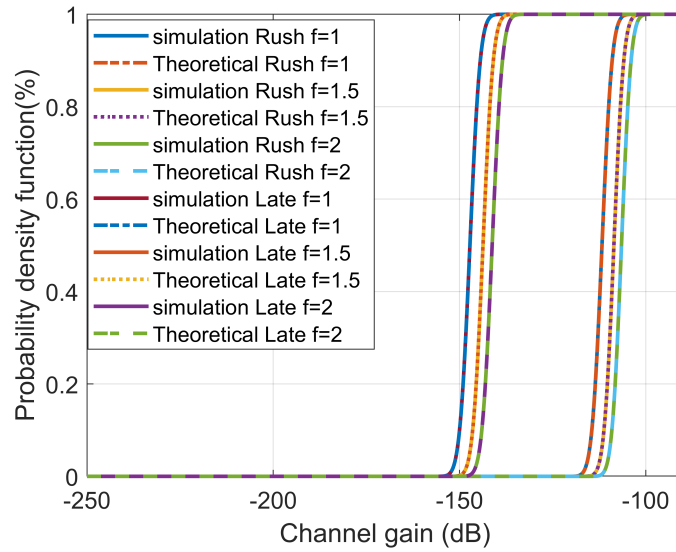
Time	Lateral inter-vehicular deviation f (m)	Theoretical (μ_q, σ_q)	Simulation (μ_q, σ_q)
0:00-3:00	1	(-147.2, 2.17)	(-147.2, 2.17)
	1.5	(-143.7, 2.17)	(-143.7, 2.17)
	2	(-141.2, 2.17)	(-141.2, 2.17)
12:00-15:00	1	(-111.7, 2.13)	(-111.7, 2.13)
	1.5	(-108.6, 2.08)	(-108.6, 2.08)
	2	(-106.5, 2.01)	(-106.5, 2.01)

reject the null hypothesis at the 1% significance level. In addition, the figure and table showed that the mean path loss increases with the increases in $\Psi_{1/2}$ while the standard deviation values change insignificantly. This is expected in (5.16) because the effect of $\Psi_{1/2}$, which is represented by m , is reduced by $Cov(d_1, r_1)$.

Figure 5.4 examines the effect of quantized lateral inter-vehicle spacing f . The figure depicts the statistical and simulated PDFs and CDFs of NLOS V2V-VLC path loss when the inter-vehicle spacing D has a log-normal distribution with parameters provided in Table 3.4 for $f = 2$ m, $f = 1.5$ m and $f = 1$ m. The figure shows that the path loss distribution obtained using MC simulation for a Lambertian source matches perfectly with the theoretical analysis given by (5.15) and the Kolmogorov-Smirnov test does not reject the null hypothesis at the 1% significance level. The standard deviation values σ_q and the mean path loss values μ_q are summarized in Table 5.3. The table shows that distribution parameters match the theoretical analysis given in (5.16-5.19), respectively. Insignificant changes of standard deviation values are observed at relatively larger inter-vehicle spacing values (e.g. late night hours) because the $Cov(d_1, r_1)$ and $Cov(d_2, r_2)$ effect becomes negligible. However, at rush hours the inter-vehicle spacing values become comparable to the lateral inter-vehicle spacing values, hence the $Cov(d_1, r_1)$ and $Cov(d_2, r_2)$ effect increase as expected in (5.16). The mean



(a)



(b)

Figure 5.4: The a) PDF and b) CDF of NLOS component of the V2V-VLC path loss for Lambertian source when a single reflector is considered and the inter-vehicle spacing D has a log-normal distribution for three different values of f 2 m, 1.5 m and 1 m, respectively, for the time intervals 00:00-03:00 and 12:00-15:00.

path loss μ_q decreases with the increase in f as expected in (5.18).

Figure 5.5 illustrates the statistical and simulated PDFs and CDFs of NLOS V2V-VLC path loss using the piecewise Lambertian model (ζ values given in Table 4.2) when D has a log-normal distribution with parameters given in Table 3.4. The figure shows that NLOS V2V-VLC is independent on the irradiance angle ϕ and it matches normal distribution with a mean value of -85.6 dB and standard deviation of 1.8. The results show that the asymmetrical radiation pattern of the vehicle's source has a marginal effect on the NLOS path loss distribution. However, it affects the mean and the standard deviation values of the distribution.

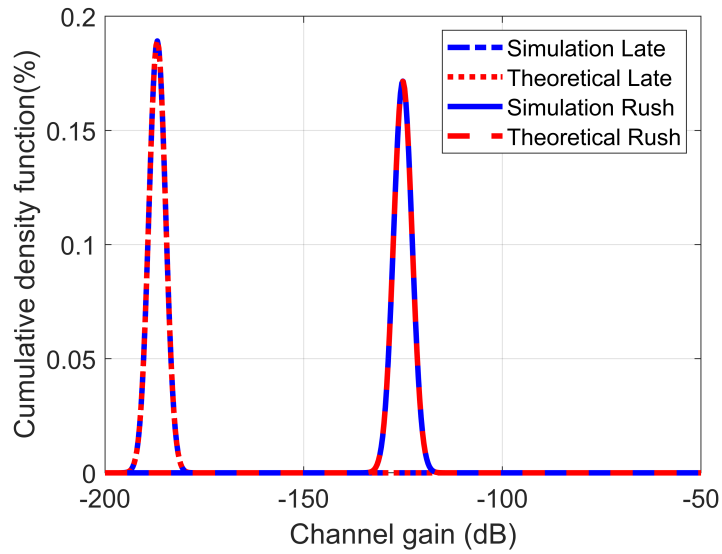
The path loss value is high for the single reflector scenario. This indicates that V2V-VLC cannot be supported by the NLOS component if the LOS link is blocked. At low-density traffic, the LOS link is less likely to be blocked and at high-density traffic, the possibilities of multiple reflectors increase. Therefore, in the following section, a statistical model of NLOS path loss is established for multiple reflectors scenario.

5.3.2 Multiple reflectors scenario

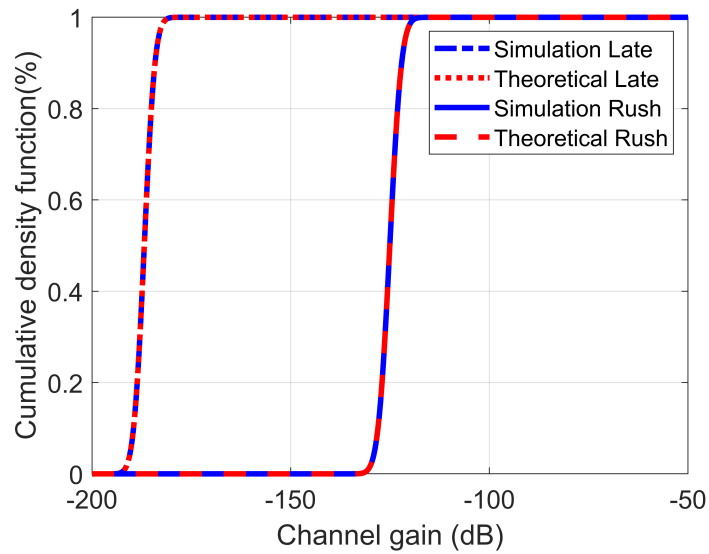
The distribution of multiple reflectors is given as the sum of the distributions of a single reflector given in (5.8). The path loss (in dB) has a normal distribution given in (5.15). Therefore, the DC channel gain distribution in (5.7) is given as $10^{P_{L,dB}/10}$. Consequently, the DC channel gain has log-normal distribution with $\mu_i = \mu_q (\ln 10)/10$ and $\sigma_i = \sigma_q (\ln 10)/10$ (Papoulis et al., 2002; Schwartz and Yeh, 1982). Schwartz and Yeh (1982) shows that the sum of random variables with log-normal distribution has a log-normal distribution with approximate mean value μ_j and standard deviation σ_j that can be calculated using different methods, such as Wilkinson, Fray or Schwartz-Yeh methods. Hence, the distribution of multiple reflectors in (5.2) is given by log-normal distribution (Schwartz and Yeh, 1982):

$$P_{LNLOS}(x; \mu_j, \sigma_j) = \frac{1}{x\sigma_j\sqrt{2\pi}} \exp\left\{\left(-\frac{(\ln x - \mu_j)^2}{2\sigma_j^2}\right)\right\}, \quad (5.20)$$

and the path loss (in dB) is given by normal distribution (Schwartz and Yeh, 1982):



(a)



(b)

Figure 5.5: The a) PDF and b) CDF of NLOS V2V-VLC path loss using the piecewise Lambertian model when the inter-vehicle spacing D has a log-normal distribution and $f=1$ m for the time intervals 00:00-03:00 and 12:00-15:00.

$$P_{LNLOS[dB]}(x; \mu_j, \sigma_j) = \frac{1}{x\sigma_j\sqrt{2\pi}} \exp\left\{-\frac{(x - \mu_j)^2}{2\sigma_j^2}\right\}. \quad (5.21)$$

The path loss of **NLOS V2V-VLC** channel of four reflectors vehicles, i.e. $J_r = 4$, when the inter-vehicle spacing D has a log-normal distribution with parameters given in Table 3.4, is given in Figure 5.6. The figure shows that the gain of multiple reflections increases to -56.9 dB and -70.4 dB at high and low-density traffic scenarios, respectively. Hence, **V2V-VLC** can be supported relying on the **NLOS** component when multiple reflectors are presented.

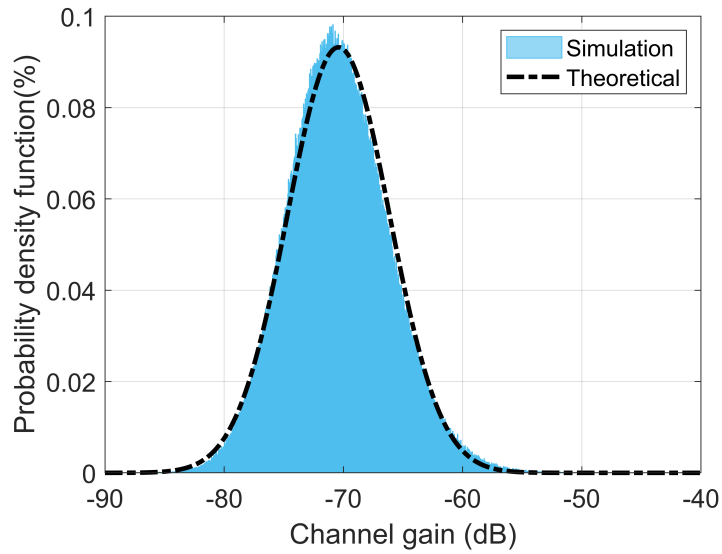
Having studied the statistical path loss model of the **V2V-VLC** multipath channel, the following section investigates the temporal properties of the channel.

5.4 Temporal properties of V2V-VLC channel

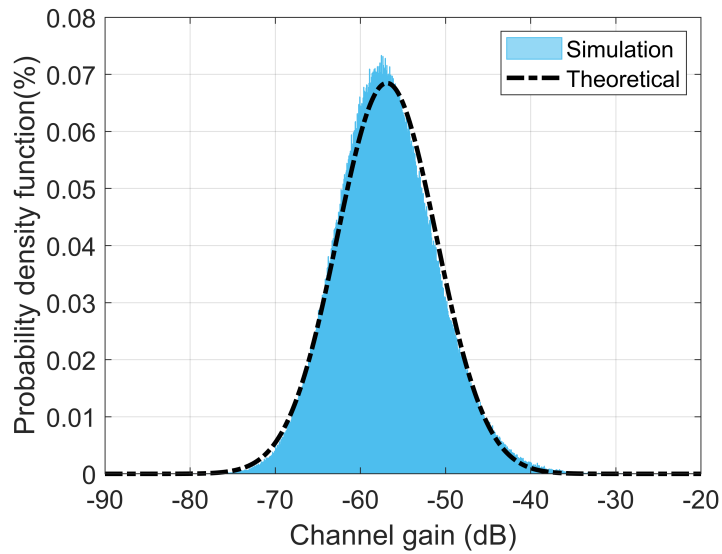
The vehicular communication system has a dynamic nature as the transmitters, receivers and reflectors move with an unpredictable movement pattern. Furthermore, the number and locations of reflectors also changes continuously. In such systems, the characteristics of multipath vary with time and hence a statistical model must be used to study the system (Goldsmith Andrea, 2005, P. 33). As explained in section 2.2.2.3, the optical signal arrives at the receiver through multiple paths with different path lengths. Therefore, it experiences delays of different duration, with each delay duration proportional to the propagation path length (Al-Kinani, Wang, Zhou and Zhang, 2018). As a result, the received signal is a time dispersed copy of the transmitted signal.

5.4.1 Two-dimensional CIR

The **CIR** in **V2V-VLC** systems is expressed as a two-dimensional process given in (2.8) with parameters depending on the time-varying traffic conditions. This process depends on the dynamic inter-vehicle spacing $D(t)$ which has a log-normal distribution with parameters given in Table 3.4. The **MC** simulation of 10^6 iterations is considered to study the temporal properties of the **V2V-VLC** channel when the inter-vehicle lateral distance is 1 m. A **PD**



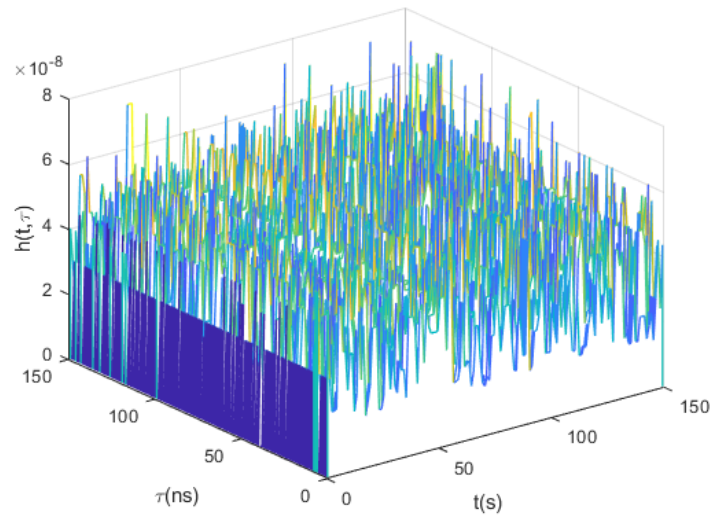
(a)



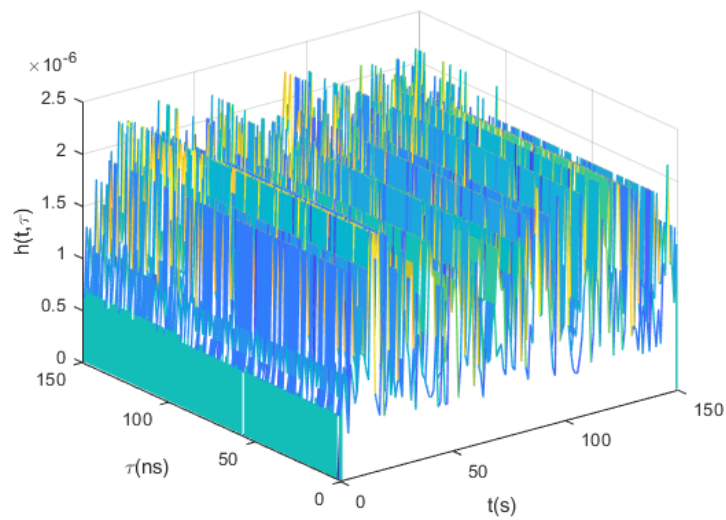
(b)

Figure 5.6: Multiple reflection path loss distribution of four reflectors vehicles, at a) 00:00-03:00 and b) 12:00-15:00.

receiver with an active area of 1 cm^2 and FOV of 80° is assumed (Al-Kinani, Sun, Wang, Zhang, Ge and Haas, 2018).



(a)



(b)

Figure 5.7: The two-dimensional CIR of the V2V-VLC channel when the inter-vehicle spacing has a log-normal distribution at a) 00:00-03:00 and b) 12:00-15:00.

The two-dimensional V2V-VLC CIR for the time intervals 00:00-03:00 and 12:00-15:00 is shown in Figure 5.7. It is observed that the amplitude of CIR between 12:00 and 15:00 is two orders of magnitude higher than the amplitude of CIR between 00:00 and 03:00. This is because the NLOS signals propagate shorter distances at rush hours as given in Table 3.4. The values of the propagation delay of the NLOS components are in the nanoseconds range for both rush and late hours.

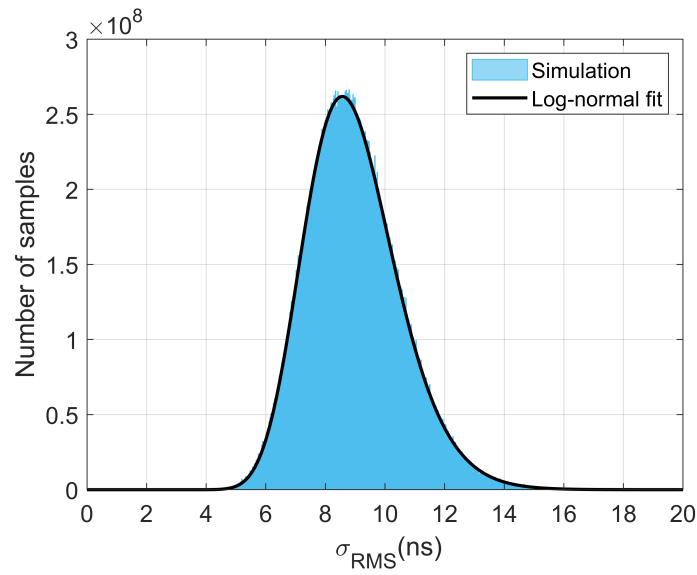
5.4.2 RMS delay spread

RMS delay spread is a time dispersion parameter used to find channel coherence bandwidth and describe the fading behaviour of the channel, as explained in section 2.2.2.3. Figure 5.8 shows the RMS delay spread σ_{rms} of the V2V-VLC channel at the rush and late hours. The figure shows that σ_{rms} fits a log-normal distribution with mean values summarised in Table 5.4. The figure and table show that the delay spread σ_{rms} at rush hours has a higher value when traffic density is high, because the number of NLOS component taps are higher. Hence, the time dispersion increases with the increasing number of reflection taps as shown in Figure 2.8. The obtained RMS delay spread values at rush hours are comparable to the values obtained by ray-tracing in (Lee et al., 2012b) in the metropolitan street scenario as given in Table 5.4. A ray-tracing study in (Eldeeb et al., 2021) showed that the RMS delay spread σ_{rms} has lower values at a longer distance due to small FOV, which limits NLOS component reception. At different traffic density, the obtained RMS delay spread values of the V2V-VLC channel are in nanoseconds.

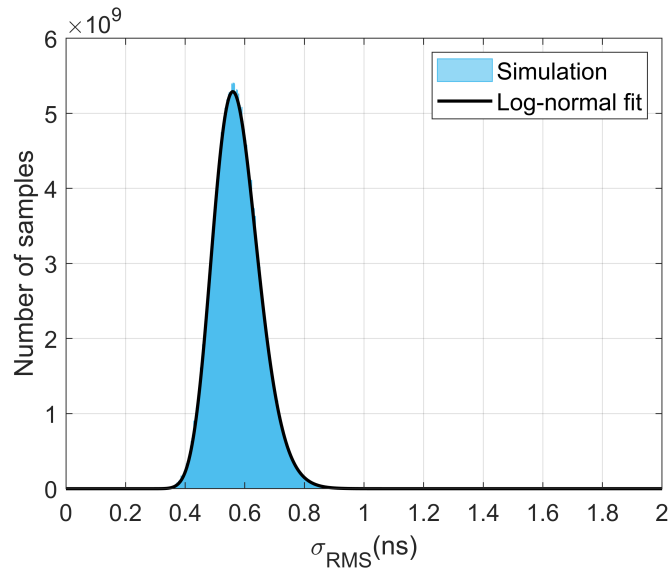
The figure and table show that the V2V-VLC channel has flat fading characteristics for any data transmission with a rate below 1 Gbps because the symbol time duration is larger than the RMS delay spread.

5.4.3 Two-dimensional autocorrelation function

The two-dimensional autocorrelation function in (2.23) indicates the time stationarity properties and coherence time of the channel as explained in Section 2.2.2.3. The autocorrelation



(a)



(b)

Figure 5.8: The RMS delay spread σ_{rms} of the V2V-VLC channel for a) high-density traffic and b) low-density traffic.

functions and coherence time of the V2V-VLC channel at late and rush hours are shown in Figure 5.9. The figure shows that the V2V-VLC channel decorrelates with time, as the

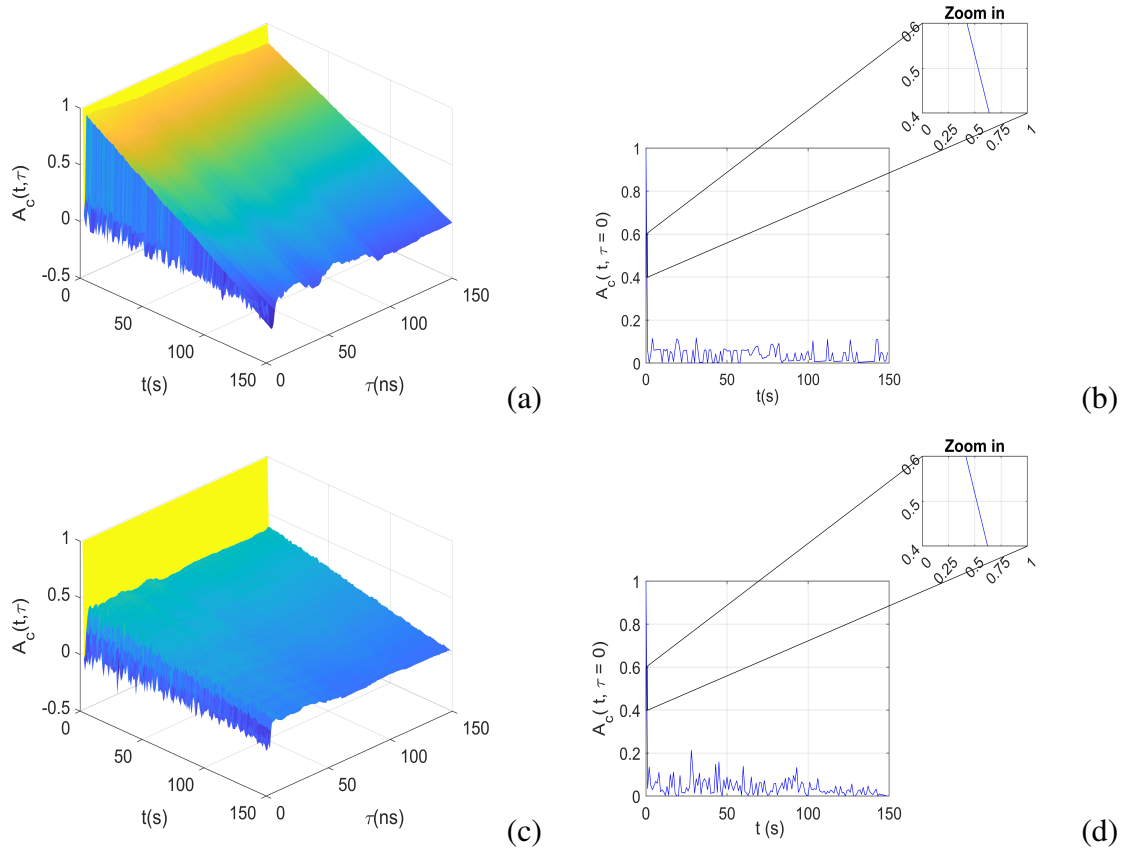


Figure 5.9: The autocorrelation functions and coherence time of V2V-VLC channel at 00:00-03:00 (a and b) and 12:00-15:00 (c and d), respectively.

Table 5.4: Values of the RMS delay spread σ_{rms} of V2V-VLC channel at rush and late hours compared to previous works.

Time	Mean distance (m)	σ_{rms} (ns)
0:00-3:00	48.72	0.57
12:00-15:00	12.37	8.9
Al-Kinani et al. (2018)	70	0.5-0.6
Lee et al. (2012b)	Metropolitan street scenario	5-30
Eldeeb et al. (2021)	40-50	0.1

Table 5.5: Values of the 50% coherence time for different inter-vehicle spacing distributions.

Time	Mean distance (m)	50% coherence time (s)
0:00-3:00	48.72	0.53
12:00-15:00	12.37	0.52
Cui et al. (2014)	Urban area of Taipei	0.53
Chen et al. (2016)	Freeway	2.656
	Suburban	0.164

autocorrelation function of the channel decreases over the delay τ as the transmission time increases. This means that the autocorrelation function is time-dependent, and hence, the V2V-VLC channel has time-variant non-stationary behaviour.

Figure 5.9 (b and d) show the 50% coherence time values of the V2V-VLC channel at late and rush hours. Table 5.5 summarises the 50% coherence time values for different inter-vehicle spacing distributions. The table shows that the obtained coherence time value falls within the range that was measured by [Cui et al. \(2014\)](#) and it is close to the empirical value that was determined by [Chen et al. \(2016\)](#). In general, the values of coherence time shows that the V2V-VLC channel is considered a slow fading channel for any data transmission with a rate below 1 Gbps.

5.5 Summary

The impact of dynamic traffic on path loss and the temporal properties of multipath V2V-VLC systems was investigated. V2V-VLC channel path loss due to reflection from different surfaces was examined. The results showed that the channel path loss due to reflection from surrounding vehicles is at least 10 dB lower than its values due to reflection from other surfaces.

A statistical distribution of the NLOS V2V-VLC channel path loss was established. The results showed that the NLOS V2V-VLC channel path loss follows a normal distribution with a mean value that increases with the increase number of reflectors. The results also showed that the asymmetrical radiation pattern of the vehicle's source has a marginal effect on the NLOS path loss distribution. However, it affects the mean and the standard deviation values of the distribution.

The temporal properties of the V2V-VLC channel under different traffic conditions showed that the V2V-VLC channel is time-variant non-stationary with flat and slow fading behaviour.

The results showed that the surrounding vehicles are the main cause of reflection and hence, multipath propagation. However, the number of surrounding vehicles is variable and depends on traffic conditions. Therefore, in the following Chapter 6, a novel measure to quantify the co-existence of other vehicles in the adjacent lanes is proposed based on traffic measurements from two motorways in the UK. In addition, the impact of multipath propagation on the BER and associate SNR performance is examined.

Chapter 6

Performance of Vehicle-to-Vehicle Visible Light Communications Channel

Chapter 4 and Chapter 5 established a statistical model to describe the channel gain for the LOS and NLOS components of the V2V-VLC channel under different traffic condition. This chapter uses these statistical models to investigate the BER performance in the presence of surrounding vehicles, which introduce multiple reflections as well as increase ambient noise due to the light sources.

Due to the dynamic changes in the traffic conditions, the presence of surrounding vehicles varies with the traffic flow, which changes during the day. As a result, the likelihood of reflection and interference level change with the traffic conditions. Therefore, evaluating the co-existence of other vehicles in the adjacent lanes is important to evaluate the performance of V2V communication systems regardless of the transmission technologies.

This chapter estimates the probability of co-existence of other vehicles in the adjacent lanes using real-time traffic measurements. To quantify the effect of other vehicles in the adjacent lanes on V2V-VLC performance, the SNR and BER are examined on different lanes for different traffic conditions.

The remainder of this chapter is organised as follows: the related works which studied the BER performance and the impact of interference from natural and artificial light sources

on **VVLC** systems are discussed in Section 6.1. The probability of co-existence of other vehicles in the adjacent lanes is provided in Section 6.2. The **BER** performance analysis of the **V2V-VLC** systems is given in Section 6.3.

6.1 Related works

The **SNR** and **BER** are important performance metric indicator for digital communication systems. As explained in Section 2.2.2.4, the relationship between the **SNR** and **BER** depends on the employed modulation scheme. The received signal and noise power are affected by the presence of surrounding vehicles, as shown in Figure 6.1. The signal power increases due to reflection from surrounding vehicles as shown in Chapter 5, while the noise power increases due to interference from light sources of these vehicles. The following sections discuss the previous works that studied the **BER** performance of different modulation schemes and the impact of interference on the **VVLC** channel.

6.1.1 Vehicle-to-vehicle visible light communication performance

The relation between the received signal strength to the channel disturbances such as additive noise and interference, e.g. **SNR** and **signal-to-interference-noise ratio (SINR)** are crucial to establish the performance of **VVLC** systems measured by achievable transmission rate, outage probability and channel capacity (Rahaim and Little, 2017). Table 6.1 provides a summary of the achieved performance of **V2V-VLC** systems in the literature.

Luo, Ghassemlooy, Minh, Bentley, Burton and Tang (2015) predicted the **SNR** and the associate **BER** performance for a **VVLC** system that used a tungsten-halogen lamp and **OOK** modulation scheme, taking into account the effects of reflection from the road surface. The study examined the **BER** performance when the receiver is mounted at 0.2 m, 0.4 m, 0.6 m and 0.8 m. The **BER** is higher for wet roads compared to dry roads and, consequently, a longer transmission distance can be achieved. For a wet road, when the receiver is mounted at a lower height (i.e. less than 0.2 m), a data rate of 50 Mbps is achieved at a transmission

This item has been removed due to 3rd Party Copyright. The unabridged version of the thesis can be viewed at the Lanchester Library, Coventry University.

Figure 6.1: *A realistic scenario with the presence of surrounding vehicles that introduces multiple reflectors as well as the increased ambient noise due to the light sources (Syed, 2014).*

distance of 70 m. Luo, Ghassemlooy, Minh, Bentley, Burton and Tang extended the study to consider the performance of the MIMO system in (Luo, Ghassemlooy, Bentley, Burton and Tang, 2015). A data rate of 4 Mbps was achieved at a distance of 40 m when the receiver is mounted at a height between 0.2 m to 0.4 m.

Căilean et al. (2016); Căilean et al. (2020) proposed an SNR-adaptive VVLC receiver that can estimate the received SNR and adjusts the gain of the receiver accordingly. The proposed automatic gain control (AGC) technique considered the expected variation in the received signal due to vehicles movement and inter-vehicle spacing variation. Căilean et al. (2020) used OOK modulation and Manchester coding. A notable enhancement in the BER performance was achieved by applying the AGC technique. Likewise, Avătămăniței, Căilean, Done, Dimian and Prelipceanu (2020) proposed an adaptive reception technique to overcome

Table 6.1: Summary of the performance of VVLC systems reported in the literature.

Ref.	Modulation scheme	Target BER	Achievable data rate (Mbps)	Achievable link distance(m)
Luo et al. (2015)	OOK	-	50	70
Shen and Tsai (2017)	OFDM & BPSK	-	-	35-45
Elamassie et al. (2018)	MPAM	10^{-6}	-	72 (clear) 26 (fog)
Béchadergue et al. (2019)	OFDM	-	0.002	35
	OOK	-	0.01-0.1	30
Eldeeb et al. (2019)	MPAM	10^{-6}	10	30 (clear) 19.5 (fog)
Zaki et al. (2019)	OOK,	10^{-6}	10	173
	SC-BPSK,	10^{-6}	10	123
	M-PPM	10^{-6}	10	237
	I-MPPM	10^{-6}	10	156
Karbalayghareh et al. (2019)	OOK	10^{-6}	-	180.7 (clear) 66.7 (fog)
Avătămăniței et al. (2020)	OOK	10^{-6}	-	50
Karbalayghareh et al. (2020)	OOK	10^{-6}	-	77.64

ambient noise. The authors examined the BER performance in the presence of high optical interference due to direct sunlight. The study showed that a BER of 10^{-6} can be achieved at a transmission distance of 50 m in sunny conditions.

Shen and Tsai (2017); Béchadergue et al. (2019) conducted an experimental study to examine the error performance of a VVLC system using LED taillight and photodiode supported by WiFi V2V and LIDAR (see Figure 6.2). Shen and Tsai (2017) used 16-

This item has been removed due to 3rd Party Copyright. The unabridged version of the thesis can be viewed at the Lanchester Library, Coventry University.

Figure 6.2: *System setup of Shen and Tsai (2017); Béchadergue et al. (2019) experiment.*

subcarrier **orthogonal-frequency-division-multiplexing (OFDM)** transmission scheme with a BPSK modulation for each subcarrier. Considering the high noise at the edge carriers, only 14-subcarriers were used for transmission. Four subcarriers were used as pilot symbols and 10-subcarriers were used to transmit data. The study showed that a **symbol reception rate (SRR)** of 90% can be achieved within a transmission distance of 35 m. The achievable **SRR** decays significantly when the transmission distance increased to 45 m. The study showed a trade-off between the achievable transmission distance and data rate. In addition, the study showed that the **SRR** decreases when the incidence angle increases due to the radiation pattern of the light source. As a result, **Shen and Tsai (2017)** concluded that the geometry of the **VVLC** link presented by the transmission distance and angles is the main factor that influences the received power. **Béchadergue et al. (2019)** compared the spatial performance of **OFDM** and **OOK**. The results revealed that **OFDM** is resilient to interference, while **OOK** undergoes a transmission outage due to interference. However, **OFDM** provides larger spatial coverage at the expense of one order of magnitude lower data rate.

Elamassie et al. (2018); Eldeeb et al. (2019) derived the achievable transmission distance formula for **M-ary pulse amplitude modulation (MPAM)** scheme considering different weather conditions. To ensure an acceptable reception with a **BER** of 10^{-6} , Elamassie et al. (2018) showed that the maximum achievable distance is 72 m under clear weather conditions. The maximum achievable distance decreases to 26 m in foggy condition. Elamassie et al. (2018); Eldeeb et al. (2019) showed that using higher-order **pulse amplitude modulation (PAM)** increases the data rate at the expense of reducing the achievable transmission distance. Similarly, Karbalayghareh et al. (2019) derived the achievable transmission distance formula for the **OOK** modulation scheme considering different weather conditions. Karbalayghareh et al. showed that when a **SPAD** receiver is used, the maximum achievable distance values are 180.7 m and 66.7 m at **BER** = 10^{-6} with a transmit optical power of 20 dBm for clear and foggy conditions, respectively. Karbalayghareh et al. (2020) considered different receiver aperture sizes. The maximum achievable distance was 77.64 m at **BER** = 10^{-6} when a **SPAD** receiver with an aperture size of 15 cm was used. Eldeeb, Elamassie and Uysal (2020) used the Shannon formula to describe the capacity of the **V2I** channel. The study showed that a channel capacity of 54 Mbps can be achieved at a distance of 30 m when a **PD** receiver is aligned with the green light of a traffic light. Channel capacity decays to 21 Mbps if the **PD** receiver is mounted in alignment with the red light of a traffic light.

Zaki et al. (2019) investigated the performance of different modulation techniques, including **M-ary pulse position modulation (MPPM)**, **inverted-MPPM (I-MPPM)**, **OOK**, **sub-carrier-BPSK (SC-BPSK)** under different weather conditions. The study identified the required **SNR** values for each modulation and the achievable transmission distance associated with the target **BER**. The study concluded that **MPPM** offers optimal performance.

The capacity bounds of **VVLC** that considers power constraints have not been reported in the literature. Particularly, **VVLC** channel capacity associated with an unpredictable movement pattern of vehicles requires further investigation.

This item has been removed due to 3rd Party Copyright. The unabridged version of the thesis can be viewed at the Lanchester Library, Coventry University.

Figure 6.3: *A photograph of a realistic driving scenario in presence of the sunlight (Pxhere.com, 2017).*

6.1.2 Impact of interference

Interference from other light sources induces additional noises. Therefore, there has been extensive research activities to examine the feasibility of VLC links in outdoor environments in the presence of natural and artificial light sources. The following subsections provide an overview of the previous studies which considered the impact of interference from natural and artificial light sources on outdoor VLC and particularly VVLC systems.

6.1.2.1 Interference from natural light sources

The main source of ambient noise in VVLC systems is the sunlight, which introduces shot noise at the optical receiver. Figure 6.3 shows a photograph of a realistic driving scenario in presence of sunlight. The sunlight noise is limited to daytime. Solar irradiance changes during the day, months, seasons and depends on geographical location (Islim and Haas, 2017).

The interference impact due to natural light sources was studied by several researchers. [Lee et al. \(2009\)](#) investigated the impact of the ambient noise due to sunlight on V2I system performance during different times of the day. The proposed selective combining receiver technique reduced the impact of ambient noise by 5 dB. In addition, a 20 dB variation in the background noise power was observed between the minimum recorded values in the early morning and peak values at midday.

[Liu et al. \(2011\)](#) performed an experimental study to investigate the impact of solar interference on the PDR of a VVLC system for different azimuth and vertical angles of the sun. The study showed that 100% PDR could be achieved for a transmission distance of less than 101 m when a receiver with 12° FOV is used in a dominant diurnal noise scenario. Similarly, [Chung and Oh \(2013\)](#) proposed an optical filter to block the ambient noise. The proposed technique blocked noise with an angle greater than 30°. [Islim and Haas \(2017\)](#) studied the impact of solar irradiance on the data rate and BER performance of outdoor VLC system under the worst-case scenario. The authors investigated the impact of sunlight on SNR, data rate and BER performance of VVLC systems in two different geographical locations; Edinburgh and Antofagasta in the northern and southern hemispheres, respectively. The results showed that a data rate of 1 Gbps is achieved in the presence of sunlight.

[Kim and Chung \(2015\)](#) carried out an experimental study to examine the performance of a proposed differential decision threshold receiver with optical and colour filters method to reduce the ambient noise. The measurements were carried out under direct sunlight in an outdoor environment at different times of the day from 10:00 to 16:00. The proposed method enhanced the reception of the communication link. However, the study considered a short transmission distance of 10-20 cm.

[Singh et al. \(2018\)](#) studied the BER performance of VVLC in the presence of sunlight in New Delhi and London in March, June and December. Compared to London, New Delhi has higher BER values during June due to the higher solar irradiance values. Similarly, [Avătmăniței, Căilean, Done, Dimian and Prelipeanu \(2020\)](#) studied the BER performance in the presence of high optical interference due to direct sunlight. The study showed that a BER of 10^{-6} can be achieved at a transmission distance of 50 m in sunny conditions when an

This item has been removed due to 3rd Party Copyright. The unabridged version of the thesis can be viewed at the Lanchester Library, Coventry University.

Figure 6.4: *VVLC channel path loss as a function of distance and under different illumination conditions (Turan et al., 2018, Figure 5).*

adaptive reception technique is employed.

Turan et al. (2018) considering different illumination, including sun, sunset and night conditions to derive a path loss expression as a function of transmission distance, as illustrated in Figure 6.4. The channel gain values at night were observed to be higher than their values at sunset and sunny time by 0.793 dB and 12.943 dB, respectively. However, the channel path loss and additive noise are independent as given in (2.1) (Ghassemlooy et al., 2019).

Cervinka et al. (2020) investigated the impact of the direct, reflected and diffuse sunlight on VVLC link throughout the year in Coventry, UK. A flashing warning light mounted on top of an emergency service vehicle was considered a transmitter. Considering a binary PAM scheme, the results revealed that a transmission distance of 33 m and 28 m can be achieved for the minimum and maximum solar irradiance, respectively.

6.1.2.2 Interference from artificial light sources

The impact of interference from artificial light sources has been considered by few researchers. Liu et al. (2011) conducted an experiment to examine the impact of interference from the

surrounding vehicle's light sources on the PDR of a VVLC system. The study considered the interference due to halogen and LED-bases light sources. The results showed that 100% PDR could be achieved regardless of the separation between the receiver and the LED-based interferer. However, the PDR decays to 0% when the separation between the receiver and the halogen-based interferer is less than 5 m. Alam and Faruque (2016) carried out an experimental study to investigate the impact of ambient noise due to indoor light sources and sunlight when two solar panels are used as optical receivers. The study proposed a differential optical receiver to mitigate the interference from ambient noise. The results showed that the proposed method reduces the ambient noise from artificial sources and sunlight by 22 dB and 12 dB, respectively.

Khoder et al. (2020) studied the interference from the surrounding vehicles in the other lane in VVLC platoon links. The study showed degradation in the throughput, probability of failure and virtual service time performance at high-density traffic when the rate of arrival of vehicles in the adjacent lanes increases.

Singh et al. (2020) examined the impact of interference from adjacent vehicles on VVLC and RF-based vehicular communications links performance. The study considered the poisson point process (PPP) to model spatially distributed interfering vehicles locations. The results indicated a superior performance of VVLC on RF-based vehicular communications systems under clear weather, while RF-based systems have better performance under severe weather conditions.

Matolcsy and Udvary (2020) proposed a 2×2 differential VLC transmission method to cancel the additive ambient noise. The proposed method showed high noise cancellation efficiency even for high-frequency noise from artificial light sources when the two detectors are equally affected by the same noise level. The efficiency of the proposed method decreases when the noise distribution between the two detectors is imbalanced.

In conclusion, surrounding vehicles sources induce ambient noise that affect the performance of VVLC systems. Different techniques have been proposed to reduce the impact of such noise. However, the probability of co-existence of other vehicles in the adjacent lanes which induce additional noise changes with the variation in traffic flow during the day.

Therefore, the following section estimates the probability of co-existence of other vehicles in the adjacent lanes.

6.2 Probability of co-existence of other vehicles in the adjacent lanes

Figure 6.5 illustrates the reflection and direct light from the surrounding vehicles. Reflection from the surrounding vehicles has a significant effect compared to the reflection from other road surfaces as discussed in Section 5.2. In addition, the direct light from these vehicles increases the shot noise at the receiver. However, due to the dynamic nature of traffic, vehicle density and road occupancy change continuously during the day. As a result, the presence of other vehicles which add interference and act as reflectors changes accordingly. Hence, an indicator to measure the probability of co-existence of other vehicles in the adjacent lanes (L_k) is proposed. It relies on traffic measurements from the M6 and M42 motorways. The probability values are calculated by examining the traffic flow and road occupancy data. These metrics provide vital information about the reflection and interference from nearby vehicles for the vehicular communication systems regardless of the employed transmission technology.

To calculate the probability of co-existence of other vehicles in the k^{th} lane (where $k = 1, 2$ and 3 for left-hand, middle and right-hand lanes, respectively), a logical indicator f_k is defined, which is assigned a logic 1 when the traffic flow ($flow_k$) in the k^{th} lane is larger than one, and 0 otherwise. The event R_ι of having more than two vehicles in any adjacent two lanes at any time instant ι is calculated using Algorithm 1.

In addition, L_k increases with the time duration of other vehicles occupying the adjacent k^{th} lane, which is measured by road occupation percentages O_k . Therefore, the average of the occupation percentages O_k of the other lanes should be taken into account while determining L_k . Hence, L_k is given as a product of the event of having two vehicles in the other two lanes

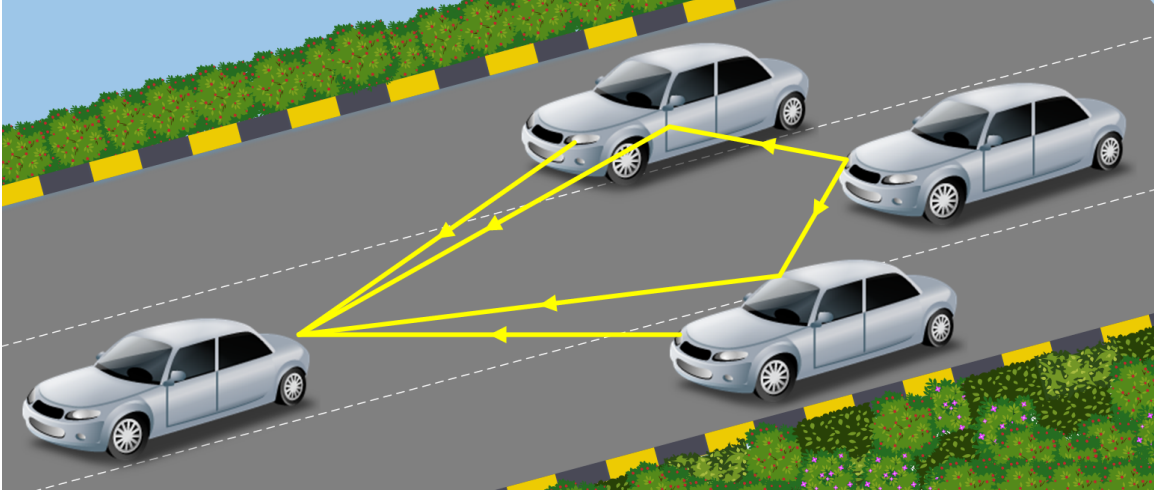


Figure 6.5: Reflection and the direct light from the surrounding vehicles increases the shot noise at the receiver.

R_v and the average of percentages that these vehicles occupy the road, as follows

$$L_3 = R_v \times \left(\frac{O_2 + O_1}{2} \right), \quad (6.1)$$

$$L_2 = R_v \times \left(\frac{O_3 + O_1}{2} \right), \quad (6.2)$$

$$L_1 = R_v \times \left(\frac{O_3 + O_2}{2} \right). \quad (6.3)$$

The distribution of L_k represents the probability of co-existence of other vehicles in the adjacent lanes.

To study the distribution that describes the probability of co-existence of other vehicles in the adjacent lanes L_k during different periods of time, this work first identify sample time windows based on traffic density. Considering variable traffic density during the day, three periods 00:00-06:00, 06:00-20:00 and 20:00-24:00 are used. The time periods 00:00-06:00 and 20:00-24:00 have low-density traffic. The time period 06:00-20:00 has the highest traffic density, as explained in Section 3.2 (see Figure 3.2).

Values of the probability of co-existence of other vehicles in the right-hand (L_3), middle (L_2) and left-hand (L_1) lanes during the low-density traffic at late midnight to early morning hours between 00:00 and 06:00 is shown in Figure 6.6 (a) as a function of time. The figure shows that the values of L_1 , L_2 and L_3 are below 10% between 00:00 and 3:00 on different

Algorithm 1: The event of co-existence of other vehicles in the adjacent lanes at any time instant t .

Result: R_t

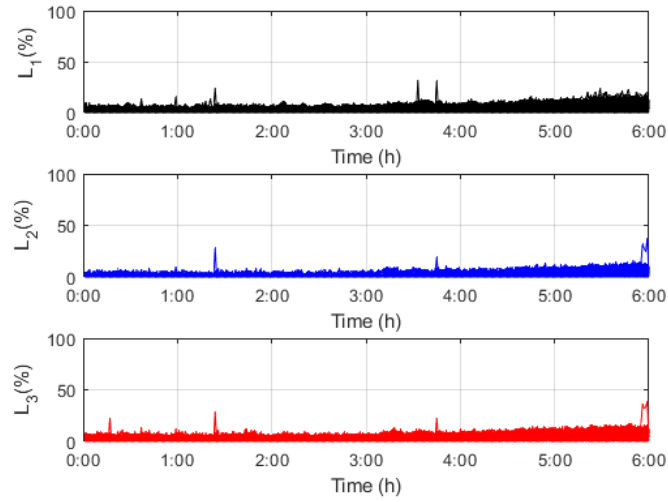
```

while  $i \neq 0$  do
  if  $flow_1 \geq 1$  then
    |  $f_1 = 1$ ;
  else
    |  $f_1 = 0$ ;
  end
  if  $flow_2 \geq 1$  then
    |  $f_2 = 1$ ;
  else
    |  $f_2 = 0$ ;
  end
  if  $flow_3 \geq 1$  then
    |  $f_3 = 1$ ;
  else
    |  $f_3 = 0$ ;
  end
   $R_t = f_3 \bullet f_2 + f_3 \bullet f_1 + f_2 \bullet f_1$ ;
end

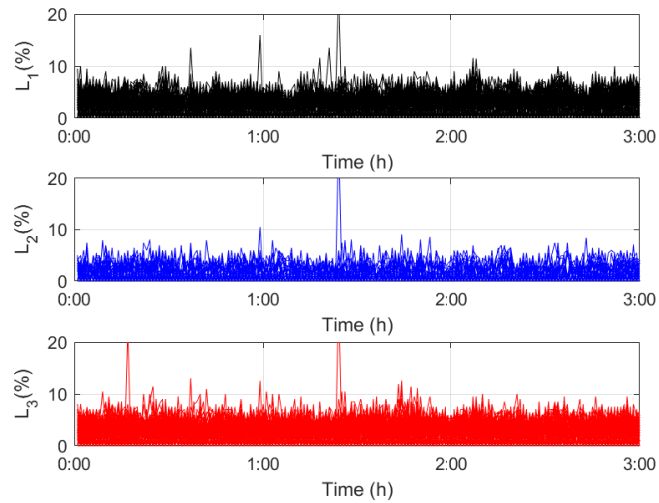
```

lanes. After 03:00 the values start increasing to 20%, as shown in Figure 6.6 (b). Therefore, the time window from 00:00 to 03:00 is used to examine the probability of the co-existence of other vehicles in the adjacent lanes during the off-peak hours.

Values of the probability of co-existence of other vehicles in the right-hand (L_3), middle (L_2) and left-hand (L_1) lanes during the high-density traffic hours (06:00-20:00) as a function of time are depicted in Figure 6.7 (a). The figure shows that after 7:00 hours, the values of L_1 , L_2 and L_3 increase above 60%. The values reach 90% during the peak hours between 16:00 and 19:00, as shown in Figure 6.7 (b). Therefore, the time window (16:00-19:00) is used to study L_k at peak hours.



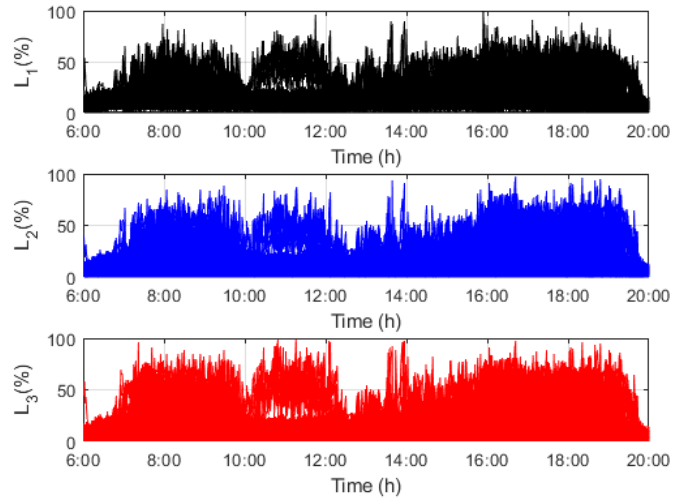
(a)



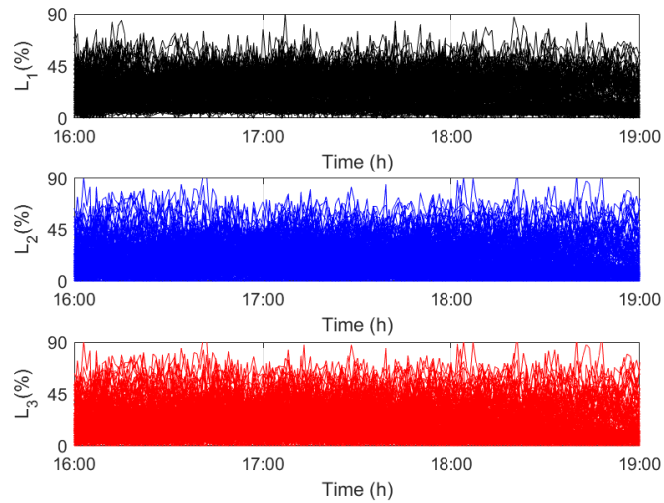
(b)

Figure 6.6: The probability of co-existence of other vehicles in the right-hand (L_3), middle (L_2) and left-hand (L_1) lanes during the off-peak hours at a) 00:00-06:00 and b) 00:00-03:00.

Values of the probability of co-existence of other vehicles in the right-hand (L_3), middle (L_2) and left-hand (L_1) lanes during the low-density traffic night hours (20:00-24:00) are



(a)



(b)

Figure 6.7: The probability of co-existence of other vehicles versus time in the right-hand (L_3), middle (L_2) and left-hand (L_1) lanes during the high-density traffic hours a) 06:00-20:00 and b) 16:00-19:00.

shown in Figure 6.8 as a function of time. The figure shows that between 20:00-22:00 the values of L_1 , L_2 and L_3 are below 10%. An increase in the probability values of less than

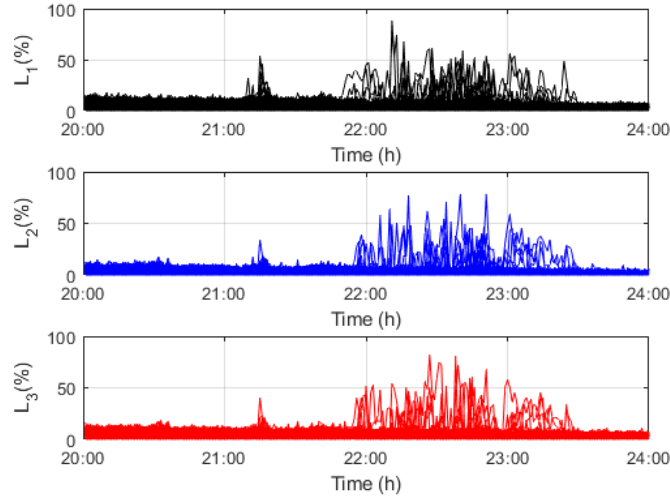


Figure 6.8: The probability of co-existence of other vehicles versus time on the right-hand (L_3), middle (L_2) and left-hand (L_1) lanes during the night hours (20:00-24:00).

60% can be noticed between 22:00 and 23:00. Then the values of L_1 , L_2 and L_3 decrease again to less than 10% after 23:00.

A CDF curve-fitting method is utilized to determine the statistical distribution that best describes the probabilities L_1 , L_2 and L_3 . The curve-fitting is performed with log-normal, Normal, Nakagami and exponential distributions. Table 6.2 provides the parameters and the standard error values of the distributions. The table shows that among the considered distributions, the standard error values of a log-normal distribution are the lowest. Hence, the log-normal distribution provides the closest fit and is given as (Papoulis et al., 2002):

$$P_L(l) = \frac{1}{\delta_l \sqrt{2\pi}} \frac{1}{l} \exp \left\{ \left(- \frac{(\ln(l) - \mu_l)^2}{2\delta_l^2} \right) \right\}. \quad (6.4)$$

The parameters μ_l and δ_l of the distribution are given in Table 6.2. The CDF curves of the probability of co-existence of other vehicles in the right-hand (L_3), middle (L_2) and left-hand (L_1) lanes are shown in Figures 6.9, 6.10 and 6.11 during off-peak hours 00:00-03:00. Similarly, the CDF curves of the probability of co-existence of other vehicles in the right-hand (L_3), middle (L_2) and left-hand (L_1) lanes are shown in Figures 6.12, 6.13 and 6.14 during

Table 6.2: Parameters of different distributions that are expected to describes L_k .

Time	Lane	Distribution	Mean Value (m)	μ_l	μ_l estimation error (%)	δ_l	δ_l estimation error(%)
00:00-03:00	left (1)	log-normal	3.74	1.21	0.41	0.46	0.29
	middle (2)		2.55	0.78	0.98	0.56	0.69
	right (3)		3.61	1.18	0.34	0.45	0.24
	left (1)	Nakagami	3.7	1.56	1.8	16.2	11.67
	middle (2)		2.6	0.94	2.0	8.7	15.7
	right (3)		3.6	1.6	1.6	15.1	9.3
	left (1)	Normal	3.7	3.7	1.4	1.6	1.0
	middle (2)		2.5	2.5	2.6	1.5	1.8
	right (3)		3.6	3.6	1.2	1.5	0.8
	left (1)	Exponential	3.7	3.7	3.3	-	-
	middle (2)		2.5	2.5	4.4	-	-
	right (3)		3.6	3.6	2.8	-	-
16:00-19:00	left-hand (1)	log-normal	19.9	2.71	0.30	0.70	0.25
	middle (2)		16.7	2.44	0.35	0.87	0.20
	right (3)		17.4	2.58	0.45	0.74	0.21
	left (1)	Nakagami	19.3	0.73	0.38	515	262
	middle (2)		15.9	0.58	0.28	380	205
	right (3)		17.8	0.64	0.31	457	235
	left (1)	Normal	18.9	18.9	5.4	12.5	3.8
	middle (2)		15.6	15.6	4.5	11.7	3.9
	right (3)		17.1	17.1	5.2	12.7	3.7
	left (1)	Exponential	18.9	18.9	8.27	-	-
	middle (2)		15.6	15.6	6.4	-	-
	right (3)		17.2	17.2	7.0	-	-

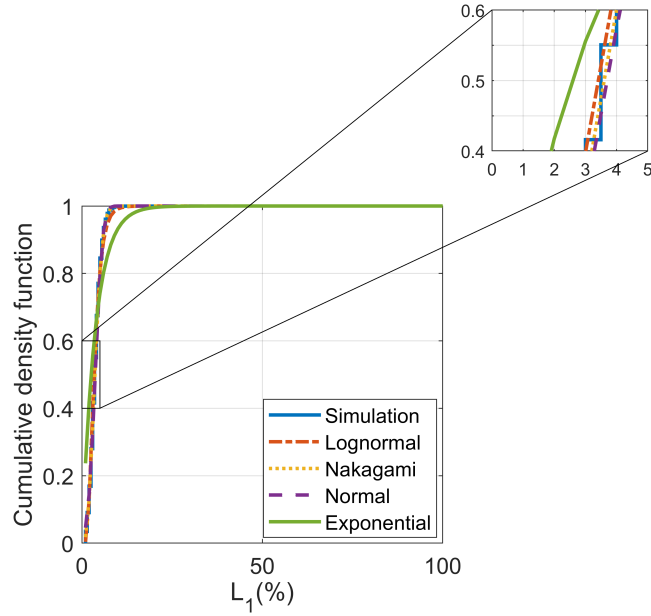


Figure 6.9: *The cumulative density functions of the co-existence of other vehicles in the left-hand lane at 00:00-03:00*

peak hours 16:00-19:00. The figure also shows that a log-normal distribution provides the closest fit and predicts the mean value accurately.

Table 6.2 shows that the mean values of the distributions are comparable for the three lanes during a particular period of time. However, the mean values at off-peak hours differ widely from those at peak hours. The mean values are between 5.12% – 2.55% during the off-peak hours, while they are between 19.9% – 16.7% during the peak hours. This is also illustrated in Figure 6.15.

Considering the probability of the co-existence of other vehicles in the adjacent lanes, the CIR in (2.11) can be re-written as

$$h(t) = h_{LOS}(t) + L_k h_{NLOS}(t). \quad (6.5)$$

As discussed in Section 2.2.2.4, the BER performance in (2.33) when the OOK modulation is considered depends on the V2V-VLC channel. Therefore, the performance of the V2V-VLC channel considering the probability of the co-existence of other vehicles in the adjacent lanes

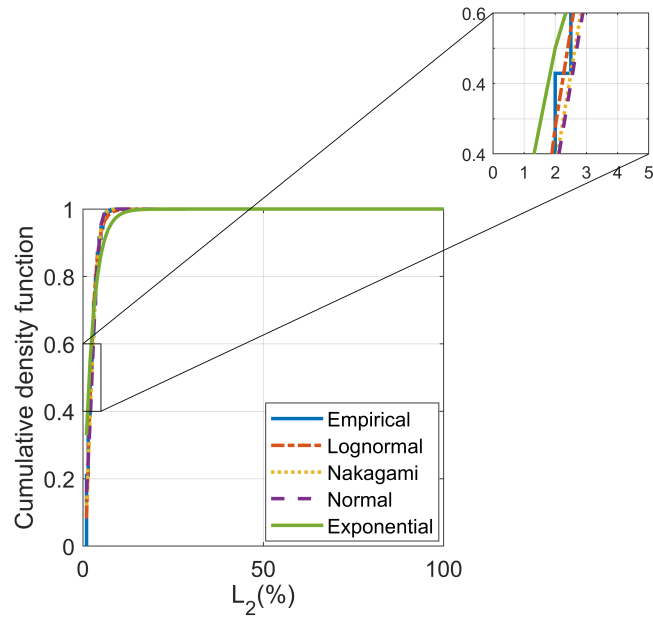


Figure 6.10: The cumulative density functions of the co-existence of other vehicles in the middle lane at 00:00-03:00

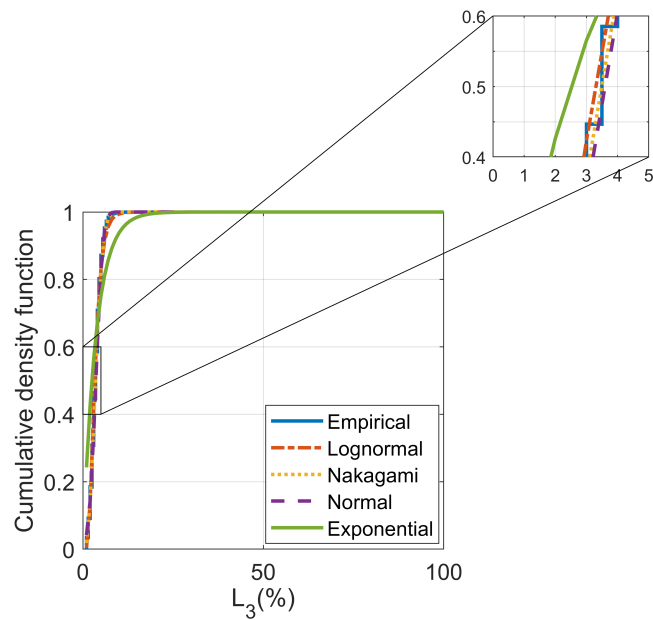


Figure 6.11: The cumulative density functions of the co-existence of other vehicles in the right-hand lane at 00:00-03:00

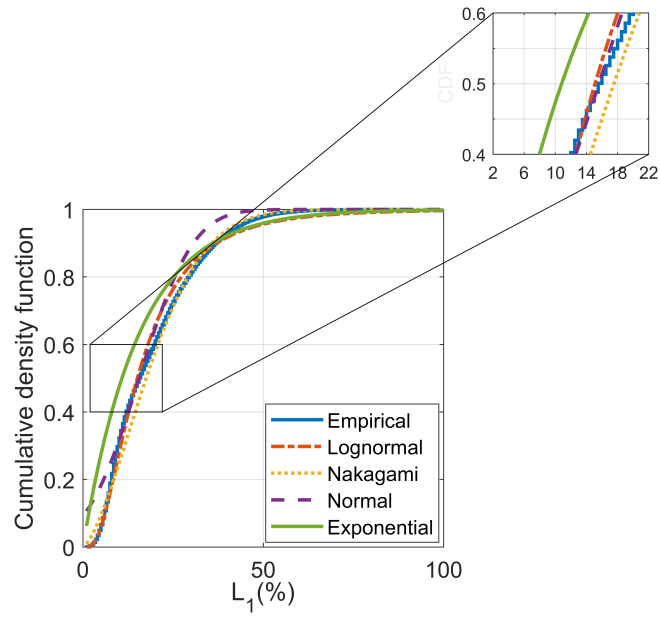


Figure 6.12: The cumulative density functions of the co-existence of other vehicles in the right-hand lane at 16:00-19:00.

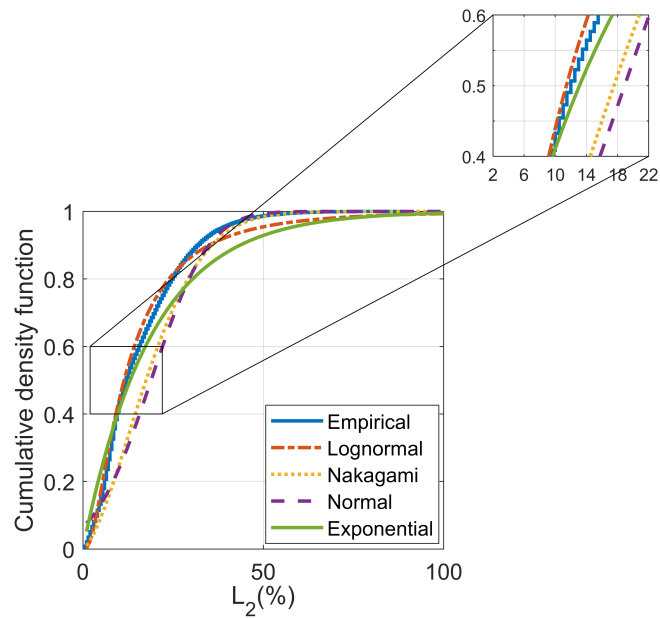


Figure 6.13: The cumulative density functions of the co-existence of other vehicles in the middle lane at 16:00-19:00.

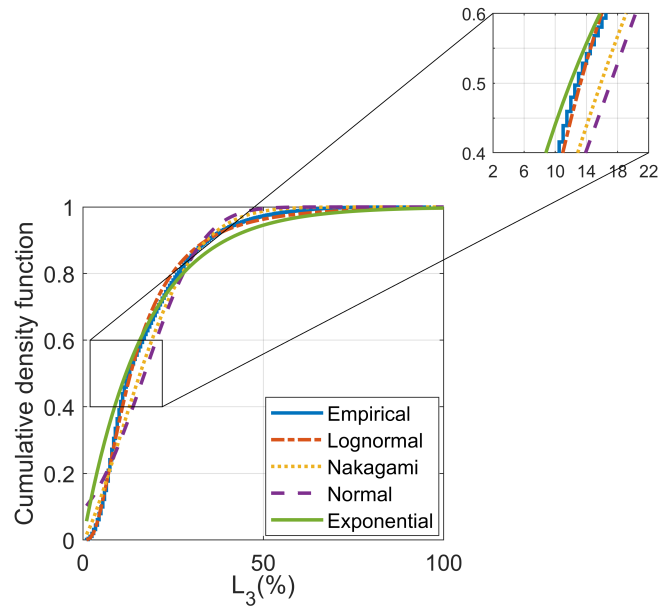


Figure 6.14: The cumulative density functions of the co-existence of other vehicles in the left-hand lane at 16:00-19:00.

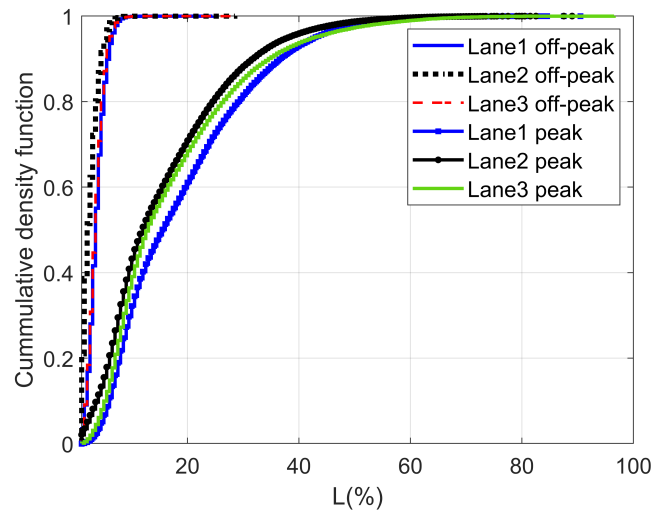


Figure 6.15: The cumulative density function of the co-existence of other vehicles in the adjacent lanes during off-peak hours 00:00-03:00 and during peak hours 16:00-19:00 periods.

Table 6.3: Simulation parameters.

Symbol	Parameter	Values	Ref
P_T	Transmitted power (normalized)	1 W	-
$\Psi_{1/2}$	Semi-angle	30°	Zaki et al. (2019)
γ	PD responsivity	0.54 A/W	Kim et al. (2015)
Ψ_c	The receiver field of view	80°	Al-Kinani et al. (2018)
A_r	Receiver area	$1 \times 10^{-4} m^2$	Al-Kinani et al. (2018)
C_{pd}	Capacitance of PD per unit area	$1.12 \mu F m^{-2}$	Luo et al. (2015)
I_2	Noise bandwidth factor	0.562	Kahn and Barry (1997)
I_3	Noise bandwidth factor	0.0868	Kahn and Barry (1997)
B_w	Noise bandwidth	100 MHz	Ghassemlooy et al. (2019)
G_ν	Open-loop voltage gain	10	Luo et al. (2015)
Γ_k	FET channel noise factor	1.5	Luo et al. (2015)
g_m	FET transconductance	30 mS	Kahn and Barry (1997)
I_{bg}	Background current at $\lambda = 850$ nm	55.4 μA	Ghassemlooy et al. (2019)
ρ	Reflection coefficient	0.8	Al-Kinani et al. (2018)

requires further investigation. The following section discusses the BER performance of V2V-VLC on different lanes, taking into account the probability of the co-existence of other vehicles in the adjacent lanes.

6.3 BER performance of the V2V-VLC channel

Considering the reflection from the surrounding vehicles, the received power P_R is given as a linear combination of the received power from LOS and NLOS paths (Ghassemlooy et al., 2019):

$$P_R = P_T H(0) = P_T (H_{LOS}(0) + L_k H_{NLOS}(0)). \quad (6.6)$$

The shot noise in V2V-VLC systems accounts for the interference power P_I due to the

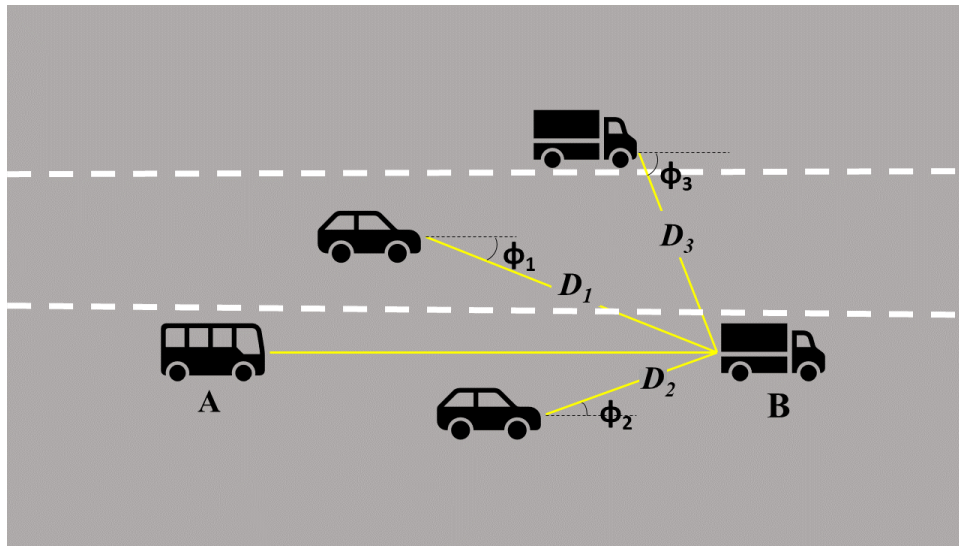
sun and artificial light sources (Luo, Ghassemlooy, Minh, Bentley, Burton and Tang, 2015; Béchadergue et al., 2019). Shot noise due to sunlight peaks at morning hours (Lee et al., 2009), while noise due to artificial light sources of the adjacent vehicles peaks at night hours. Therefore, it is expected that the magnitude of interference power P_I changes according to the presence of other vehicles in the adjacent lanes during different periods of the day. Considering the probability of co-existence of other vehicles in the adjacent lanes L_k during different periods of the day, the shot noise given in (2.3) can be re-written as (Ghassemlooy et al., 2019)

$$\sigma_{shot}^2 = 2q(P_R + L_k P_I)\gamma B_w + 2qI_{bg}I_2 B_w. \quad (6.7)$$

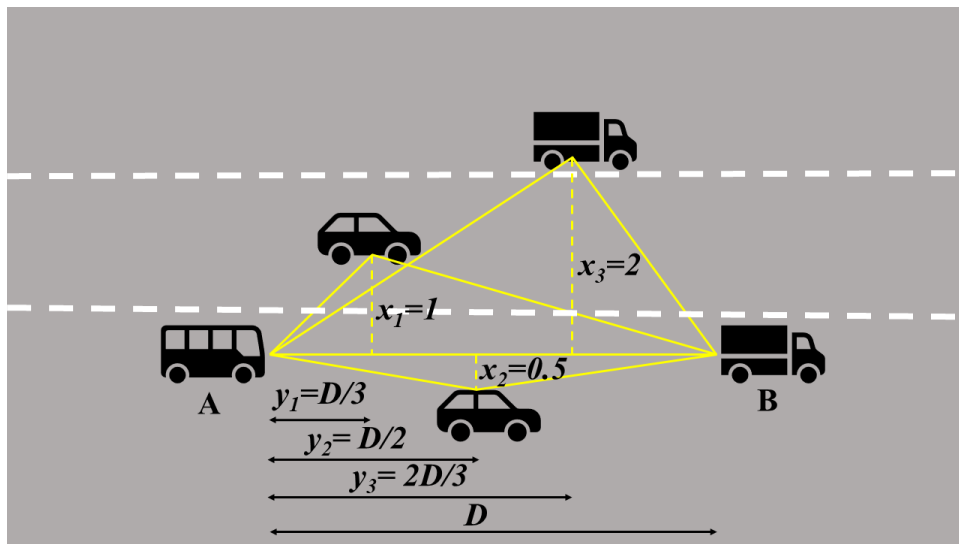
To study the SNR and the associated BER performance of the V2V-VLC channel, the communication link illustrated in Figure 6.16 is considered. The figure shows a typical communication link with the transmitter and receiver vehicles A and B. Three vehicles are present in the adjacent lanes located at (x_j, y_j) of $(1, D_l/3)$ m, $(0.5, D_l/2)$ m and $(2, 2D_l/3)$ m, where D_l is the longitudinal inter-vehicle spacing that follows a log-normal distribution with parameters given in Table 3.3. Therefore, the communication link is affected by the presence of these vehicles which act as potential reflectors and add ambient noise. The BER performance is examined with respect to the transmitted SNR per lane and at different periods of the day using simulation parameters summarised in Table 6.3. Using transmitted SNR to evaluate the impact of varying channel impulse response performance is a standard method in VLC systems (Marshoud et al., 2017; Butala et al., 2014; Chen et al., 2020). Considering the SNR at the receiver in (2.33), the transmitted SNR is given by

$$SNR_{RT}[dB] = 10 \log \left(\frac{\gamma^2 H(0)^2 P_T^2}{\sigma_T^2} \right) - 10 \log \left(H(0)^2 \right). \quad (6.8)$$

Hence, the SNR (in dB) values at the receiver are offset by the corresponding channel path loss values (Marshoud et al., 2017). The BER performance is examined for a pseudorandom sequence of 10^7 bits and a data rate of 50 Mbps assuming OOK modulation scheme as explained in Section 2.2.2.4. The log-normally distributed lane-dependent inter-vehicle spacing D_l with parameters summarised in Table 3.3 is considered to calculate the received power and hence the SNR per lane. The DC gain $H_{LOS}(0)$ is calculated using the empirical



(a)



(b)

Figure 6.16: A typical communication link between two vehicles travelling on a three-lane motorway and co-existence of other vehicles in the adjacent lanes which act as a) interference sources and b) reflectors.

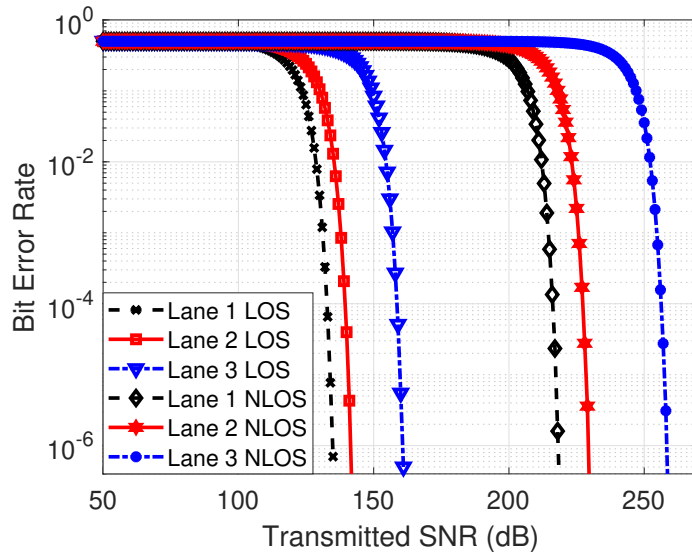
model in (4.12) and the Lambertian model in (4.2) to mimic the asymmetrical and symmetrical radiation pattern of vehicle sources, respectively.

A communication link between a transmitter vehicle A and a receiver vehicle B in presence

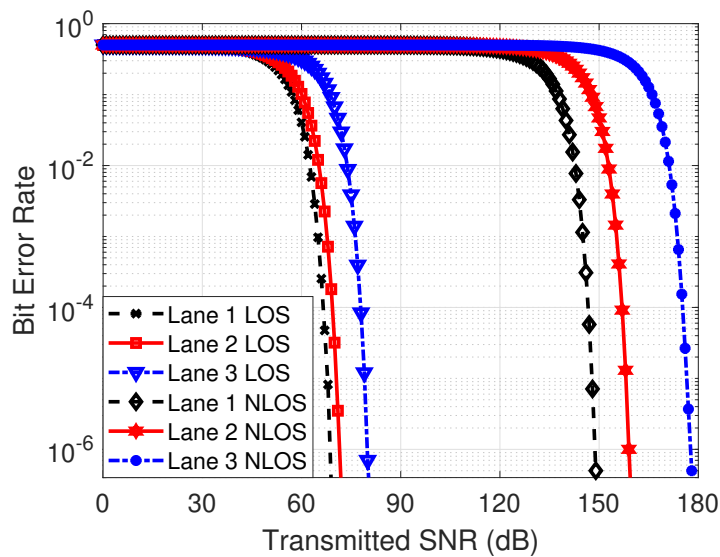
of a vehicle j driving on the adjacent lane is illustrated in Figure 2.7. The figure shows the geometry of **NLOS** component due to reflection. Assuming that the vehicle surface is a Lambertian reflector (Akafuah et al., 2016; Ďurikovič and Ágošton, 2007), the channel gain of the **NLOS** component is given in (2.17).

Figure 6.17 illustrates the **BER** performance of the **V2V-VLC** link in the three lanes between 00:00 and 03:00 for the empirical and the Lambertian models in Figure 6.17 (a) and (b), respectively. The figure shows the **BER** performance of **LOS** components and **NLOS** components due to reflection from vehicles in the adjacent lanes. As expected, the **BER** performance varies widely among different lanes because the mean inter-vehicle spacing in different lanes varies as summarised in Table 3.3. The left-hand lane (Lane 1) has the lowest **BER** values for **LOS** and **NLOS** paths compared to the middle and right-hand lanes (Lane 2 and 3). For example, Figure 6.17 (a) shows that at **SNR** = 130 dB, the **BER** values of the **LOS** link are 0.452, 0.101 to 0.003 for the right-hand lanes (Lane 3), middle lane (Lane 2) and the left-hand lane (Lane 1), respectively. Similarly, at **SNR** = 205 dB, the **BER** values of the **NLOS** link are 0.49, 0.38 and 0.07 for right-hand lanes (Lane 3), middle lane (Lane 2) and the left-hand lane (Lane 1), respectively. This is expected as the mean inter-vehicle spacing in the left-hand lane is 57.2 m, which is lower than 67.1 m and 109.8 m for the middle and right-hand lanes, respectively. In addition, Figure 6.17 (b) shows that lower **SNR** values are required when the Lambertian is used, e.g. at **SNR** = 60 dB, the **BER** are 0.31, 0.10 and 0.04 for left-hand lanes (Lane 3), middle lane (Lane 2) and the right-hand lane (Lane 1), respectively. This is expected because the Lambertian model has a lower mean path loss value of -79.6dB as given in Table 4.5 compared to the empirical model that has a mean path loss value of -102.8 dB. Hence, the Lambertian model supports longer transmission distances. Figure 6.17 shows a large difference between the **BER** performance of the **LOS** and **NLOS** components. This difference is due to variation of the mean value of the probability of the co-existence of other vehicles in the different lanes, which does not exceed 5%. Hence, the probability of reflection occurrence is very low.

Figure 6.18 provides the **BER** performance of the **LOS** and **NLOS** components in three lanes at 16:00-19:00 for the empirical and the Lambertian models. According to the figure, the



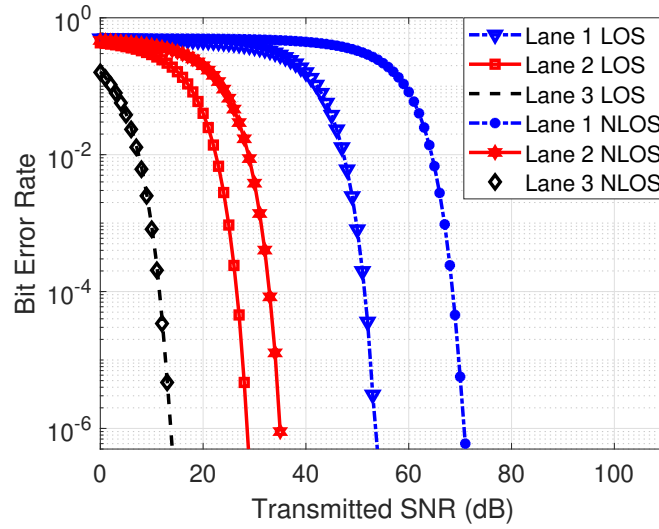
(a)



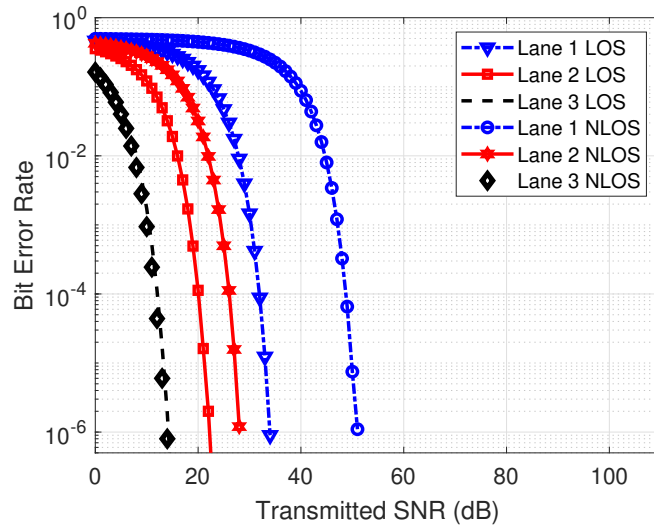
(b)

Figure 6.17: BER performance of the V2V-VLC link in three lanes at 00:00-03:00 when a) the empirical and b) the Lambertian models are considered.

right-hand lane (Lane 3) has lower BER values than the middle and left-hand lanes (Lane 2 and 1). For example, at SNR = 10 dB, when the empirical radiation model is used, the



(a)



(b)

Figure 6.18: BER performance of the V2V-VLC link in three lanes at 16:00-19:00 when a) the empirical and b) the Lambertian models are considered.

BER values are 0.489, 0.290 and 0.001, and when the empirical radiation model is used, they are 0.487, 0.120 and 0.002, for left-hand lanes (Lane 1), middle lane (Lane 2) and the right-hand lane (Lane 3), respectively. The variation in BER values is because the mean

inter-vehicle spacing in the right-hand lane (Lane 3) given in Table 4.5 is 2.48 m which is shorter than 3.93 m and 7.79 m for the middle lane (Lane 2) and the left-hand lane (Lane 1), respectively. In addition, in the right-hand lane (Lane 3), the BER values of the NLOS and LOS components are close while they differ in the middle lane (Lane 2) and the left-hand lane (Lane 1). This is because of the high probability of the co-existence of other vehicles in the adjacent lanes which reaches 70% and hence a high probability of reflection occurrence in the right-hand lane.

Figure 6.17 and Figure 6.18 show that the required ranges of SNR vary widely from hundreds of decibels during the off-peak hours to tens of decibels during the peak hours to achieve comparable BER values. This indicates the dependency of channel capacity on traffic conditions during different periods of the day.

A summary of the required transmitted SNR values to achieve acceptable BER performance of 10^{-6} for different radiation pattern models, lanes, and link configurations are provided in Table 6.4. The average inter-vehicle spacing values are lower at peak than at off-peak hours. Hence, higher SNR values are required at off-peak hours compared to the peak hours to achieve the desired SNR. Furthermore, the table shows that there is a feasibility of communication relying on the NLOS component during peak hour. This is important because the probability of LOS link blocking is higher during peak hours than it is during off-peak. However, V2V-VLC can support communication for both peak and off-peak hours. It has been shown that the required values of SNR using the Lambertian model are lower than the empirical model under the same channel condition due to the reduced path loss.

6.4 Summary

The impact of the presence of other vehicles in the adjacent lanes on the performance of the V2V-VLC channel was studied in this chapter. The study showed that the probability of co-existence of other vehicles in the adjacent lanes follows a log-normal distribution and varies with traffic density during different periods of the day.

The SNR and BER performance of V2V-VLC systems was studied for different vehicles'

Table 6.4: A summary of the transmitted SNR values to achieve $BER=10^{-6}$ for different models, lanes, and configurations.

Time	model	Lane	Link configuration	SNR (dB)
00:00-03:00	Lambertian model	left (1)	LOS	68.6
		middle (2)		71.5
		right (3)		79.9
		left (1)	NLOS	148.7
		middle (2)		159.0
		right (3)		177.7
	Empirical model	left (1)	LOS	134.8
		middle (2)		141.5
		right (3)		160.7
		left (1)	NLOS	218.2
		middle (2)		229.3
		right (3)		258.3
16:00-19:00	Lambertian model	left (1)	LOS	34.0
		middle (2)		22.2
		right (3)		14.2
		left (1)	NLOS	51.0
		middle (2)		28.0
		right (3)		13.9
	Empirical model	left (1)	LOS	53.6
		middle (2)		28.6
		right (3)		13.7
		left (1)	NLOS	70.8
		middle (2)		35.0
		right (3)		13.5

sources radiation pattern and dynamic traffic conditions at different times of the day. The results showed that acceptable performance of $\text{BER} = 10^{-6}$ can be achieved relying on the **NLOS** component during peak hour when the mean inter-vehicle spacing values are relatively low and the probability of co-existence of other vehicles in the adjacent lanes is high. At off-peak hours, the **BER** performance of **NLOS** components is poor when the mean inter-vehicle spacing values are high and the probability of co-existence of other vehicles in the adjacent lanes is low.

Chapter 7

Conclusions and Future work

The main objective of this research was to study the impact of unpredictable movement pattern due to dynamic traffic on the channel model of systems. In such systems, the movement of transmitter, receiver and surrounding vehicles adds a factor of randomness to the communication system. Therefore, a statistical model that considers the spatial variation due to movement was established. Research findings and conclusions are summarised in Section 7.1. Areas of potential future work are suggested in Section 7.2.

7.1 Conclusions

Considering the technical background and fundamental principles Chapter 2 showed that variations in the V2V-VLC link geometry, the transmission distance, irradiance angle and incident angle have a significant impact on the channel model. The transmission distance depends on the inter-vehicle spacing which changes with the traffic conditions during different times of the day. The irradiance and incident angles change with the angular lateral deviation between vehicles which is affected by the radiation pattern of vehicles' sources. Therefore, to establish a statistical channel model that can describe the V2V-VLC link geometrical changes, the impact of dynamic traffic conditions and the radiation pattern of vehicles' sources should be considered. In addition, the impact of weather conditions should be

considered to study the **V2V-VLC** channel model. Therefore, relying on traffic measurements collected from the M6 and M42 motorways, Chapter 3 investigated the impact of the inter-vehicular variation assuming negligible the variation of the irradiance and incident angles due to the angular lateral deviation between vehicles. The analysis showed that a log-normal distribution provides the best fit to describe inter-vehicle spacing variation at different times of the day, and consequently, the path loss has a normal distribution. The results showed 10 dB difference, depending on traffic density, between the mean path loss values for the time intervals 00:00-03:00 and 12:00-15:00.

Chapter 4 studied the combined impact of vehicles' sources radiation pattern and dynamic traffic on the **LOS V2V-VLC** statistical channel model. The study examined the Lambertian, piecewise Lambertian, Gaussian and empirical radiation pattern models to describe the angular distribution of vehicles' light sources. The statistical models showed that the path loss model can be given by the convolution between inter-vehicle spacing and radiation pattern distributions. A difference in the mean path loss values of at least 2 dB was observed between Gaussian and Lambertian. The mean path loss value of Gaussian radiation pattern is the least followed by Lambertian, Piecewise Lambertian and asymmetrical patterns. This indicates the impact of the radiation pattern on the path loss values of the channel. In addition, among the considered radiation pattern models, the Gaussian model can be adopted to describe vehicles' sources with different designs. Chapter 4 also investigated the impact of the weather on the **LOS** component of the **V2V-VLC** channel. The results showed that poor weather conditions negatively affect the attenuation. For example, the mean path loss value reaches the highest values of -137.5 dB under heavy fog conditions, compared to 103.5 dB for clear weather when the empirical radiation pattern is considered during the time interval 0:00-03:00. The additional attenuation due to heavy fog shifts the mean path loss value, but it does not change the statistical distribution of the path loss.

Having studied the impact of dynamic traffic on the **LOS** component of **V2V-VLC** in Chapter 4, the path loss and the temporal properties of **NLOS** (multipath) **V2V-VLC** systems were investigated in Chapter 5. **V2V-VLC** channel path losses due to reflection from different surfaces with different natures and physical states were examined. The results showed that the

channel path loss due to reflection from surrounding vehicles is at least 10 dB lower than its values due to reflection from other surfaces. Therefore, the study focused on reflection from surrounding vehicles as dominant reflectors to establish the statistical distribution of the **NLOS V2V-VLC** channel path loss. The results showed that the asymmetrical radiation pattern of the vehicle's source has a marginal effect on the **NLOS** path loss distribution. However, it affects the mean and the standard deviation values of the distribution. In addition, reflection from surrounding vehicles increases the channel gain if multiple reflectors are considered. The temporal properties of the **V2V-VLC** channel under different traffic conditions showed that the **V2V-VLC** channel is time-variant non-stationary with flat and slow fading.

Considering that the surrounding vehicles are the main cause of reflection, quantifying the presence of vehicles in the adjacent lanes is required to study the **V2V-VLC** system performance. This is because the number of surrounding vehicles varies with traffic conditions. Therefore, in Chapter 6, a novel parameter was proposed to quantify the probability of co-existence of other vehicles in the adjacent lanes based on traffic measurements from two motorways in the UK. The analysis showed that the probability of co-existence of other vehicles in the adjacent lanes follows a log-normal distribution with mean values that increases to 19.9% at high-traffic density during peak hours and decays to 2.55% at low-density traffic during off-peak hours. Furthermore, the **SNR** and **BER** performance of **V2V-VLC** systems was studied in Chapter 6, considering different vehicles' sources of radiation pattern and dynamic traffic conditions at different times of the day. The results showed that acceptable performance of $\text{BER}=10^{-6}$ can be achieved relying on the **NLOS** component during rush hour because the mean inter-vehicle spacing values are relatively low and the probability of co-existence of other vehicles in the adjacent lanes is as high as 90%. However, **BER** performance of **NLOS** components at off-peak hours is poor because the mean inter-vehicle spacing values are high and the probability of co-existence of other vehicles in the adjacent lanes lower than 5%.

7.2 Future work

VLC is promising technology with many interesting research areas that require further investigations. Potential research directions to extend the research reported in this thesis are as follows:

- **Three-dimensional random traffic process:** extend the work in Chapter 3 to establish a three-dimensional traffic random process that considers realistic traffic conditions to describe the V2V-VLC channel as a function of time, delay and distance. The analytical model is then compared to outcomes of the measurement campaign under realistic driving scenarios and traffic conditions at different times of the day.
- **Three-dimensional radiation pattern:** extend the work in Chapter 4 to establish a three-dimensional radiation pattern model to describe the three-dimensional angular distribution in the azimuth and vertical planes of vehicles light sources with different designs and manufacturers.
- **Time properties of dynamic V2V-VLC channel:** extend the work in Chapter 5 to estimate the distance over which the V2V-VLC channel is considered stationary and the probability of link duration.
- **Tight bounds on channel capacity for dynamic V2V-VLC:** extend the work in Chapter 6 to estimate tight bounds on channel capacity for dynamic V2V-VLC considering the variation of inter-vehicle spacing due to dynamic traffic at different times of the day.

Bibliography

- Abdelkader, Y. and Al-Marzouq, Z. (2010), 'Probability distribution relationships', *Statistica* **70**, 41–51.
- Abualhoul, M. Y., Munoz, E. T. and Nashashibi, F. (2018), The use of lane-centering to ensure the visible light communication connectivity for a platoon of autonomous vehicles, in '2018 IEEE International Conference on Vehicular Electronics and Safety (ICVES)', pp. 1–6.
- Abuella, H., Miramirkhani, F., Ekin, S., Uysal, M. and Ahmed, S. (2019), 'ViLDAR—visible light sensing-based speed estimation using vehicle headlamps', *IEEE Transactions on Vehicular Technology* **68**(11), 10406–10417.
- Adrian, W. and Jobanputra, R. (2005), Influence of pavement reflectance on lighting for parking lots, Research and Development information SN2458, Portland Cement Association, Skokie, IL, USA.
- Ahmad, Z., Geisar, P., Salih, O. and Rajbhandari, S. (2016), Design of a visible light communication system for deep sea divers based on analogue frequency modulation, in '2016 10th International Symposium on Communication Systems, Networks and Digital Signal Processing (CSNDSP)', pp. 1–5.
- Akafuah, N. K., Poozesh, S., Salaimeh, A., Patrick, G., Lawler, K. and Saito, K. (2016), 'Evolution of the automotive body coating process—a review', *Coatings* **6**(2), 1–24.

- Al-Kinani, A., Sun, J., Wang, C., Zhang, W., Ge, X. and Haas, H. (2018), 'A 2-D non-stationary GBSM for vehicular visible light communication channels', *IEEE Trans. Wireless Commun.* **17**(12), 7981–7992.
- Al-Kinani, A., Wang, C., Zhou, L. and Zhang, W. (2018), 'Optical wireless communication channel measurements and models', *IEEE Communications Surveys Tutorials* **20**(3), 1939–1962.
- Al-Kinani, A., Wang, C., Zhu, Q., Fu, Y., Aggoune, E. M., Talib, A. and Al-Hasaani, N. A. (2020), 'A 3D non-stationary GBSM for vehicular visible light communication MISO channels', *IEEE Access* **8**, 140333–140347.
- Alam, M. R. and Faruque, S. (2016), Prospects of differential optical receiver with ambient light compensation in vehicular visible light communication, *in* '2016 IEEE Vehicular Networking Conference (VNC)', pp. 1–4.
- Amanor, D. N., Edmonson, W. W. and Afghah, F. (2018), 'Intersatellite communication system based on visible light', *IEEE Transactions on Aerospace and Electronic Systems* **54**(6), 2888–2899.
- Arfaoui, M. A., Soltani, M. D., Tavakkolnia, I., Ghrayeb, A., Safari, M., Assi, C. and Haas, H. (2020), 'Physical layer security for visible light communication systems: A survey', *IEEE Communications Surveys Tutorials* pp. 1–1.
- Audi (2021), 'LED rear lights'. [Online; accessed April 21, 2021].
URL: https://shops.audi.com/en_GB/web/zubehoer/p/led-rear-lights-8w6052100-9
- Avătămăniței, S. A., Căilean, A. M., Done, A., Dimian, M. and Popa, V. (2020), Experimental evaluation of traffic light to vehicle visible light communications in snowfall conditions, *in* '2020 7th International Conference on Control, Decision and Information Technologies (CoDIT)', Vol. 1, pp. 693–696.

Avătămăniței, S. A., Căilean, A.-M., Done, A., Dimian, M. and Prelipceanu, M. (2020), 'Noise resilient outdoor traffic light visible light communications system based on logarithmic transimpedance circuit: Experimental demonstration of a 50 m reliable link in direct sun exposure', *Sensors* **20**(3).

URL: <https://www.mdpi.com/1424-8220/20/3/909>

Béchadergue, B., Shen, W.-H. and Tsai, H.-M. (2019), 'Comparison of OFDM and OOK modulations for vehicle-to-vehicle visible light communication in real-world driving scenarios', *Ad Hoc Networks* **94**, 101944.

Ben-Arie, J. (1991), Image processing operators and transforms generated by a set of multidimensional neural lattices that use the central limit, in '[Proceedings] 1991 IEEE International Joint Conference on Neural Networks', pp. 987–993 vol.2.

Butala, P. M., Elgala, H. and Little, T. D. C. (2014), Performance of optical spatial modulation and spatial multiplexing with imaging receiver, in 'Proc. Wireless Commun. Netw. Conf. (WCNC' 14)', Istanbul, Turkey, pp. 394–399.

Béchadergue, B., Chassagne, L. and Guan, H. (2019), 'Simultaneous visible light communication and distance measurement based on the automotive lighting', *IEEE Trans. Intell. Veh.* **4**(4), 532–547.

Căilean, A.-M., Dimian, M. and Popa, V. (2020), 'Noise-adaptive visible light communications receiver for automotive applications: a step toward self-awareness', *Sensors* **20**(13), 3764.

Cervinka, D., Ahmad, Z., Salih, O. and Rajbhandari, S. (2020), A study of yearly sunlight variance effect on vehicular visible light communication for emergency service vehicles, in 'Proc. 12th IEEE/IET Int. Symp. Commun. Syst. Netw. and Digit. Signal Process. (CSNDSP'20)', Porto, Portugal, pp. 1–6.

Chen, A., Wu, H., Wei, Y. and Tsai, H. (2016), Time variation in vehicle-to-vehicle visible

- light communication channels, in '2016 IEEE Vehicular Networking Conference (VNC)', pp. 1–8.
- Chen, C., Yang, H., Du, P., Zhong, W. D., Alphones, A., Yang, Y. and Deng, X. (2020), 'User-centric MIMO techniques for indoor visible light communication systems', *IEEE Syst. J.* **14**(3), 3202–3213.
- Chen, F., Wang, K., Qin, Z., Wu, D., Luo, X. and Liu, S. (2010), 'Design method of high-efficient LED headlamp lens', *Optics Express* **18**, 20926–38.
- Chen, J. and Wang, Z. (2020), 'Topology control in hybrid VLC/RF vehicular Ad-Hoc network', *IEEE Trans. Wireless Commun.* **19**(3), 1965–1976.
- Cheng, L., Viriyasitavat, W., Boban, M. and Tsai, H. (2018), 'Comparison of radio frequency and visible light propagation channels for vehicular communications', *IEEE Access* **6**, 2634–2644.
- Chun, H., Gomez, A., Quintana, C., Zhang, W., Faulkner, G. and O'Brien, D. (2019), 'A wide-area coverage 35 Gb/s visible light communications link for indoor wireless applications', *Scientific Reports* **9**.
- Chung, Y. H. and Oh, S. (2013), Efficient optical filtering for outdoor visible light communications in the presence of sunlight or artificial light, in 'Proc. 2013 Int. Symp. Intell. Signal Process. Commun. Syst. (ISISPCS'13)', Naha, Japan, pp. 749–752.
- Ciaramella, E., Cossu, G., Ertunc, E., Gilli, L., Messa, A., Presi, M., Rannello, M., Bresciani, F., Basso, V., Dell'Orso, R. and Palla, F. (2020), Prospects of visible light communications in satellites, in '2020 22nd International Conference on Transparent Optical Networks (ICTON)', pp. 1–4.
- Cui, Z., Wang, C. and Tsai, H. (2014), Characterizing channel fading in vehicular visible light communications with video data, in '2014 IEEE Vehicular Networking Conference (VNC)', pp. 226–229.

- Căilean, A., Dimian, M., Popa, V., Chassagne, L. and Cagneau, B. (2016), ‘Novel DSP receiver architecture for multi-channel visible light communications in automotive applications’, *IEEE Sensors J.* **16**(10), 3597–3602.
- Ding, J., I, C. and Xu, Z. (2016), ‘Indoor optical wireless channel characteristics with distinct source radiation patterns’, *IEEE Photonics Journal* **8**(1), 1–15.
- Ebrahim, K. J. and Al-Omary, A. (2017), Sandstorm effect on visible light communication, in ‘2017 9th IEEE-GCC Conference and Exhibition (GCCCE)’, pp. 1–7.
- Elamassie, M., Karbalayghareh, M., Miramirkhani, F., Kizilirmak, R. and Uysal, M. (2018), Effect of fog and rain on the performance of vehicular visible light communications, in ‘2018 IEEE 87th Vehicular Technology Conference (VTC Spring)’.
- Elamassie, M. and Uysal, M. (2020), ‘Vertical underwater visible light communication links: Channel modeling and performance analysis’, *IEEE Transactions on Wireless Communications* **19**(10), 6948–6959.
- Eldeeb, H. B., Elamassie, M. and Uysal, M. (2020), Vehicle-to-infrastructure visible light communications: Channel modelling and capacity calculations, in ‘2020 12th International Symposium on Communication Systems, Networks and Digital Signal Processing (CSNDSP)’, pp. 1–6.
- Eldeeb, H. B., Eso, E., Jarchlo, E. A., Zvanovec, S., Uysal, M., Ghassemlooy, Z. and Sathian, J. (2021), ‘Vehicular vlc: A ray tracing study based on measured radiation patterns of commercial taillights’, *IEEE Photonics Technology Letters* pp. 1–1.
- Eldeeb, H. B., Miramirkhani, F. and Uysal, M. (2019), A path loss model for vehicle-to-vehicle visible light communications, in ‘2019 15th International Conference on Telecommunications (ConTEL)’, pp. 1–5.
- Eldeeb, H., Eso, E., Uysal, M., Ghassemlooy, Z., Zvanovec, S. and Sathian, J. (2020), Vehicular visible light communications: The impact of taillight radiation pattern, in ‘2020 IEEE Photonics Conference (IPC)’.

- Esmail, M. A., Fathallah, H. and Alouini, M. (2017), 'Outage probability analysis of FSO links over foggy channel', *IEEE Photon. J.* **9**(2), 1–12.
- Eso, E., Burton, A., Hassan, N. B., Abadi, M. M., Ghassemlooy, Z. and Zvanovec, S. (2019), Experimental investigation of the effects of fog on optical camera-based VLC for a vehicular environment, in '2019 15th International Conference on Telecommunications (ConTEL)', pp. 1–5.
- Ford (2020), 'Features and technical specification: Mondeo brochure', Brochure.
URL: <https://www.ford.co.uk/cars/mondeo/models-specs/st-line-edition#>
- Ghassemlooy, Z., Popoola, S., W.O.Tang, Zvanovec, X. and Rajbhandari, S. (2017), Visible light communications – a review, in 'IEEE COMSOC MMTC Communications - Frontiers', Vol. 12, pp. 6–13.
- Ghassemlooy, Z., Popoola, W. and Rajbhandari, S. (2019), *Optical wireless communications: system and channel modelling with Matlab®*, CRC Press (Inc.), Boca Raton, FL.
- Goldsmith Andrea (2005), *Wireless communications*, Cambridge University Press, Cambridge.
- Greenberg, I. (1966), 'The log-normal distribution of headways', *Australian Road Res.* **2**(7).
- Gupta, A., Sharma, N., Garg, P. and Alouini, M. (2017), 'Cascaded FSO-VLC communication system', *IEEE Wireless Communications Letters* **6**(6), 810–813.
- Haas, H., Yin, L., Wang, Y. and Chen, C. (2016), 'What is lifi?', *Journal of Lightwave Technology* **34**(6), 1533–1544.
- Hanacekl, V. (2018), 'Driving in evening traffic jam and snow calamity weather'. [Online; accessed April 21, 2021].
URL: <https://picjumbo.com/driving-in-evening-traffic-jam-and-snow-calamity-weather>

- Hassan, N. U., Naeem, A., Pasha, M. A., Jadoon, T. and Yuen, C. (2015), 'Indoor positioning using visible LED lights: A survey', *ACM Computing Surveys (CSUR)* **48**(2), 20.
- Highways England (n.d.), 'Site data tools'.
URL: www.sitedatatools.co.uk
- Hranilovic, S. (2005), *Wireless Optical Communication Systems*, 1st ed. 2005. edn, Springer Science & Business Media.
- Hu, G.-y., Chen, C.-y. and Chen, Z.-q. (2007), 'Free-space optical communication using visible light', *Journal of Zhejiang University - Science A: Applied Physics and Engineering* **8**, 186–191.
- Hua-Yen Tseng, Wei, Y., Ai-Ling Chen, Hao-Ping Wu, Hsuan Hsu and Tsai, H. (2015), Characterizing link asymmetry in vehicle-to-vehicle visible light communications, in '2015 IEEE Vehicular Networking Conference (VNC)', pp. 88–95.
- Huang, H., Yang, A., Feng, L., Ni, G. and Guo, a. (2017), 'Artificial neural-network-based visible light positioning algorithm with a diffuse optical channel', *Chinese Optics Letters* **15**, 050601–50605.
- Huang, T., Yang, W., Wu, J., Ma, J., Zhang, X. and Zhang, D. (2019), 'A survey on green 6G network: Architecture and technologies', *IEEE Access* **7**, 175758–175768.
- Ishihara, S., Rabsatt, R. V. and Gerla, M. (2015), Improving reliability of platooning control messages using radio and visible light hybrid communication, in '2015 IEEE Vehicular Networking Conference (VNC)', pp. 96–103.
- Islim, M. S. and Haas, H. (2017), An investigation of the solar irradiance effect on visible light communications, in '2017 IEEE 28th Annual International Symposium on Personal, Indoor, and Mobile Radio Communications (PIMRC)', pp. 1–6.

- Iturralde, D., Seguel, F., Soto, I., Azurdia, C. and Khan, S. (2017), 'A new VLC system for localization in underground mining tunnels', *IEEE Latin America Transactions* **15**(4), 581–587.
- Jiang, H., Qiu, H., He, N., Popoola, W., Ahmad, Z. and Rajbhandari, S. (2020), 'Performance of spatial diversity DCO-OFDM in a weak turbulence underwater visible light communication channel', *Journal of Lightwave Technology* **38**(8), 2271–2277.
- Jung, S., Hann, S. and Park, C. (2011), 'TDOA-based optical wireless indoor localization using LED ceiling lamps', *IEEE Transactions on Consumer Electronics* **57**(4), 1592–1597.
- Játiva, P. P., Azurdía-Meza, C. A., Sánchez, I., Seguel, F., Zabala-Blanco, D., Firoozabadi, A. D., Gutiérrez, C. A. and Soto, I. (2020), 'A VLC channel model for underground mining environments with scattering and shadowing', *IEEE Access* **8**, 185445–185464.
- Kahn, J. and Barry, J. (1997), 'Wireless infrared communications', *Proceedings of the IEEE* **85**(2), 265–298.
- Karbalayghareh, M., Miramirkhani, F., Eldeeb, H. B., Kizilirmak, R. C., Sait, S. M. and Uysal, M. (2020), 'Channel modelling and performance limits of vehicular visible light communication systems', *IEEE Transactions on Vehicular Technology* pp. 1–1.
- Karbalayghareh, M., Miramirkhani, F., Safari, M. and Uysal, M. (2019), Vehicular visible light communications with spad receivers, in '2019 IEEE Wireless Communications and Networking Conference (WCNC)'.
doi:10.1109/WCNC.2019.8699177
- Kazemi, H., Safari, M. and Haas, H. (2019), 'A wireless optical backhaul solution for optical attocell networks', *IEEE Transactions on Wireless Communications* **18**(2), 807–823.
- Khoder, R., Naja, R. and Tohme, S. (2020), Impact of interference on visible light communication performance in a vehicular platoon, in 'Proc. 2020 Int. Wireless Commun. Mobile Comput. (IWCMC'20)', Limassol, Cyprus, pp. 1935–1939.

- Kim, I. I., McArthur, B. and Korevaar, E. (2001), Comparison of laser beam propagation at 785 nm and 1550 nm in fog and haze for optical wireless communications, *in* 'SPIE Optics East'.
- Kim, Y. H., Cahyadi, W. A. and Chung, Y. H. (2015), 'Experimental demonstration of VLC-based vehicle-to-vehicle communications under fog conditions', *IEEE Photon. J.* **7**(6), 1–9.
- Kim, Y.-h. and Chung, Y.-H. (2015), 'Experimental outdoor visible light data communication system using differential decision threshold with optical and color filters', *Optical Engineering* **54**, 040501.
- Lee, I. E., Sim, M. L. and Kung, F. W. L. (2009), 'Performance enhancement of outdoor visible-light communication system using selective combining receiver', *IET Optoelectronics* **3**(1), 30–39.
- Lee, S. J., Kwon, J. K., Jung, S. Y. and Kwon, Y. H. (2012a), Simulation modeling of visible light communication channel for automotive applications, *in* 'Proc. 2012 15th ITSC', pp. 463–468.
- Lee, S., Kwon, J. K., Jung, S.-Y. and Kwon, Y.-H. (2012b), 'Evaluation of visible light communication channel delay profiles for automotive applications', *EURASIP journal on Wireless Communications and Networking* **2012**(1), 370.
- Lee/Reuters, J. (2017), 'Vehicles drive on the fourth ring during a smoggy morning in beijing'. [Online; accessed April 21, 2021].
URL: <https://www.csmonitor.com/Environment/2017/0304/Why-smog-in-Asia-is-an-American-concern>
- Liu, C., Sadeghi, B. and Knightly, E. (2011), Enabling vehicular visible light communication (V2LC) networks, *in* 'Proceedings of the Eighth International Workshop on Vehicular Ad Hoc Networks', pp. 41–50.

- Luo, P., Ghassemlooy, Z., Bentley, E., Burton, A. and Tang, X. (2015), 'Bit-error-rate performance of a car-to-car VLC system using 2×2 MIMO', *Mediterranean J. Comput. Netw.* **11**, 400–407.
- Luo, P., Ghassemlooy, Z., Minh, H. L., Bentley, E., Burton, A. and Tang, X. (2015), 'Performance analysis of a car-to-car visible light communication system', *Appl. Opt.* **54**(7), 1696–1706.
- Marshoud, H., Sofotasios, P. C., Muhaidat, S., Karagiannidis, G. K. and Sharif, B. S. (2017), 'On the performance of visible light communication systems with non-orthogonal multiple access', *IEEE Trans. Wireless Commun.* **16**(10), 6350–6364.
- Masini, B. M., Bazzi, A. and Zanella, A. (2017), Vehicular visible light networks with full duplex communications, in '2017 5th IEEE International Conference on Models and Technologies for Intelligent Transportation Systems (MT-ITS)', pp. 98–103.
- Matolcsy, B. and Udvary, E. (2020), Common-mode noise rejection in V2V/V2I communication based on differential VLC transmission, in '2020 12th International Symposium on Communication Systems, Networks and Digital Signal Processing (CSNDSP)', pp. 1–6.
- Memedi, A. and Dressler, F. (2021), 'Vehicular visible light communications: A survey', *IEEE Communications Surveys Tutorials* **23**(1), 161–181.
- Memedi, A., Tebruegge, C., Jahneke, J. and Dressler, F. (2018), Impact of vehicle type and headlight characteristics on vehicular VLC performance, in '2018 IEEE Vehicular Networking Conference (VNC)', pp. 1–8.
- Memedi, A., Tsai, H. and Dressler, F. (2017), Impact of realistic light radiation pattern on vehicular visible light communication, in 'Proc. IEEE Global Commun. Conf. (GLOBECOM'17)', Singapore, pp. 1–6.
- Moreno, I. and Sun, C.-C. (2008), 'Modeling the radiation pattern of LEDs', *Opt. Express* **16**(3), 1808–1819.
URL: <http://www.opticsexpress.org/abstract.cfm?URI=oe-16-3-1808>

- Mousa, F., Almaadeed, N., Busawon, K., Bouridane, A., Binns, R. and Elliot, I. (2018), 'Indoor visible light communication localization system utilizing received signal strength indication technique and trilateration method', *Optical Engineering* **57**, 11.
- Naboulsi, M., Sizun, H. and Fornel, F. (2005), 'Propagation of optical and infrared waves in the atmosphere', *Proceedings of the union radio scientifique internationale* .
- Pal, D. and Chunchu, M. (2019), 'Modeling of lateral gap maintaining behavior of vehicles in heterogeneous traffic stream', *Transportation Letters* **11**(7), 373–381.
- Pal, D. and Mallikarjuna, C. (2010), 'Cellular automata cell structure for modeling heterogeneous traffic', *European Transport Trasporti Europei* **45**, 50–63.
- Papoulis, A., Pillai, S. and Pillai, S. (2002), *Probability, Random Variables, and Stochastic Processes*, McGraw-Hill (Inc.), New York, NY, USA.
- Pathak, P. H., Feng, X., Hu, P. and Mohapatra, P. (2015), 'Visible light communication, networking, and sensing: A survey, potential and challenges', *IEEE Communications Surveys Tutorials* **17**(4), 2047–2077.
- Poliak, J., Pezzei, P., Leitgeb, E. and Wilfert, O. (2012), Link budget for high-speed short-distance wireless optical link, in '2012 8th International Symposium on Communication Systems, Networks Digital Signal Processing (CSNDSP)', pp. 1–6.
- Proakis, J. G. (2001), *Digital Communications*, McGraw-Hill electrical engineering series, 4th ed... edn, McGraw-Hill, New York ; London.
- Puttonen, E., Suomalainen, J., Hakala, T. and Peltoniemi, J. (2009), 'Measurement of reflectance properties of asphalt surfaces and their usability as reference targets for aerial photos', *IEEE Transactions on Geoscience and Remote Sensing* **47**(7), 2330 – 2339.
- Pxhere.com (2017), 'morning golden sun yellow sun city urban waking up sunrise'.
- URL:** https://pxhere.com/en/photo/671311?utm_content=shareClip&utm_medium=referral&utm_source=pxhere

- Rahaim, M. and Little, T. D. C. (2017), 'Interference in IM/DD optical wireless communication networks', *IEEE/OSA J. Opt. Commun. Netw.* **9**(9), D51–D63.
- Rajagopal, S., Roberts, R. D. and Lim, S. (2012), 'IEEE 802.15.7 visible light communication: modulation schemes and dimming support', *IEEE Communications Magazine* **50**(3), 72–82.
- Rappaport, T. S. (2002), *Wireless communications : principles and practice*, Prentice-Hall communications engineering and emerging technologies, 2nd ed.. edn, Prentice-Hall ; Prentice-Hall International, Upper Saddle River, NJ. : London.
- Rehman, S., Ullah, S., Chong, P., Yongchareon, S. and Komosny, D. (2019), 'Visible light communication: a system perspective—overview and challenges', *Sensors* **19**(5), 1153.
- Roy, R. and Saha, P. (2018), 'Headway distribution models of two-lane roads under mixed traffic conditions: a case study from india', *Eur. Transp. Res. Rev.* **10**(1), 1–12.
- Sakhastka/Getty, O. (2021), 'Que te guste el olor a lluvia tiene una explicación científica'. [Online; accessed April 21, 2021].
URL: [//www.businessinsider.es/descubre-como-forma-te-gusta-olor-lluvia-795695](https://www.businessinsider.es/descubre-como-forma-te-gusta-olor-lluvia-795695)
- Schwartz, S. C. and Yeh, Y. S. (1982), 'On the distribution function and moments of power sums with log-normal components', *The Bell System Technical Journal* **61**(7), 1441–1462.
- Shen, W. and Tsai, H. (2017), Testing vehicle-to-vehicle visible light communications in real-world driving scenarios, in '2017 IEEE Vehicular Networking Conference (VNC)', pp. 187–194.
- Singh, G., Srivastava, A. and Bohara, V. A. (2018), On feasibility of VLC based car-to-car communication under solar irradiance and fog conditions, in 'Proceedings of the 1st International Workshop on Communication and Computing in Connected Vehicles and Platooning', C3VP '18, Association for Computing Machinery, New York, NY, USA, p. 1–7.

Singh, G., Srivastava, A. and Bohara, V. A. (2019), Impact of weather conditions and interference on the performance of VLC based V2V communication, *in* 'Proc. Int. Conf. Transparent Opt. Netw. (ICTON'19)', Angers, France, pp. 1–4.

Singh, G., Srivastava, A. and Bohara, V. A. (2020), 'Stochastic geometry-based interference characterization for RF and VLC-based vehicular communication system', *IEEE Systems Journal* pp. 1–11.

Singh/National, P. (2015), 'Morning fog on the Abu Dhabi-dubai motorway near ghantoot shows how badly visibility can be affected'. [Online; accessed April 21, 2021].

URL: <https://www.thenationalnews.com/uae/transport/fog-driving-warnings-issued-by-uae-police-after-more-crashes-1.6221>

Sklar, B. et al. (n.d.), *Digital communications: fundamentals and applications*, Prentice Hall.

Strbac-Hadzibegovic, N., Strbac-Savic, S. and Kostic, M. (2019), 'A new procedure for determining the road surface reduced luminance coefficient table by on-site measurements', *Lighting Research and Technology* **51**(1), 65–81.

Syed, N. (2014), 'Rows of car headlights'. [Online; accessed April 21, 2021].

URL: <https://unsplash.com/photos/Jk3-Uhdwjcs>

Technical Committee CPL/34 (1996), 'Part 9: Code of practice for lighting for urban centres and public amenity areas', *BRITISH STANDARD* (BS 5489-9:1996).

The Road Vehicles Lighting Regulations (1989), 'section 81 of the road traffic act 1988'.

URL: <https://www.legislation.gov.uk/uksi/1989/1796/made>

TimeandDate (2017), 'Coventry, england, united kingdom — sunrise, sunset, and daylength, november 2017'. [Online; accessed May 4, 2021].

URL: <https://www.timeanddate.com/sun/uk/coventry?month=11&year=2017>

- Tomaš, B., Tsai, H. M. and Boban, M. (2014), Simulating vehicular visible light communication: Physical radio and MAC modeling, *in* ‘2014 IEEE Vehicular Networking Conference (VNC)’, pp. 222–225.
- Torres-Zapata, E., Guerra, V., Rabadan, J., Perez-Jimenez, R. and Martin Luna-Rivera, J. (2020), Channel characterization of full-duplex VLC system for urban tunnels, *in* ‘2020 12th International Symposium on Communication Systems, Networks and Digital Signal Processing (CSNDSP)’, pp. 1–6.
- Toyota (2018), ‘Toyota corolla: LED rear combination lamps’, Brochure.
URL: <http://toyota-tsfm.com/Assets/Brochure/Corolla.pdf>
- Trio Adiono and Fuada, S. (2017), Investigation of optical interference noise characteristics in visible light communication system, *in* ‘2017 International Symposium on Nonlinear Theory and Its Applications’, Cancun, Mexico, pp. 612–615.
- Turan, B., Gurbilek, G., Uyrus, A. and Ergen, S. C. (2018), Vehicular VLC frequency domain channel sounding and characterization, *in* ‘2018 IEEE Vehicular Networking Conference (VNC)’, pp. 1–8.
- Ucar, S., Ergen, S. C. and Ozkasap, O. (2018a), ‘IEEE 802.11p and visible light hybrid communication based secure autonomous platoon’, *IEEE Transactions on Vehicular Technology* **67**(9), 8667–8681.
- Ucar, S., Ergen, S. C. and Ozkasap, O. (2018b), ‘Ieee 802.11p and visible light hybrid communication based secure autonomous platoon’, *IEEE Transactions on Vehicular Technology* **67**(9), 8667–8681.
- Uni (2013), *United Nations Economic Commission for Europe vehicle regulations, Reg. 112-Rev.3*.
- Uyrus, A., Turan, B., Basar, E. and Coleri, S. (2019), Visible light and mmWave propagation channel comparison for vehicular communications, *in* ‘2019 IEEE Vehicular Networking Conference (VNC)’, pp. 1–7.

- Uysal, M., Ghassemlooy, Z., Bekkali, A., Kadri, A. and Menouar, H. (2015), 'Visible light communication for vehicular networking: Performance study of a V2V system using a measured headlamp beam pattern model', *IEEE Veh. Technol. Mag.* **10**(4), 45–53.
- Viriyasitavat, W., Yu, S.-H. and Hsin-Mu, T. (2013), 'Short Paper : Channel Model for Visible Light Communications Using Off-the-shelf Scooter Taillight', *2013 IEEE Vehicular Networking Conference* pp. 170–173.
- Wang, J., Al-Kinani, A., Zhang, W., Wang, C. and Zhou, L. (2018), 'A general channel model for visible light communications in underground mines', *China Communications* **15**(9), 95–105.
- Wang, J., Li, K. and Lu, X.-Y. (2014), Chapter 5 - effect of human factors on driver behavior, in Y. Chen and L. Li, eds, 'Advances in Intelligent Vehicles', Academic Press, Boston, pp. 111 – 157.
- Wisitpongphan, N., Bai, F., Mudalige, P., Sadekar, V. and Tonguz, O. (2007), 'Routing in sparse vehicular Ad Hoc wireless networks', *IEEE Journal on Selected Areas in Communications* **25**(8), 1538–1556.
- World Health Organization (2018), 'Global status report on road safety 2018', (9789241565684).
URL: <https://www.who.int/publications/i/item/9789241565684>
- Yan, G. and Olariu, S. (2011), 'A probabilistic analysis of link duration in vehicular Ad Hoc networks', *IEEE Trans. Intell. Transp. Syst.* **12**(4), 1227–1236.
- Yasir, M., Ho, S. and Vellambi, B. N. (2016), 'Indoor position tracking using multiple optical receivers', *Journal of Lightwave Technology* **34**(4), 1166–1176.
- Zaki, R. W., Fayed, H. A., Abd El Aziz, A. and Aly, M. H. (2019), 'Outdoor visible light communication in intelligent transportation systems: Impact of snow and rain', *Applied Sciences* **9**(24), 5453.

- Zedini, E., Ansari, I. S. and Alouini, M. (2015), 'Performance analysis of mixed nakagami- m and gamma-gamma dual-hop fso transmission systems', *IEEE Photonics Journal* **7**(1), 1–20.
- Zhang, X., Duan, J., Fu, Y. and Shi, A. (2014), 'Theoretical accuracy analysis of indoor visible light communication positioning system based on received signal strength indicator', *Journal of Lightwave Technology* **32**(21), 4180–4186.
- Zhang, Z., Xu, K. and Gan, C. (2019), 'The vehicle-to-vehicle link duration scheme using platoon-optimized clustering algorithm', *IEEE Access* **7**, 78584–78596.
- Đurikovič, R. and Ágošton, T. (2007), 'Prediction of optical properties of paints', *Central Eur. J. Phys.* **5**(3), 416–427.